Electrodeposition of Ultra-Radiopure Copper-Chromium Alloys

By Anne-Marie Elizabeth Suriano

A dissertation submitted to the Graduate Division
in partial fulfillment of the requirements for the degree of

Doctor of Philosophy in Materials Engineering and Science

South Dakota School of Mines and Technology
Rapid City, South Dakota

Defended: November 15, 2016

_____   _____
Prepared by: Anne-Marie Elizabeth Suriano, Degree Candidate   Date

Approved by:

_____   _____
Major Professor – Stanley M. Howard, Ph.D., Department of   Date
Materials and Metallurgical Engineering

_____   _____
Graduate Division Representative – Sally B. Palmer, Ph.D.,   Date
Humanities Department

_____   _____
Committee Member – Cabot-Ann D. Christofferson, M.S.,   Date
Chemistry and Applied Biological Sciences Department

_____   _____
Committee Member – Eric W. Hoppe, B.S., Pacific Northwest   Date
National Laboratory

_____   _____
Committee Member – Jon J. Kellar, Ph.D., Materials and   Date
Metallurgical Engineering Department

_____   _____
Committee Member – William M. Cross, Ph.D., Materials   Date
and Metallurgical Engineering Department

_____   _____
Program Coordinator, Materials Engineering and Science   Date
– Jon J. Kellar, Ph.D.

_____   _____
Dean of Graduate Education – Douglas P. Wells, Ph.D.   Date

Abstract

The next generations of low background underground detector experiments searching for extremely rare physics interaction processes require ultra-radiopure structural materials containing the smallest obtainable amounts of naturally occurring radioactive uranium and thorium contaminants. Most materials contain trace amounts of uranium and thorium, and quantities as low as parts per quadrillion are important to these experiments. Electroformed copper is currently used to satisfy radiopurity requirements; however, it lacks the mechanical properties required for detector advancement. Structural alternatives to currently used copper are investigated, and a copper-chromium alloy is selected. A method of producing radiopure copper-chromium alloys is developed by electroplating copper and chromium in alternating layers, which are then heat treated to form a single-phase alloy. The alloy possesses favorable mechanical properties over pure electroformed copper currently used in radioassay detectors. Results show an increase from the average electroformed copper hardness of 72 HV to the maximum copper-chromium alloy hardness of 121 HV with 0.585 wt% chromium alloying element addition. Achieved alloy radiopurity is determined using inductively coupled plasma mass spectroscopy direct measurements of uranium and thorium. The developed copper-chromium alloy attained a radiopurity of 0.062 pg_{Th}/g_{Cr} and 0.031 pg_{U}/g_{Cr}.

Acknowledgements

First I would like to acknowledge my major advisor, Dr. Stanley Howard, who has guided me throughout the years. I have learned and grown so much under his counsel. My deepest gratitude goes to Cabot-Ann Christofferson, who was the force that got me through my dissertation. She encouraged me and fought for me throughout the entire process; without her support none of this work would've been possible. Along with Cabot-Ann I'd like to thank the entire Majorana Collaboration for believing in me.

Special thanks to Pacific Northwest National Laboratory Scientist Eric Hoppe, for his patience and assistance. He donated much time and effort to mentor me and help me grow as an Electrochemist, when it wasn't required of him. The path to completing my dissertation research was eased with help from my lab partners Isaac Arnquist and Adam Caldwell. They added joy and laughter to my research, an invaluable contribution. Additional thanks to Isaac, for his assistance in assaying radiopurity and analyzing results.

Great assistance was given to me by Environmental Molecular Sciences Laboratory Scientists Bruce Ayre, Odeta Qafoku, and Libor Kovarik. They put in much time and effort into my samples, and the level of technical characterization is because of them. I would like to thank Dr. Bharat Jasthi and Dr. Edward Duke for their assistance with SEM analysis. I also acknowledge Mark Horton, who started this work.

Lastly I thank my parents, Drs. John and Candace Suriano. They showed me the value of higher education, pushed me pursue and complete my Ph.D., and sacrificially financed my undergraduate degrees.

Table of Contents

List of Figures

List of Tables

List of Acronyms

$\beta\beta(0\upsilon)$	neutrinoless double-beta
BCC	body centered cubic
CC	chronocoulometry
CE	current efficiency
cnt	count
CP	close-packed
CP	chronopotentiometry
CRSS	critical resolve shear stress
CUORE	Cryogenic Underground Lab for Rare Events
CV	cyclic voltammetry
CW	cold worked
DC	direct current
DI	deionized
DM	dark matter
EDX	energy-dispersive x-ray spectroscopy
EFCu	electroformed copper
EFCu-Cr	electroformed copper-chromium
EMF	electromotive force
EMSL	Environmental Molecular Sciences Laboratory
FCC	face centered cubic
FFT	fast Fourier transform
FIB	focused ion beam
GB	grain boundary
GP	Guinier-Preston
HT	heat treat
HV	Vickers hardness
ICP-MS	inductively coupled plasma mass spectroscopy
IACS	International Annealed Copper Standard
KS	Kurdjumov-Sachs
LOD	limit of detection
LSW	Lifshitz-Slyozow-Wagner
MJD	The Majorana Demonstrator
nEXO	next Enriched Xenon Observatory
NW	Nishiyama-Wassermann
OFHC	oxygen-free high conductivity
OR	orientation relationship
PB	process blank
PFA	perfluroalkoxy
PNNL	Pacific Northwest National Laboratory

PP	polypropylene
PP	pulse-plate
PTFE	polytetrafluoroethylene
RDE	rotating disk electrode
RDS	rate determining step
ROI	region of interest
ROI-t-y	region of interest-tonne-year
RPM	rotations per minute
RR	rejection rate
SAD	selected area diffraction
SDSMT	South Dakota School of Mines and Technology
SEM	secondary electron microscope
SHE	standard hydrogen electrode
SNO+	Sudbury Neutrino Observatory +
SOFC	solid oxide fuel cell
SS	stainless steel
SURF	Sanford Underground Research Facility
TEM	transmission electron microscope
UG	underground
UTS	ultimate tensile strength
VIM	vacuum induction melted
YS	yield strength

List of Variables

A_i	ionic strength constant
A_d	cross-sectional area after cold working
A_o	original cross-sectional area
A_{wt}	atomic weight
a	lattic constant
a_c	smaller electrode radius
a_{Cr}	Cr precipitate lattice constants
a_{Cu}	Cu matrix lattice constants
a_{erf}	error function integration constant
a_i	hydrated ion size
a_M	activity of the metal ion being reduced
a_{prod}	ion activity of product
a_{react}	ion activity of reactant
a_t	experimental Tafel constant
B_i	ionic strength constant
b_t	experimental Tafel constant
b	Burgers vector magnitude
b_c	larger electrode radius
b_x, b_y, and b_z	Burgers vector components
C	solute concentration
C_b	bulk metal ion concentration
Ccr	Cr concentration
Ccu	Cu concentration
C_M	metal ion concentration
c_1 and c_2	solute concentrations in coupled layers
c_j	concentration of species j
D	total surface excess energy
D^*	diffusion coefficient
D_M	diffusion coefficient
d	effective particle diameter
d	grain size
E	energy
E^o	standard electrode potential
E_{OC}	open circuit potential

E_v	voltage present under flow of current
F	Faraday's constant
f	frequency
f_p	volume fraction of spherical precipitates
H	Vickers hardness
H_o	Hall-Petch line intercept
h	geometry constant
I	ionic strength
I	current
i_{lim}	limiting current
i_0	exchange current
i_{peak}	deposition peak current
i, j, and k	directions
j	current density
j	atomic flux
K_H	Hall-Petch line slope
K_p	equilibrium constant
L	length
M_{aq}^{n+}	aquated metal ions
M_s	solid metal
m	concentration coefficient
N	number of atoms
N^*	critical atomic cluster size
n	valence
P_{O2}	oxygen pressure
Q	charge
Q_D	double layer charge
Q_i	interfacial interactions charge
Q_j	charge passed in reaction j
Q_{total}	total charge passed
R	gas constant
r^*	critical radius
r	precipitate spacing
r_b	dislocation radius of curvature
r_L	empirical precipitate spacing
S_A	surface area
s	scan rate

T	temperature
$T_{critical}$	critical nucleation temperature
t	time
V	Voltage
V_β	Cr-phase molar volume
$V_{Cu,450um}$	volume of plated Cu for a 450 um thickness
$<v>_F$	atom drift velocity
v_k	local lattice plane velocity
v_m	atom volume
w_j	weight of metal deposited
$w_{Faraday}$	Faradaic weight
wt_{Cr}	grams of Cr dissolved
X_α	coherent solubility of Cr
X_β	Cr molar fraction
X(Cu,Cr)	equilibrium solubility of Cr in Cu
X_{Cr}	atomic fraction of Cr in Cu
x	diffusion depth
y	error function tabulated value
Z	error function tabulated value
Z	atomic number
z	number of electrons transferred
α	transfer coefficient
α_s	flow stress constant
γ	activity coefficient
γ	interfacial energy
ΔG	Gibbs Energy Change
ΔG^*	precipitate nucleation barrier
ΔG_{el}	elastic energy
ΔG_n	nucleation driving force
ΔG_o	standard Gibbs Energy change
ΔH	enthalpy change
ΔS	partial molar excess entropy
δ	diffusion layer thickness
δ_x	linear lattice misfit
ε	dielectric permittivity
η	overpotential
λ	orientation angle of the slip plane relative to tensile axis
μ	shear modulus

υ	kinematic viscosity
σ	average surface energy
σy	yield strength
ρ_{Cu}	density of Cu
τ	flow stress
ϕ	orientation angle of the slip plane relative to tensile axis
ω	angular velocity
"	inch

1. INTRODUCTION

Copper is an important metal in both industry and basic research. It is a stable, native element with ore deposits of relative high purity. Electroforming, a derivative of the industrial refining process for Cu, benefits from Cu's nobility to yield the most radiopure material currently produced. Radiopurity is essential to minimize background signals for materials adjacent rare-event physics detectors searching for neutrinoless double-beta decay and dark matter. Detector projects using radiopure electroformed Cu components struggle with design of structural and mechanical parts which fail because of Cu's ductility and creep. This research establishes a method of producing a radiopure copper-chromium alloy with physical properties more suitable than those of current electroformed Cu for detector advancement.

Current radioactive background requirements on rare-event physics experiments are met using ultra-radiopure electroformed Cu (EFCu) designed and plated at Pacific Northwest National Laboratory (PNNL). Cu was selected for many reasons. It has excellent electrical and thermal conductivity, meeting many design requirements. Detector parts can be machined from EFCu because unlike many elements compact deposits can be plated to a significant thickness. Lack of long-lived radioactive isotopes and progeny make it suitable for minimizing backgrounds. Cu is also relatively abundant and inexpensive. Unfortunately, Cu possesses a face centered cubic (FCC) structure with 12 slip systems. This leads to Cu's undesirably high ductility and low strength, limiting its use for moving mechanical, high-pressure, and load-bearing parts. A higher strength radiopure alternative to EFCu is desirable for use in such components.

The achievable radiopurity of various alternative materials has been examined and assayed. Results show that EFCu attains radiopurity much higher than other structurally suitable materials[1]. Mechanical properties of Cu can be improved through alloying. Second phase particles in the Cu matrix resist dislocation movement and can produce large strength increases. Retaining Cu as the major alloying element in an EFCu alternative maintains achieved radiopurity while increasing plastic deformation resistance.

Potential minor alloying elements which satisfy both mechanical and radiochemical requirements were investigated. Cr has a body centered cubic (BCC) structure with large lattice misfit to Cu. Therefore, additions of minimal concentrations of Cr to Cu provide significant strength increases. The maximum solubility of Cr in Cu is less than 2%, allowing the necessary electrical and thermal support provided by pure Cu to be maintained. Cr is more reactive than Cu and refined from complex ore deposits. This indicates that radio-contaminants are more likely to be included at higher concentrations in Cr deposits than in Cu deposits. Nernstian-refining of Cr sources thermodynamically will exclude fewer contaminants. The solubility limit, therefore, also serves to limit the concentration of additional impurities introduced to the alloy.

The electrochemical basis for excluding radiocontaminents from pure Cu can also be used to develop a radiopure Cu-Cr alloy. Electrodeposition of Cr and Cu thin films separately is common; however, the area of electroforming to a significant thickness without the use of additives, as done by PNNL, is still considered to be in the research and development phase. Increase in adsorption sites, electric field effects, increasing concentration of particles in the electrolyte, shifting limiting current and bath chemistry,

and other complex cell effects cause the deposit structure to become progressively more granular over long plating times. There are no literature references on co-electrodeposition of Cu and Cr(VI), whose reduction potentials vary significantly. Very little research has been done on plating without the use of radioimpurity contributing additives used to close the plating potential gap, suppress dendrite growth, improve current efficiency, and level and brighten deposits. In research and industry Cu and Cr are rarely plated directly on each other, but always with an intermediate. Tertiary elements such as Ni are used to relieve the high stress Cr deposits and increase poor adhesion between Cu and Cr layers that result from factors such as low solubility of Cr in Cu and lattice mismatch. This research addresses these gaps in the areas of electrochemistry and alloy development.

The need for technological advances in radiopure alloys does not lie solely with physics detector projects, but more predominantly in industry. Microelectronics require high purity to increase efficiency and high radiopurity to prevent soft errors caused by alpha emissions. Alternative alloys for integrated circuit interconnects are needed to improve electromigration while approaching the low resistivity of Cu[2]. Alloys are also needed for solid oxide fuel cell (SOFC) interconnects to lower operating temperature[3]. Research into electrodepositing ultra-pure intermetallics and alloys could lead to smaller, more efficient microelectronics and batteries, industries greatly affecting the U.S. economy.

2. THEORY

2.1 Ultra-Low Background Materials

Most materials contain trace amounts of naturally occurring radioactive uranium and thorium decay chain contaminants ranging in the microgram/gram to nanogram/gram level. Contaminants at these levels produce unacceptable backgrounds in many of the planned next-generation physics experiments. New materials must be developed which meet both radiochemical and physical property requirements.

2.1.2 Physics Detectors

The search for neutrinoless double-beta ($\beta\beta(0\upsilon)$) decay is a major area of rare-event physics research and the subject of many physics projects. During beta decay, a neutron decays to a proton by emitting an electron and an anti-neutrino. If the neutrino is a Dirac particle, during double beta decay two anti-neutrinos are resultant [4, 5]. If it is instead a Majorana particle the decay produces no neutrinos. This is referred to as neutrinoless double-beta decay, and has as of yet never been observed.

$\beta\beta(0\upsilon)$-decay experiments are highly competitive with a variety of detector projects spanning the United States (The Majorana Demonstrator MJD[1, 4, 6, 7, 8, 9, 10] and next Enriched Xenon Observatory nEXO[11]), Canada (Sudbury Neutrino Observatory SNO+)[12], Italy (Cryogenic Underground Laboratory for Rare Events CUORE)[13], to name a few. Although the detector type varies between projects (solid semi-conducting crystals, bolometers, scintillators) the need for low background signal noise remains the same.

Dark matter (DM) experiments have a higher energy range for which early-generation experiments lacked the same background requirements of $\beta\beta(0\upsilon)$-decay. With the onset of next-generation DM projects, where higher sensitivity and larger mass parts are needed, they are approaching the energy region and background needs of the $\beta\beta(0\upsilon)$ experiments. DM experiments will not be able to proceed without the ultra-radiopure materials used by current neutrino detectors.

2.1.2 The Majorana Demonstrator

The Majorana Demonstrator (MJD) is a currently funded Department of Energy rare-event physics detector investigating $\beta\beta(0\upsilon)$ using enriched germanium ^{76}Ge. The goal of MJD is to prove the possibility of detecting $\beta\beta(0\upsilon)$-decay in a larger one-tonne experiment by reaching scalable background count rates. The maximum background rate for success of the demonstrator is 3 counts (cnt) per region of interest-tonne-year (ROI-t-yr). Current background requirements for MJD and many other projects are met using ultra-radiopure electroformed Cu. Only <0.3 uBq ^{232}Th and ^{238}U is budgeted for ultra-radiopure Cu constituents [1]. Increasing the mass of the detector increases the mass of possible U and Th containing component parts. The one-tonne detector will have a maximum background of 1 cnt/(ROI-t-yr) [4]. MJD's next-scale background requirements are the motivation for this research.

2.1.3 Radioactive Backgrounds

The expected half-life of $\beta\beta(0\upsilon)$-decay is on the order of 10^{27} yrs[1, 7, 9]. This indicates a very low rate of incidence and low likelihood of detection with any background signal noise present in the region of interest (ROI). The ROI is the energy

region around the decay peak excited in the chosen detector medium. In ^{76}Ge the decay peak occurs at a Q-value of 2,039 KeV. Around 4KeV of this a background rate of 1 cnt/(ROI-t-y) is the maximum allowable for decay observation[1, 4, 7, 8, 9]. The presence of ^{238}U, ^{232}Th [4, 7], ^{210}Pb and ^{60}Co[1, 4, 6, 7, 8, 10] in material surrounding a detector produce signals in the ROI, contributing to the maximum one count allowable. These particles are the radioimpurities for which exclusion is imperative to the success of large-scale $\beta\beta(0\upsilon)$ and DM experiments.

2.1.4 Radioisotope Contaminants

Key steps are taken to reduce concentrations of each background contributing radionuclide present near detectors. ^{60}Co is a result of cosmogenic activation of Cu and Ge[4, 6], where secondary neutrons are produced in a given material by cosmic rays from the Sun. ^{60}Co has a 5.2 year half-life, Q-value of 2.5 MeV[14] and an emission line at 1332.5 KeV[7]. To prevent ^{60}Co formation, detector components are shielded underground. This can include refining, machining, and commissioning parts in deep underground mines such as Sanford Underground Research Facility (SURF) for the MJD [4], Laboratori Nazionali del Gran Sasso for CUORE[13], and Creighton mine for SNO+[12]. The refining methods selected must also take into account removal of ^{60}Co from the bulk starting material.

^{210}Pb is part of the ^{238}U and ^{222}Rn decay chain. Rn decay chain daughter products are present in ambient atmosphere and will plate out onto material surfaces, such as detector parts, leaving ^{210}Pb background[6]. Rn surface contamination has been reported as the dominant background in rare-event detectors[10]. This can be partially mitigated by refining materials in a Rn-scrubbed and monitored cleanroom environment[8]. Any

remaining surface contamination on final components is removed through chemical

etching and leaching before storing in inert-gas purged containers[1].

^{238}U and ^{232}Th are the main concern when designing materials refining methods

for near-detector components. The radiopurity defining background signal is quantified

by concentration of ^{238}U and ^{232}Th present. ^{238}U and ^{232}Th decay chain daughter products

^{214}Bi and ^{208}Tl are the impurities causing energy signals in the ROI. If secular

equilibrium holds, the activities of all isotopes in the decay chain are the same. Bi and Tl

isotopes produce background through gamma-ray Compton scattering in Ge[1, 7] detector

crystals. They are measured by gamma-ray counting while Th and U are measured by the

much more sensitive technique of inductively coupled plasma mass spectroscopy (ICP-

MS). The constant relationship between the two sets of isotopes is verified by using

these counting methods in parallel. Secular equilibrium is then assumed for future

measurements such that only U and Th concentrations are monitored[1]. ^{238}U and ^{232}Th

are naturally present in materials of higher nobility and must be removed. They are often

also a consequence of dust covering surfaces, or inclusioned during refining. Confining

all processing steps to a dust-particle limiting cleanroom significantly reduces possible

contamination.

2.2 Physical Metallurgy of Cu-Cr

Although electrorefined Cu achieves desired Majorana Demonstrator radiopurity requirements, it falls short of requested mechanical properties. Structural components must be plated to an exorbitant thickness (~0.5") to withstand load. This takes considerable time and cost at the allowable plate-rate. The higher mass also results in more contaminants per part for the same impurity concentration. Threaded parts such as screws must be taken to the surface and Paralyene coated to prevent galling[1, 4]. Such processing risks cosmogenic activation and coats a painstakingly ultra-radiopurified part in a polymer containing orders of magnitude greater concentrations of U and Th[1]. The ductility of Cu as well makes it extremely difficult and time consuming for even an experienced worker to machine.

Strengthening stress concentrations produced by post-processing work hardening (rolling for example) in industrially produced Cu are not present in EFCu. EFCu purity requirements prohibit impurities common to Cu, such as Fe, that otherwise impede dislocation movement along slip planes[15, 16]. Low current density (j) EFCu crystal growth starts epitaxially resulting in low-angle grain boundaries and aligned grains[17, 18]. The energy for dislocations to move between grains on subsequent aligned slip planes is relatively low. A radiopure alternative to EFCu with improved mechanical properties is required.

2.2.1 Slip in Cu

Cu possesses a FCC cubic structure. The FCC crystal structure has four close-packed (CP) octahedral planes of the {111} family. Each CP plane contains three <110>-

type CP directions [15, 16]. These planes and directions come together to constitute 12 slip systems, the most of any crystal structure and the origin of Cu's extreme ductility.

Slip is the mechanism by which dislocations in FCC crystals move on active slip systems. During shear stress the plane of atoms above a dislocation rises to a maximum point above the neighboring atoms in the plane below the dislocation before settling in a new equilibrium position. The lattice strain incurred is related to the Burger's vector $\vec{b}$ describing direction and magnitude of a dislocation by the equation,

$$\vec{b} = b_x \hat{i} + b_y \hat{j} + b_z \hat{k} \tag{2.1}$$

where b_x, b_y, and b_z are the Burgers vector components in the i, j, and k unit directions[15, 19]. For a full FCC Cu lattice transition with lattice constant a the magnitude of the Burgers vector b is[15]

$$b = \frac{a}{2} < 110 > . \tag{2.2}$$

Positioning of FCC slip planes allows dislocations to move within the plane when stacking faults are present. Atoms do not have to strain to a saddle point lowering the activation energy required to move. Dislocations in FCC Cu dissociate into Shockley partials

$$\frac{a}{6} < 112 >$$

with the reaction

$$\frac{a}{2}[\bar{1}10] \leftrightarrow \frac{a}{6}[\bar{1}2\bar{1}] + \text{intrinsic stacking fault} + \frac{a}{6}[\bar{2}11]$$

by the removal of the {111} plane creating an intrinsic stacking fault[15, 19]. The critical resolve shear stress (CRSS) τ_{CRSS} is given by

$$\tau_{CRSS} = \sigma_y (\cos\phi \cos\lambda)_{max} \tag{2.3}$$

where σ_y is the yield strength, and ϕ and λ are orientation angles of the slip plane

relative to the tensile axis[16]. The CRSS is lowered through partial dislocation movement

in FCC. Therefore, the yield strength of Cu is very low relative to commonly used

structural materials, such as stainless steel (SS), and it easily plastically deforms.

2.2.2 Cu-Cr Precipitation Hardening

Cu-Cr alloy precipitation hardening produces large strength increases over pure

Cu and is the strengthening method selected for this work. Precipitation alloy hardening

mechanisms include (1) chemical strengthening (2) coherency strengthening and (3)

dislocation looping[20, 21]. Prevailing mechanism depends upon extent of Cr precipitate

coarsening, which will be discussed in § 2.4.

Deformable precipitates are small coherent or semi-coherent particles formed in

the early stages of aging. Alloy strengthening resulting from deformable precipitates is a

weak function of precipitate radius and a strong function of precipitate properties[21].

Dislocations can interact with deformable particles by a mixture of shearing through them

(chemical strengthening) and bending around them (coherency strengthening).

It is energetically unfavorable for dislocations in Cu to pass through Cr

precipitates which possess a different crystal structure. Chemical strengthening is,

therefore, minimal and not factored into computations. The mechanism for deformable

particle strengthening in Cu-Cr alloys is dominated by coherency strain. The precipitate

associated misfit stress field resists dislocation movement by forcing dislocations to bow

around precipitates[21]. The linear lattice misfit δ_x is given by

$$\delta_x = \frac{a_{Cr} - a_{Cu}}{a_{Cu}} \tag{2.4}$$

where a_{Cr} and a_{Cu} are the lattice constants of the Cr precipitate and the Cu matrix[22].

Coherent and incoherent Cr precipitates possess the same BCC crystal structure[23] with

different lattice spacing.

For a dislocation to pass by a lattice misfit incurred internal stress field, as shown

in Fig. 2.1a, the dislocation must apply a greater or equal stress. This is given by flow

stress τ

$$\tau = 2\mu\delta_x f_p \tag{2.5}$$

for shear modulus μ and volume fraction of spherical precipitates f_p. The dislocation

radius of curvature r_b which accounts for precipitate spacing through which a dislocation

can bend is

$$r_b = \frac{\alpha_s \mu b}{\tau} \tag{2.6}$$

for temperature-dependent flow stress constant, α_s, which is generally ~0.5. Therefore,

the flow stress for small coherent particles with spacing r is [21]

$$\tau = 4.1\mu\delta_x{}^{3/2}f^{1/2}{}_p \left(\frac{r}{b}\right)^{1/2}. \tag{2.7}$$

As precipitates age and coarsen the energy for dislocations to loop around

precipitates becomes lower than the energy to shear them[15, 20, 22, 24]. Coarsened particles

are incoherent and possess no misfit strain, allowing dislocations to bypass without

bowing. Since no strain is induced by the precipitate lattice, strengthening from non-

deformable particles is independent of particle properties. Hardening is instead a strong

function of precipitate radius and dispersion[21].

Orowan theory describes the looping mechanism by which non-deformable

hardening occurs[19, 20]. Moving dislocations bend around precipitates, traversing until

the dislocation line meets again on the opposing side of the particle and pinch off. This creates a loop with associated strain field. Dislocations continue to travel along the precipitate-intersecting slip plane resulting in a series of concentric loops around precipitates as shown in Fig. 2.1b. This effectively lowers the distance between particles.
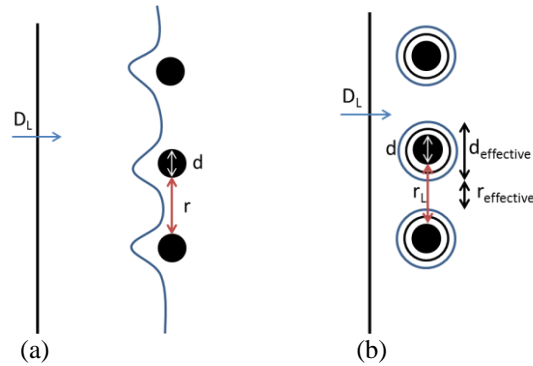
Figure 2.1: (a) Bending dislocation (b) Orowan looping

Much work has been done on Orowan stress computations to account for geometric effects, distribution, and dislocation character. The result is developed by Hirsch and Humphreys[25] with empirical determination of particle spacing r_L,

$$\tau = 0.81 \frac{\mu b}{2\pi r_L} \ln\left(\frac{d}{4b}\right). \tag{2.8}$$

$$r_L = N^{-1/2}$$

where the factor 0.81 accounts for 3D precipitate projected onto 2D plane, N is the number of precipitate shown in a TEM image for a unit planar area, and d is the effective particle diameter.

As can be seen from this relation, the stress is inversely related to the distance between incoherent particles. Smaller spacing increases stress needed for successive dislocations to pass. Solute volume and aging parameters dictate actual particle spacing.

Concentric dislocation loops pile up, effectively lowering this spacing[19]. The result is a work hardening effect in precipitation hardened alloys.

2.2.3 Strain Hardening

Strain hardening is commonly used to improve the hardness of Cu. The high number of FCC Cu slip systems allows multiple differently oriented planes to activate simultaneously under plastic deformation. Intersecting active planes pin crossing dislocations, leading to high stress concentrations and rapid strengthening. Defects multiply during plastic deformation, also increasing the stress concentration. The percent cold worked (CW) achieved during such strain hardening is described by

$$\%CW = \left(\frac{A_o - A_d}{A_o}\right) * 100 \tag{2.9}$$

where A_o is the original cross-sectional area and A_d is the area after cold working deformation[16]. A strain hardened material, therefore, possesses reduced cross section. CW accomplished through rolling presses surface impurities into the sample surface. To maintain radiopurity the parts would have to be skim cut to remove these impurities post-CW. This would further reduce the part thickness and counteract achieved strengthening.

Strain hardening is also used in precipitation alloying to improve potential increase in hardness. After solution treating and quenching a precipitation hardened alloy, the solid solution rejects supersaturated solute atoms through precipitation[15, 16]. The increase in defect density from cold working between solution treating and age hardening increases the concentration of thermodynamically favorable nucleation sites. Eutectic alloy hardness increases with the precipitate concentration[24]. This is seen through decreased precipitate spacing increasing flow stress in Eq. 2.8.

2.2.4 Grain Boundary Strengthening

The atoms at grain boundaries (GB) have longer bond angles and unsatisfied bonds attributing to a GB energy [16] higher than lattice energy.   Lattice strain from GBs hinders dislocation mobility, decreasing plastic deformation. Different orientations between neighboring grains results in misaligned slip planes, raising the energy for slip to travel between grains. This energy increases with increasing GB angle. Dislocations become pinned at GBs and pile up, increasing dislocation density and stress concentration [15, 16, 26]. The resulting strength increase is modeled by the Hall-Petch[15] equation for Vickers hardness where empirical values of hardness H and grain size d are plotted against each other,

$$H = H_o + K_H d^{-1/2} \ . \tag{2.10}$$

H_o is the plotted line's intercept and K_H is the line slope.

Grain size in an electrolytically grown crystal is controlled by current density and applied waveform frequency. The relationship between current density and nucleation, which effects grain size, will be discussed in § 2.3.8.3. The periodically applied forward voltage defined by the waveform results in periodic grain re-nucleation, as will be discussed in § 2.3.

Precipitates preferentially form at GBs during age hardening because GB energy and open atomic sites lower nucleation barrier energy. Cr precipitates have a different elastic constant than the bulk Cu material, resulting in stress concentrations at precipitates during deformation. For extensive GB precipitation, this undesirably affects the Cu-Cr alloy's mechanical properties and can eventually lead to failure[24].

2.2.5 Cu-Cr Strength

The correlations between ultimate tensile strength (UTS), yield strength (YS), and hardness have been investigated for many materials, allowing hardness testing to represent strength behavior. Typical mathematical relationships for strain hardening materials result in variation from theory at high and low values. Krishna has performed extensive research on empirical relations for Cu-alloys with various strengthening properties. This research determined that the derivation from the linear strength-hardness for age-hardened alloys with hardness >110 Vickers hardness (HV) show excellent correlation. The developed relations are[27]

$$YS \text{ (MPa)} = 2.874 * HV \qquad (2.11)$$

$$UTS \text{ (MPa)} = 3.353 * HV. \qquad (2.12)$$

2.3 Electrochemistry

Electroforming is the process by which Cu is refined and produced by PNNL for use in radioassay detectors. Electroforming is a subset of electroplating in which the resulting deposits are removed from the mold on which they are plated[28]. It refines by excluding instead of removing contaminants.

2.3.1 The Electrolytic Cell

An electrolytic cell or bath as shown in Fig. 2.2 consists of an anode, cathode, and electrolyte. During electrorefining solid impure metal is oxidized at the anode into aquated metal ions M_{aq}^{n+} with valence n. The ions in solution diffuse to the cathode where they are reduced to solid metal M_s,

$$M_{aq}^{n+} + ze- \rightleftharpoons M_s \tag{2.13}$$
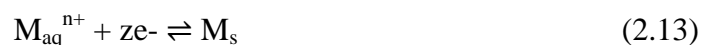
through a transfer of z electrons[29].
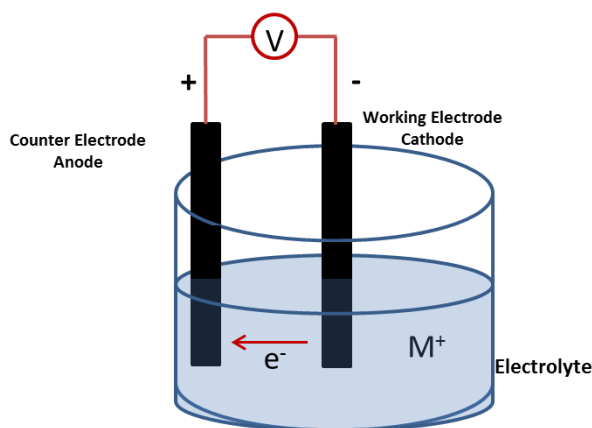
Figure 2.2: An electrolytic cell or bath

2.3.2 Kinetics of Electrodeposition

The deposition of a metal ion from solution onto a cathode is described by the following process shown in Fig. 2.3:

1. Metal ion mass transport from bulk

2. Boundary layer diffusion

3. Adsorption or nucleation

4. Crystal growth

It is assumed (1) there is a sufficient concentration of metal ion already in solution and (2) the oxidation reaction rate at the anode is significantly higher than the deposition rate at the cathode such that the rate determining step (RDS) is not affected by anode reactions. With adequate solution flow the boundary layer thickness approaches zero and steady state is achieved. Mass transport then becomes the slowest deposition step and transport variables regulate the limiting current. These variables include conductivity, viscosity, temperature, and convection[29].   Applied current density relative to limiting current density of the system dictates deposit structure and quality.
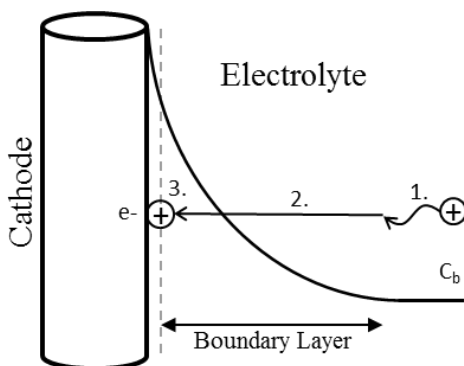
Figure 2.3: Metal ion deposition

Kinetic constants are determined experimentally. The relationship between the diffusion limited current and concentration is derived from the second order Fick's Diffusion Law and is known as the Cottrell Equation[30],

$$i(t) = \frac{zFS_A D_M^{1/2} C_b}{\pi^{1/2} t^{\frac{1}{2}}} \tag{2.14}$$

for current i, time t, cathode surface area S_A (cm^2), bulk metal ion concentration C_b, Faraday's constant F, and diffusion coefficient D_M. This is used to model concentration profile away from the cathode using the error function solution for diffusion. Charge, Q, effects of a system can be measured through observing current response over time. Since Q=it,

$$Q(t) = \int_0^t i(t) dt. \tag{2.15}$$

This makes the integrated Cottrell Equation[30],

$$Q = \frac{2nFS_A C_b D_M^{1/2} t^{1/2}}{\pi^{1/2}} + Q_D + Q_i \tag{2.16}$$

where Q_D is the double layer charge and Q_i is interfacial interactions charge for a planar electrode.

Metal ion diffusion coefficient D_M is described by the Randles-Sevcik equation[31]

$$i_{peak} = 269z^{1.5} S_A D_M s^{0.5} C_b \tag{2.17}$$

for deposition peak current i_{peak} and scan rate s at room temperature T = 25 ^{o}C.

The Tafel relation for reversible systems at cathodic high overpotentials η is[30]

$$\eta = a_t - b_t \log|i| \tag{2.18}$$

where experimental parameters a_t and b_t provide information on kinetic constants transfer coefficient α and exchange current i_0,

$$a_t = \left(\frac{2.3RT}{\alpha F}\right) \log i_0, \, b_t = \left(\frac{-2.3RT}{\alpha F}\right). \tag{2.19}$$

for gas constant R and temperature T.   Allen and Hickling proposed a form using low overpotentials which can be used in quasi-reversible systems[30],

$$i = i_0 e^{-\frac{\alpha F\eta}{RT}}(1 - e^{\frac{F\eta}{RT}}). \tag{2.20}$$

The overpotential is the driving force for electron transfer in electrochemical systems. It is defined by[32]

$$\eta = E_v - E_{OC}. \tag{2.21}$$

E_{OC}, the open circuit potential, is the potential at equilibrium. E_v is the driven voltage, or that present under flow of current.

Diffusion layer information can be found experimentally using the Levich equation,

$$i_{lim} = 0.620\ zFS_AC_bD_M{}^{2/3}\upsilon^{-1/6}\omega^{1/2} \tag{2.22}$$

where i_{lim} is the limiting current, υ is the kinematic viscosity, and ω is the angular velocity of the cathode. The electrode frequency f in rotations per minute (RPM) is $f = \omega/2\pi$. From this the diffusion layer thickness δ is found to be[33]

$$\delta = 1.61\ D_M{}^{1/3}\omega^{-1/2}\upsilon^{1/16}. \tag{2.23}$$

The kinetics involved in electrorefining are discussed in greater detail in Appendix A "Rate of Metal Deposition from Aqueous Solutions"[29].

2.3.3 The Nernst Equation

The energy, E, required to move Eq. 2.13 to the right and reduce a selected ion is given by the Nernst Equation

$$E = E^0 + \left(\frac{RT}{zF}\right)\ln\{\frac{\prod a_{react}}{\prod a_{prod}}\} \tag{2.24}$$

for standard electrode potential of the ion being reduced E^o and ion activities of reactants a_{react} and products a_{prod} during equilibrium[32, 34]. Solids possess an activity at unity, changing Eq. 2.24 to

$$E = E^0 + \frac{0.0592}{z} \log\{a_M\} \qquad (2.25)$$

at room temperature. The activity of the metal ion being reduced, a_M, is given by

$$a_M = \gamma \, C_M \qquad (2.26)$$

where C_M is the metal ion concentration and γ is the activity coefficient which depends upon the strength of ion-to-ion interactions in solution[32]. The activity coefficient for the $CuSO_4$ system is calculated using the Extended Debye-Huckel for ionic strengths I below 0.1 M[35],

$$\log(\gamma) = -A_i z^2 \frac{\sqrt{I}}{1+B_i a_i \sqrt{I}} \qquad (2.27)$$

where A_i and B_i are unitless constants equaling 0.51 and 0.33×10^8 at 25 ^{o}C. Table 2.1 lists the size of the hydrated ion of interest a_i in cm. Ionic size is not tabulated for the various species such as $H_2Cr_nO_{3n+1}$ complexes which may be present in a chromic acid (H_2CrO_4) solution[36]. In these cases the Davies approach[35] is used instead,

$$\log(\gamma) = -A_i z^2 \left(\frac{\sqrt{I}}{1+\sqrt{I}} - 0.2I \right). \qquad (2.28)$$

The ionic strength for both approaches is given by

$$I = 0.5 \sum c_j z_j^2 \qquad (2.29)$$

with concentration c_j. At very low concentrations the activity coefficient is about one and the concentration C_M may be used in Nernst calculations.

Table 2.1: Hydrated ion diameters of interest

Ion	Size (A)
H^+	9
Cu^{2+}	6
SO_4^{2-}	4

For low background physics detector component material naturally occurring contaminants U, Th, and Co must be excluded during electroforming. The Nernst Equation (Eq. 2.25) is used to determine the applied voltage needed to reduce the metal of interest. Operating below the reduction potential of a given species will exclude it from depositing. Therefore, to refine materials for exclusion of U, Th only potentials significantly electropositive (lower) to them may be applied. Table 2.2 lists standard half-cell potentials of interest. Notice radiocontaminant potentials are much more electronegative (higher) than Cu and, therefore, require a higher driving potential to induce deposition. The concentrations of contaminants in the electrolyte are minimized to prevent a decrease in this required potential, as indicated by the Nernst Equation. Electroforming operating voltage parameters are designed to stay well below potentials, which could reduce the radiocontaminants at any possible concentration.

Table 2.2:Half-cell potentials of interest

Metal	Reaction	E^o (V)	ΔE^o_{Th} (V)	ΔE^o_U (V)
Cu	$Cu^{2+} + 2e^- \leftrightarrow Cu_{(S)}$	0.34	-2.17	-1.98
Cr	$Cr^{3+} + e^- \leftrightarrow Cr^{2+}$	-0.42	-1.41	-1.22
	$Cr^{2+} + 2e^- \leftrightarrow Cr_{(s)}$	-0.89	-0.94	-0.75
	$Cr^{3+} + 3e^- \leftrightarrow Cr_{(s)}$	-0.74	-1.09	-0.9
	$Cr(OH)^{2+} + H^+ + 3e^- \leftrightarrow Cr_{(s)} + H_2O$	-0.058	-1.772	-1.582
	$0.5Cr_2O_7^{2-} + 7H^+ + 3e^- \leftrightarrow Cr^{3+} + 3.5H_2O$	1.10	-2.93	-2.74
	$Cr^{6+} + 6e^- \leftrightarrow Cr_{(s)}$ (Experimental)	-0.63	-	-
Ni	$Ni^{2+} + 2e^- \leftrightarrow Ni_{(S)}$	-0.24	-1.59	-1.4
Be	$Be^{2+} + 2e^- \leftrightarrow Be_{(S)}$	-1.97	0.14	0.33
U	$U^{3+} + 3e^- \leftrightarrow U_{(S)}$	-1.64	-0.19	0
Th	$Th^{4+} + 4e^- \leftrightarrow Th_{(S)}$	-1.83	0	0.19

To maintain deposit radiopurity the highest allowable U, Th concentrations in MJD EFCu electrolyte have been identified as being 0.024 ng_U/ml and 0.078 ng_{Th}/ml[1]. These are significantly lower values than indicated by the Nernst Equation. The difference can be explained by impurity inclusions which increase at high concentrations and high current densities from mass transport effects[9, 10].

2.3.4 Electroformed Cu

Cu is currently being electroformed at PNNL for a variety of experiments including the MJD at unprecedented radiopurity. Cu was selected for its favorable radiochemical, thermal, and electrical properties as the main MJD construction material. Cu is found elemental in nature and is naturally relatively radiopure because of its lack of reactivity. This is shown by its Gibbs energy and placement at the top of the Ellingham diagram. Cu has a positive half-cell potential of $E^o = 0.34$ V vs. the standard hydrogen electrode (SHE)[32], allowing high purity through electrorefining. It is one of the few elements having no relatively long-lived background contributing radioisotopes. Cu's longest radioisotope is ^{67}Cu with a half-life of 61.88 hrs[37]. It has excellent thermal conductivity of 388 W/(m*K)[16] and electrical conductivity of over 100% International Annealed Copper Standard (IACS)[37]. Cu is also relatively abundant and inexpensive compared to more noble metal options, making it the fiscally viable selection for high-mass shielding parts.

This carefully controlled electrorefining process has produced the highest purity material in the world. PNNL performed ICP-MS assay on a large variety of materials including base metals and polymers, purified metals, and finished parts. Published results show that PNNL/MJD EFCu is an order of magnitude lower in U and Th

contamination than the next cleanest material measured with ICP-MS[1]. The values

reported for MJD EFCu are as low as <0.029 x 10^{-12} g_{Th}/g_{Cu} and <0.008 x 10^{-12} g_U/g_{Cu}[1].

These limits are beneath experiment requirements of 0.075 x 10^{-12} g_{Th}/g_{Cu} and 0.024 x 10^{-12} g_U/g_{Cu}[4].

2.3.5 Minor Alloying Element

Radiopurity and increase in hardness over current PNNL EFCu are the main

considerations in selecting an element with which to alloy Cu. Background requirements

restrict elements that are reactive or have radioactive progeny. For radiopurification

through electrorefining the selected minor alloying element must have a half cell

potential significantly lower than to U and Th as calculated using the Nernst

Equation (Eq. 2.25)[32]. This approach eliminates alloying elements such as Be, which

greatly increases the strength of Cu but has a reduction potential 0.142 V higher than that

of Th (Table 2.2)[38]. Even at extremely low electrolyte concentrations, U and Th will

reduce at E^o_{Be} and decrease deposit radiopurity.

Potential minor alloying elements which satisfy design requirements are Ni and

Cr. Both have standard potentials in the appropriate range, lack radioactive isotopes or

long-lived daughters, and are fiscally viable. Ni is FCC and isomorphous in Cu as shown

in Cu-Ni phase diagram in Fig. 2.4, creating a substitutional Cu-Ni alloy with solid

solution strengthening. The metallic radius of Ni is 2.3% from that of Cu[39], resulting in

almost strain-free lattice matching. Without high stress concentrations, large quantities

of Ni alloying element is needed for significant strength increases. For a 23 wt% Ni alloy

the electrical resistivity is increased to 180 ohm/cir mil ft and the thermal conductivity is

reduced to 0.35 W/cm/°C[40]. Ni's plating potential is 0.58 V higher than Cu,
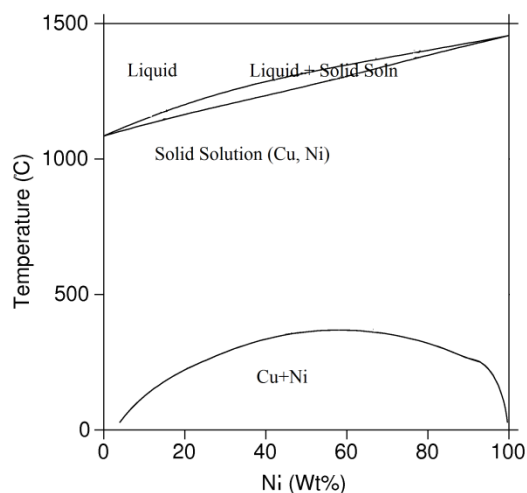
Figure 2.4: Cu-Ni Phase Diagram

although still 1.40 V and 1.59 V less than U and Th (Table 2.2). Therefore, U and Th

will not thermodynamically reduce at E^o_{Ni} for any possible present concentration. The

probability, however, of depositing contaminating species increases with the relatively

long time the Ni voltage needs to be applied make a high wt% Ni alloy.

As seen by the Cu-Cr phase diagram shown in Fig. 2.5, which contains a eutectic

point, Cr strengthens Cu through precipitation hardening. Large BCC Cr lattice misfit

with Cu causes high strength increases from small volumes of Cr coherent precipitates.

The longest-lived radioisotope of Cr is 51 at 27.7 days[37, 41, 42] with a Q value of 752.62

KeV and gamma energy of 320.084 KeV[42]. The standard potentials of Cr are 0.76 –

1.23 V higher than Cu and 0.9 - 2.93 V lower than U, Th (Table 2.2). The maximum

solubility of Cr in Cu reported is 1.83 wt% Cr at 1077 ^{o}C[43]. This maintains Cu's desired

thermal and electrical properties while improving mechanical properties and limiting the

introduction of new impurities driven to co-deposit with Cr. Cu-Cr alloys maintain

electrical conductivity of >80% IACS[44, 45, 46]. Therefore, Cr was selected as the minor

alloying element.
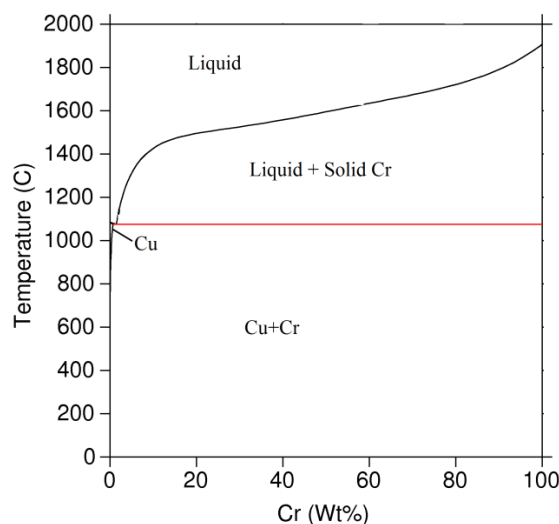
Figure 2.5: Cu-Cr Phase Diagram

2.3.6 Cr Oxidation States

Cr has two oxidation states which are commonly electrodeposited: +3 and +6 [47,

48, 49]. The bath chemistry, reduction potential, and deposit structure are different for each

valence.

Trivalent Cr oxidizes to hexavalent Cr in the presence of sulfate ions and will not

plate from a copper sulfate ($CuSO_4$) bath[38]. Cr^{3+} electrolyte solutions contain ligands

such as formic acid (HCOOH) or urea ($CO(NH_2)_2$). These complexing agents are to

prevent Cr from forming the esa-aquo complex $[Cr(H_2O)]^{3+}$ from which kinetically no Cr

can reduce[38, 48]. Carbon from the complexer co-plates with Cr in amorphous chromium-

carbide deposits[47, 49]. C itself has long-lived radioisotopes[50]. These organic ligands

may also complex and co-deposit with radioimpurities. Negatively charged metal ions

may complex with Cr^{3+} in the absence of suitable ligands to form stable complexes[38].

Therefore, to alloy Cr^{3+} using the current EFCu process, a duel-bath set-up would have to be used. For these reasons the trivalent Cr ion is excluded as an alloying candidate.

Hexavalent Cr based electrolytes are selected for this work. Although common in hard chrome plating, Cr^{6+} is a carcinogen and highly regulated[47]. It will not co-electrodeposit with other metal ions and there is no literature showing research into co-plating or plated Cr^{6+} alloys. A Cr^{6+} electrolyte consists of chromic trioxide and a catalyst such as sulfuric acid[32]. A sulfuric acid electrolyte is currently used in the Cu electroforming process and attainable radiopurity has been well characterized[8].

Similar to Cr^{3+}, Cr^{6+} is stable in solution as a complex and not as a metal ion as in the Cu^{2+} system. Cr has the proposed overall deposition reaction[51]:

$$Cr_2O_7^{-2} + 14H^+ + 12e^- \rightarrow catalyst \rightarrow 2Cr_s + 7H_2O. \tag{2.30}$$
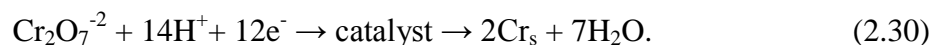
The Cr^{6+} ion is plated from a separate electrolyte than Cu to prevent complexation restricting reduction[32, 49]. Unlike Cr^{3+}, the Cr^{6+} complex reduces to a pure Cr solid. The actual series of reactions to reduce Cr_2O_7 is still unknown and the source of much debate[32, 49, 51]. The overall reduction potential must be empirically determined and is not generally stated by researchers in the literature who instead reference the current density. The potentials of possible reaction steps are known and used as an upper limit on overall potential. These reduction potentials are more electronegative than that of hydrogen, resulting in a current efficiency (CE) of only 10-20% as H^+ simultaneously gains electrons. This causes relatively long Cr plate-times with low yield. This can be offset by raising the current density[49], which as previously stated risks radiocontaminant inclusion. The low CE does not greatly effect overall Cu-Cr alloy deposition time because of the low wt% Cr required.

2.3.7 Dual Electrolytic Cell Method

Cu and Cr electrorefined deposits are plated in alternating layers from separate electrolyte baths then heat treated to produce a Cu-Cr alloy. Processes involving both Cu and Cr plating set-ups must be considered to produce high-purity deposits suitable for plating uniform subsequent layers.

2.3.7.1 Cu Bath

PNNL has spent decades developing the current electroforming method that was used to produce Cu for the MJD. This process involves dissolving high purity ($>\_99.995\%$) oxygen-free high conductivity (OFHC) Cu anode nuggets in Fisher Scientific Optima grade 1.0 M sulfuric acid (H_2SO_4) to produce a $CuSO_4$ electrolyte[1, 17]. Electrolytic bath materials are composed of nitric acid (HNO_3) leached polypropylene (($C_3H_6)_n$), high-density polyethylene (($C_2H_4)_n$), and polytetrafluoroethylene (($C_2F_4)_n$). Cu is grown on HNO_3-passivated 316-stainless steel cylinders such as shield mandrels which are 23" long and 13" in diameter[17]. Electroplating baths are covered, blanketed with nitrogen to exclude radon adsorption[1, 7], and operated in a 1000 class cleanroom to prevent dust particle contamination. Cu is plated to a thickness of approximately 1.4 cm thick at a rate of 36 - 64 um/day[4] using a custom-designed Dynatronix reverse pulse programmable power supply[17]. All MJD Cu is plated underground (UG) to prevent cosmogenic activation forming ^{60}Co through neutron spallation. Plating cleanrooms are located at PNNL's shallow UG laboratory with 50 ft overburden and at SURF with a 4850 ft overburden[1].

The MJD EFCu baths are run under galvanic control at a set bias voltage of 0.380 VDC. Impedance of connections lowers this to ~0.32 VDC at the electrode surface. Current is controlled by optima grade H_2SO_4 additions to raise solution conductivity. Conductivity is held between 200 - 230 mS/cm^2, where under 180 mS/cm^2 current is insufficient to deposit at a noticeable rate. Current response under set conditions is ~16 A for the standard shield mandrels previously mentioned. The applied voltage follows a periodic-reverse pulse waveform with off-time. This waveform (1) inhibits extensive columnar growth improving surface morphology and (2) allows relaxation in which mass-transfer driven radiocontaminants may be moved away from the cathodic region through solution convection.

The PNNL Cu electroforming method provides radiopure deposits sufficient for MJD use but lacking appropriate topography for this work. To alloy EFCu with electroplated Cr a Cu surface morphology upon which Cr may be evenly plated has to be obtained. H_2CrO_4 solutions have very low covering/throwing power and are very sensitive to current interruptions[32]. High substrate roughness can result in discontinuous Cr layers and inhomogeneous alloy composition. For this work the EFCu bath variables were investigated.

2.3.7.2 Cr Bath

A simple Cr^{6+} electrolyte consists of a Cr ion source, an acid radical catalyst such as sulfuric acid, and water[32]. The ideal Cr^{6+}:SO_4^{2-} ratio is 100:1[32, 49, 52] although concentration ratios between 80:1 and 130:1 are used in industry. The Cr ion continuously polymerizes in solution through olation, producing complexes dependent upon Cr concentration as shown by the reactions[49]

$$4HCrO_4 \rightarrow Cr_4O_7{}^{2-} + 2H_2O \quad 0.01 < C_{Cr} < 1 \text{ M} \tag{2.31}$$

$$3Cr_2O_7{}^{2-} + 2H \rightarrow 2Cr_3O_{10}{}^{2-} + H_2O \quad 1.5 < C_{Cr} < 3.5 \text{ M} \tag{2.32}$$

$$4Cr_3O_{10}{}^{2-} + 2H \rightarrow 3Cr_4O_{13}{}^{2-} + H_2O \quad 7.5 < C_{Cr} < 10 \text{ M.} \tag{2.33}$$
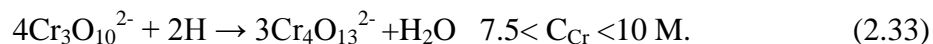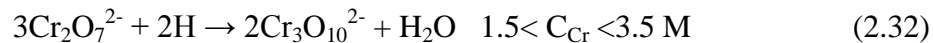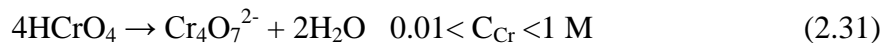
Solution concentrations of Cr, C_{Cr}, typically used were 1 - 4 M, with the ideal being 2.5 M and resulting in the $Cr_2O_7{}^{2-}$ active ion. The $HSO_4{}^-$ ion serves to protect the $Cr_2O_7{}^{2-}$ dichromate ion from complexing and forming trivalent $Cr(H_2O)_6{}^{3+}$, which cannot be reduced. The sulfate blocks one end of the trichomate ion shown in Fig. 2.6 to prevent the Cr^{3+} complex from forming while leaving the other end open to allow complex reduction reactions. Too low of a $Cr^{6+}:SO_4{}^{2-}$ ratio blocks both ends of the Cr complex and prevents reduction[32, 49].

$$
\begin{array}{c}
\text{O} \\
\parallel \\
\text{O} \quad \text{O} \quad \text{O} \leftrightarrow \text{H} \leftrightarrow \text{O} - \text{S} - \text{O}^{-} \\
\parallel \quad \parallel \quad \parallel \\
\text{O}^{-} - \text{Cr} - \text{Cr} - \text{Cr} - \text{OH} \\
\parallel \quad \parallel \quad \parallel \\
\text{O} \quad \text{O} \quad \text{O} \leftrightarrow \text{H} \leftrightarrow \text{O} - \text{S} - \text{O}^{-}
\end{array}
$$
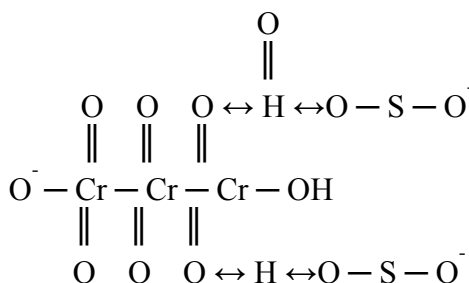
Figure 2.6: Ideally protected Cr(VI) complex

Cr-ion additions are typically made using the chromic trioxide metal salt $Cr(VI)O_3$. This can be purchased in the same purity grades as $CuSO_4$ salt. PNNL found that U and Th electrolyte concentrations using high-purity $CuSO_4$ salts were too high to produce required deposit radiopurity. OFHC Cu anode nuggets of 99.99% purity were substituted to minimize U, Th in the bath. This method results in acceptable U, Th concentrations in deposits. The rejection rate of U, Th from electrolyte in Cu deposits remained constant independent of initial concentration in the ranges tested[8, 9, 10, 17].

Cr-ions may likewise be added to an electrolyte solution using high-purity $Cr_{(s)}$ anodes. Cr is insoluble in sulfuric acid solutions and would not dissolve without being driven to oxidize through anodic current. The Cr anodic dissolution efficiency is 85-100%; whereas, the cathodic reduction efficiency is only 10-20%[49]. Therefore, Cr anodes would quickly over-concentrate the bath.

Upon applying overpotential to a H_2CrO_4 plating cell an insoluble cathode film forms[32, 49]. This catalytic film reduces the activation energy of the final partial reduction reaction of Cr-complexes passing through it. The Cr complex will only reduce under the assistance of this sulfate-rich cathodic film, which forms at a different potential than the reduction reaction. The postulated reduction sequence is modeled by

$$Cr^{6+} \rightarrow Cr^{3+} \rightarrow Cr^{2+} \rightarrow Cr^0. \tag{2.34}$$

although the precise mechanism involved is unknown[32].

Active materials, which adsorb H^+ and provide an ion source to the electrolytic cell, can function as anode materials. Metal alloy anodes are used in Cr cells but slowly dissolve into the acidic solution, reduce bath purity, and have to be periodically replaced. Lead oxide or graphite anodes are more often chosen, although inert anodes such as platinum and iridium will not dissolve and may be used[51, 53].

Anode material selection affects CE and plating times. Side electrochemical reactions, such as hydrogen evolution and partial Cr reduction, decrease current contribution to the full Cr^{6+} to $Cr_{(s)}$ reduction. CE is given by

$$CE = Q_j / Q_{total} \tag{2.35}$$

where Q_j is the charge in Coulombs used in the reaction of interest and Q_{total} is the total charge passed for all processes.   For electroplating it is more useful to consider weight w_j of metal deposited,

$$CE = w_j / w_{Faraday} = w_j / (A_{wt} Q / n F) \qquad (2.36)$$

where $w_{Faraday}$ is the Faradaic weight and A_{wt} is the atomic weight for the metal of interest[32].

In H_2CrO_4 electroplating baths, Cr^{3+} ions form at the cathode where only partial Cr^{6+} reduction occurs[51],

$$Cr_2O_7^{2-} + 14H^+ + 6e^- \rightarrow 2Cr^{3+} + 7H_2O. \qquad (2.37)$$
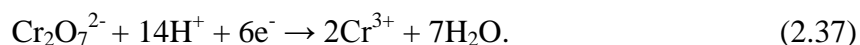
Cr^{3+} will not reduce further. At a 3+:6+ ratio of 1:25 , Cr^{3+} overpopulates the bath and prevents any deposition[54]. In the presence of inert anodes baths must be periodically regenerated to reoxidize any Cr^{3+}[51]. Lead anodes passivated to lead oxide PbO_2 will catalyze the reaction[51]

$$2Cr^{3+} + 3O_2 + 6e^- \rightarrow PbO_2 \text{ catalyst} \rightarrow 2CrO_3. \qquad (2.38)$$
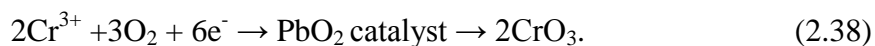
There are published methods for passivating lead to produce PbO_2 layers with varying resistance to dissolution[54].

2.3.8 Cu-Cr Adhesion

In industry Cu and Cr electrodeposited layers are plated using an intermediate such as Ni and additives to level and shift deposition potential. An acidic sulfate solution also is not typically used because of galvanic corrosion. Ni improves poor adhesion caused by lattice mismatch, low mutual solubility, and galvanic corrosion. The addition of Ni to the Cu electrolyte would raise the concentration of radiocontaminants in solution and the duty cycle percentage of electronegative potentials driven as discussed in § 2.3.5.

To ensure a radiopure alloy, only binary solid solutions are considered and neither complexing agents nor Ni intermediates are used in this work. Alternative methods must be used to increase the adhesion between Cu, Cr alternating layers.

2.3.8.1 Galvanic Corrosion

The significantly more noble plating potential of Cu than Cr results in galvanic corrosion which is the major contributing factor to non-adherent Cu deposits on Cr. When the Cr plated mandrel is exposed to Cu ions in solution an extensive displacement reaction occurs[55]. The half-cell reactions for Cu

$$Cu^{2+} + 2e^- \rightarrow Cu_s \, , \, E^o = 0.34 \text{ V vs. SHE} \tag{2.39}$$

and for active Cr

$$Cr^{6+} + 6e^- \rightarrow Cr_s \, , \, E^o = -0.63 \text{ V vs. SHE} \tag{2.40}$$

using the overall half-cell Cr^{6+} reaction potential which assumes an activity coefficient of one (Table 2.2). The Gibbs energy for the total reaction

$$Cr_s + 3Cu^{2+} \rightarrow Cr^{6+} + 3Cu_s \, , \, E^o = 0.97 \text{ V vs. SHE} \tag{2.41}$$
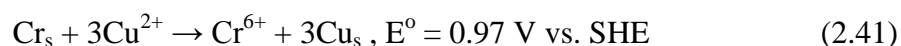
is calculated by

$$\Delta G^o = -nFE^o. \tag{2.42}$$

The resulting negative Gibbs energy change indicates spontaneous Cr dissolution at the cathode. This pushes out the plane of closest Cu^{2+} approach, preventing adhesive subsequent Cu electroplated layers.

The adhesion is increased by closing the potential gap to prevent cathodic Cr oxidation. Complexing agents can be used to change the activity of $CuSO_4$ electrolytes, increasing the reduction potential to improve adhesion. These complexing agents are chains of organic ligands which raise radioactive backgrounds. The increase in reduction

potential at which the dominant alloy mass is plated also increases probability of depositing radiocontaminants. Therefore, complexing agents cannot be considered for this work.

Passivating the Cr is another method of closing the potential gap by effectively raising its nobility, as seen in a typical Electromotive Force (EMF) series such as the abridged list shown in Table 2.3[56]. Active Cr-baring SS lies at the bottom and passive at the top. Cr can be passivated by exposure to HNO_3. The produced Cr oxide passive layer is only a few monolayers thick but is hard and non-reactive; therefore, it prevents Cr from dissolving.

Table 2.3: EMF Series

Reactivity	Metal/Alloy
Stable	Pt
	Au
	Passivated SS 11-30 wt% Cr
	Passivated Ni
	Cupronickels
	Cu
	Ni
	SS 13 wt% Cr
	Fe
Active	Cr

2.3.8.2 Nucleation Mechanisms

The first step of electrolytic deposition is specific adsorption or nucleation[57]. Cu electroplates through the following steps[55] shown in Fig. 2.7:

1. Epitaxial Nucleation
2. Island growth

3. Polycrystalline continuous film growth

Cu nucleation mechanisms dictate interfacial energy between the growing Cu crystal and Cr substrate. Interfacial Energy affects Cu's adhesion to Cr. For homogeneous Cu nucleation the energy is described by Gibbs energy of Formation

$$\Delta G = -NzF|\eta| + D(N) \tag{2.43}$$

where N is number of atoms and D is the total surface excess energy and a function of interfacial energy[55].
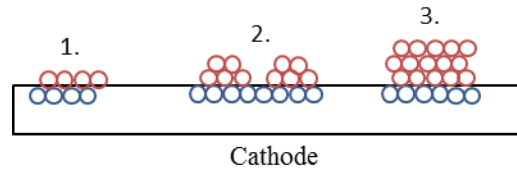
Figure 2.7: Crystal growth

2.3.8.3 Current Density

The structure and quality of Cu deposits depend on nucleation parameters. The substrate surface preparation and texture affect epitaxial nucleation. The nucleation density is a function of current density, where applying a higher current will result in more nucleation sites[55, 57]. The critical atomic cluster size N* to nucleate is given by

$$N^* = \frac{8hv_m^2\sigma^3}{27(nF|\eta|)^3} \tag{2.44}$$

where v_m is the atom volume, h is a geometry constant, and σ is the average surface energy. This shows the overpotential driving force η is inversely related to the necessary cluster size. Increasing nucleation density, therefore, improves initial coverage. The resulting initial coverage affects interfacial defects and energy, which contribute to adhesion as shown in Eq. 2.43.

2.3.8.4 Chemical Etching

Etching the Cr layer before setting in a $CuSO_4$ bath changes the Cr surface energy and increases the number of energetically favorable Cu nucleation sites. This can improve adhesion and lead to more uniform growth resulting from higher surface coverage. Cr dissolves in HCl according to the reaction

$$Cr_{(s)} + 2\ HCl \rightarrow Cr^{2+} + 2\ Cl^- + H_{2(g)}. \tag{2.45}$$
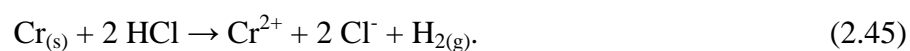
Cr is not soluble in typical strong acids such as HNO_3, which instead passivate and protect it, or in H_2SO_4, which only dissolves the Cr oxides.

2.4 Precipitation Alloying of Cu-Cr

Precipitation hardening is used to alloy systems containing a eutectic phase transformation, such as the Cu-Cr binary system. The eutectic point is an invariant point where liquid, single-solid, and two-solid phases meet in equilibrium. The phase diagram for the Cu-Cr system (Fig. 2.5) shows the eutectic temperature at 1077 °C. This is below the melting point of pure Cu at 1084.87 °C. Maximum Cr solubility in Cu occurs at the eutectic temperature, at which reported values vary greatly from 0.61 to 1.83 at.% Cr. This inconsistency is reportedly due to the use of different experimental methods and presence of metal impurities in solubility determination samples [43].

The equilibrium solubility X(Cu,Cr) of Cr in Cu at a given temperature is modeled by[43]

$$Ln\ X(Cr, Cu) = \frac{\Delta S(Cr,Cu)}{R} - \frac{\Delta H(Cr,Cu)}{RT} \qquad (2.46)$$

where ΔH is the change in enthalpy for 1 mol Cr in Cu and ΔS is the partial molar excess entropy of Cr in Cu. Experimental literature values for Cr solubility in Cu at 1000 °C are 0.98, 0.48, and 0.49 at.% Cr[43].

Precipitating hardening is a three-step process consisting of

1. Solution Treating

2. Quenching

3. Age Hardening.

2.4.1 Solution Treating

During solution treatment the temperature is raised into the single-solid phase region of the phase diagram at 800 to 184.87 °C (Fig. 2.5)[43]. This results in a Cu-Cr

solid-solution with a temperature dependent Cr concentration. Cr is driven into the Cu matrix by concentration gradient as described by Fick's Second Law for non-steady state diffusion which models net flux of atoms from high to low solute regions. The one-dimensional Fick's Second Law is[24]

$$\frac{dC}{dt} = D_M \left(\frac{d^2C}{dx^2}\right) \qquad (2.47)$$

where C is the concentration in mass/vol, D_M is the diffusion coefficient of solute in solvent, and x is the depth diffused. The general solution using dimensional analysis is[58]

$$C = a_{erf} * erf\left(\frac{x}{2\sqrt{(D_M t)}}\right) \qquad (2.48)$$

where a_{erf} is an integration constant. The error function is defined as

$$Erf(Z) = \left(\frac{2}{\sqrt{\pi}}\right) \int (e^{-y^2}) dy \qquad (2.49)$$

for which Z and y values are tabulated. Alternating Cu-Cr electroplated layers act as a diffusion couple for which the solution to Fick's Law becomes[24]

$$C = \frac{c_1 + c_2}{2} - \left[\frac{c_1 - c_2}{2}\right] erf\left[\frac{x}{2\sqrt{(D_M t)}}\right] \qquad (2.50)$$

where c_1 and c_2 are concentrations of metal of interest in respective coupled layers.

The solute atomic flux follows as[59]

$$j = -D^* \left(\frac{dC}{dx}\right) + <v>_F C + v_k C \qquad (2.51)$$

where $<v>_F$ is the atom drift velocity, c is solute concentration, and v_k is the local lattice plane velocity. From this the diffusion coefficient D^* for Cr in Cu is given by the Arrhenius type experimentally determined equation[59],

$$D^* = 0.78 \exp(-53.5 \text{ kcal mol}^{-1} / RT) \text{ cm}^2/\text{s} . \qquad (2.52)$$

At 1000 °C, $D^* = 5.086 \times 10^{-10} \text{ cm}^2/\text{s}$.

Common methods of Cu-Cr alloying in research and industry are casting/forging[44], rapid solidification through melt spinning[45, 58], and high pressure torsion[46]. All of these methods produce well mixed Cu, Cr regions. These processes use solution treating to dissolve the regions of Cr into the Cu matrix, not needing to diffuse Cr any significant distance. For a diffusion couple the Cr layer has to diffuse the length of the entire plated Cr layer to produce a homogenous alloy. This necessitates longer solution treating times than otherwise used. The hardness resulting from various Cu-Cr alloying methods is listed in Table 2.4. The stated ASM solution treating time for Cu-Cr alloys is 30 min/inch material. Temperatures used are 980 to 1010 ^{o}C[60].

Table 2.4: Literature values for Cu-Cr binary alloy hardness

Referance	Peak Hardness (HV)	T_{age} (^{o}C)	T_{age} (hrs)	Wt% Cr	Method
Jin[44]	112	400	3	15	hot forged and cold rolled
Olofinjanaa[61]	380	400	1	6	melt spinning (highest ever reported)
Proca[62]	120	450-475	4.5-5	0.5 – 1.2	extruded and solution treated 2 hrs (Romanian standard STAS 11532-87)
Vinogradov[63]	162	375	1	0.36	equal-channel angular pressing
	150	-	-	0.9-1.3	Unknown, From Yamaha Corp

2.4.2 Quenching

The Cu-Cr solid solution is rapidly cooled to room temperature after diffusion to trap dissolved Cr in a supersaturated mixture. The critical cooling rate to prevent Cr mobility for the Cu-Cr system solution treated at 800 to 1000 ^{o}C is 17 to 20 ^{o}C/sec. Therefore, a solution treatment at 1000 ^{o}C must be quenched to 25 ^{o}C in less than 48 to 57 sec. Experimentally it is also reported that higher cooling rates result in lower possible

hardening. It was postulated that this is from discontinuous precipitation at grain boundaries which embrittle age-hardened specimens[64].

Quenching media include water, oil, and various gases. Radiopurity concerns in this work exclude use of an oil quench. Both high purity de-ionized water and select inert gas atmospheres are suitable. N has a nitriding effect on Cr producing brittle CrN which negatively affect the produced alloy's mechanical properties[65], and was not considered. Gas conductivities at 300 K are listed in Table 2.5, showing that the thermal conductivity of Ar is considerably lower than other gases at 23.2302 $(mW \cdot m^{-1} \cdot K^{-1})$ [66], reducing the possible quench rate.

Table 2.5: Thermal conductivities of gases of interest

Gas	Thermal conductivity $(mW \cdot m^{-1} \cdot K^{-1})$
Nitrogen	32.7694
Argon	23.2302
Oxygen	32.5491
Air	32.6062

2.4.3 Cu – Cr Age Hardening

After quenching, Cu-Cr samples are artificially aged to precipitate Cr particles out of the supersaturated Cu matrix. The precipitation sequence is [44, 67, 68]

1) Cr-rich cluster

2) coalescence to Cr Guinier-Preston (GP) Zone

3) nucleation into coherent (metastable) BCC phase

4) incoherent (stable) BCC phase and coarsening

The precipitate nucleation barrier $\Delta G*$ and critical radius $r*$ from classical nucleation theory are[23]

$$\Delta G* = \left(\frac{16\pi}{3}\right)\frac{\gamma^3}{\Delta G_n + \Delta G_{el}} \tag{2.53}$$

$$r* = 2\gamma/\Delta G_n \tag{2.54}$$

for interfacial energy γ, ΔG_n driving force and ΔG_{el} elastic energy. The interfacial energy of incoherent Cr precipitates is reported at 625 mJ/m^2. The time-independent driving force is the chemical volume Gibbs energy change[23, 44, 69] given by

$$\Delta G_n = \left(\frac{RT}{V_\beta}\right)X_\beta \ln\left(\frac{X_{Cr}}{X_\alpha}\right) \tag{2.55}$$

where X_{Cr} is atomic fraction of Cr in Cu, X_α is coherent solubility of Cr, and V_β is the Cr-phase molar volume. The classical method considers energy required to nucleate 100 at.% Cr particles. For dilute alloys such as Cu-Cr it is more accurate to consider a critical nuclei composition which produces minimal nucleation barrier energy. Chbihini found this value to be 45 at.% Cr[23]. The driving force for the dilute solutions approximation is

$$\Delta G_n{}^{NC} = \left(\frac{RT}{V_\beta}\right)\left[\frac{2}{T/T_{critical}}\left(X_\beta - X_{Cr}\right)^2 - \left(X_\beta \ln\left(\frac{X_\beta}{X_{Cr}}\right) + \left(1 - X_\beta\right)\ln\left(\frac{1-X_\beta}{1-X_{Cr}}\right)\right)\right] \tag{2.56}$$

where X_β is Cr molar fraction and $T_{critical}$ the critical nucleation temperature [23]. Kamijo calculated the critical size of homogeneous Cr precipitate nucleation to be 1 nm at 400 ^{o}C in a Cu-0.6 at.% Cr alloy[44].

As nucleation and subsequent particle growth lower the supersaturated concentration of Cr in the Cu matrix a concentration gradient between precipitates arise[69]. Lifshitz-Slyozow-Wagner (LSW) classical theory uses Fick's law to describe particle growth assuming the distance between particles is much greater than the diameter of particles. According to the Gibbs-Thompson effect, for dilute Cr in Cu alloys

$$C_r^{Cr} = C_\infty^{Cr} \exp\left(\frac{2\gamma V_m}{rRT}\right) \qquad (2.57)$$

where C_r^{Cr} and C_∞^{Cr} are the concentrations of solute Cr at the particle interface and in the

Cr bulk, r is particle radius, and V_m is the molar volume of the Cr precipitate phase. This

shows that the driving force for Cr diffusion from the matrix to a dilute Cr particle

depends on the interfacial energy. The result is Ostwald ripening, where Cr from smaller

particles diffuse to larger particles to lower the total interfacial energy by increasing the

volume to surface area ratio. The growth rate of coarsening particle is

$$\frac{dr}{dt} = \frac{D}{r} \cdot \frac{C - C_r^{Cr}}{C_{precip}^{Cr} - C_r^{Cr}} \qquad (2.58)$$

where D is the concentration-independent diffusion coefficient, C is the instantaneous

concentration of solute Cr in the matrix, and C_{precip}^{Cr} is the concentration of Cr in the

precipitate[69, 70]. As shown in the above equations, particle radius growth rate is

dependent upon interfacial energy. The lattice misfit between incoherent BCC Cr

precipitates and the FCC Cu matrix increases the particle's interfacial energy, resulting in

rapid Cr precipitate coarsening.

BCC Cr precipitates initially form in the highest density Cu planes with both

Nishiyama-Wassermann (NW) and Kurdjumov-Sachs (KS) orientation relationships

(OR). NW is described by[71, 72, 73]

plane $\{111\}_{fcc}$ || $\{110\}_{bcc}$, direction $<0\bar{1}1>_{fcc}$ || $<001>_{bcc}$.

KS is described by[71, 72]

$\{111\}_{fcc}$ || $\{110\}_{bcc}$ and $<1\bar{1}0>_{fcc}$ || $<1\bar{1}1>_{bcc}$.

During aging the KS-OR precipitates grow at the expense of NW precipitates [23],

minimizing the interfacial energy through Ostwald ripening[24]. Cr precipitates also

possess high lattice misfit in the Cu matrix, raising the strain energy and aging

precipitates rapidly. Overaged precipitates have a KS-OR which is manifested as elongated rods in FCC Cu[44].

The ASM stated Cu – 1 wt% Cr precipitation treatment is listed as 400 to 500 $^{\circ}$C for a minimum of 4 hrs[60]. Reported values for aging times and temps producing maximum hardness using various alloying methods is shown in Table 2.4. Cr precipitate nucleation calculated from the Modified Borelius Model requires an aging temperature of 300 $^{\circ}$C for nucleation of a 1 nm precipitate. Precipitates have not been imaged under 475 $^{\circ}$C. Peak conductivity does not occur under the same aging conditions as peak hardening[44, 46], and one measurement must be sacrificed for the other.

2.4.4 Furnace Atmosphere Considerations

Furnace atmosphere selection is critical to producing usable heat treated specimens. High concentrations of oxygen during solution treatment will cause Cu scaling, which results in gross loss of mass[60]. Cr oxidizes easily to a passive layer which protects it from further oxidation at low temperatures. As the temperature continues to increase the passive layer becomes transpassive and breaks down allowing extensive oxidation[56]. Cu-Cr samples heat treated under protective atmospheres must be cooled in that atmosphere to below 65 $^{\circ}$C to prevent oxide formation[67].

The oxidation reactions occurring during Cu-Cr alloying are

$$2Cu_{(s)} + 0.5O_{2(g)} = Cu_2O_{(s)} \tag{2.59}$$

$$2Cr_{(s)} + 01.5O_{2(g)} = Cr_2O_{3(s)}. \tag{2.60}$$
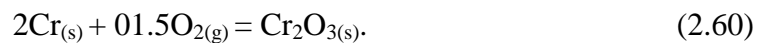
Gibbs energy is used to calculate concentration of O_2 allowable in furnace atmosphere. According to Gaskell the standard Gibbs energy change ΔG_o is given by[57]

$$\Delta G_{o,\,Cu} = -162,200 + 69.24T, \ \ T = 298\text{-}1356 \text{ K} \tag{2.61}$$

$$\Delta G_{o,\,Cr} = -1,110,100 + 247.3T, \quad T = 298\text{-}1793 \text{ K}. \tag{2.62}$$

The Gibbs energy change is

$$\Delta G = \Delta G_o + RT \ln (K_p) \tag{2.63}$$

At equilibrium $\Delta G = 0$ making equilibrium constant K_p become

$$K_p = \exp (-\Delta G_o / RT). \tag{2.64}$$

The equilibrium constant for product activies a_{prod} and reactant activities a_{react}

$$K_p = [\Pi\, a_{prod} / \Pi\, a_{react}] \tag{2.65}$$

which is calculated for pure solids at unity activity $a = 1$. Calculated oxygen pressure P_{O2} values show that Cr oxide formation in the transpassive region is more thermodynamically favorable than Cu oxide. Therefore, furnace atmosphere must be controlled according to P_{O2} for Cr.

N_2 and H_2 gases are commonly chosen for metal heat treating furnace atmospheres. They are non-oxidizing and non-reactive for most metals and considered inert. However, they both dissolve into the Cu matrix, affecting the alloy[74]. As briefly mentioned in § 2.4.2, N_2 has a nitriding effect on Cr [65]. Resulting CrN particles are larger than the Cu lattice sites they occupy, causing lattice distortions. To lower energy their energy, these particles segregate to grain boundaries. CrN particles' elastic constant is different than Cu's causing high stress concentrations under plastic deformation. This eventually leads to microcracking and intergranular failure [19].

H_2 acts as a reducing atmosphere according to the reactions

$$H_2 + Cu_2O = 2Cu + H_2O \tag{2.66}$$

$$3H_2 + Cr_2O_3 = 2Cr + 3H_2O. \tag{2.67}$$

The Ellingham Diagram shows ratios of $H_2 : H_2O$ at 1000 ^{o}C for Cu to be 1 : $10^{3.8}$ and for Cr to be $10^{3.5}$: $1^{[34]}$. This reduces oxidation while allowing P_{O2} in the furnace to be much higher. H_2 is explosive above 8 vol%[67], and is regulated to 4% use at United States federal facilities.

Actual inert gases which cannot react with metal being heat treated are Argon and Helium[74]. Ar possesses a high specific heat capacity of 0.52 kJ/kg/K allowing for more even heating. The thermal conductivity of Ar is low at 23.2302 mW/m/K resulting in slow temperature rise[75]. The attainable purity of boil-off Ar is very high, but it is more expensive than other gas options.

3. EXPERIMENTAL METHODS

3.1 Cu Cell Investigations

Eight Cu electrolytic baths of the type shown in Fig. 3.1 were constructed to study Cu cell parameters. Fischer Optima grade acid 2 L Teflon bottles were cut in half, and the bottom halves were purposed as bath cells. Three 1/2" wide titanium anode connection strips per bath were bent to fit from bottom of bath through slits made in an added cell lid. An average of 41 cylindrical 99.995 % pure OFHC Cu nuggets, with average surface area of 3.7 in^2 lined the walls of the bath to form the anodes, making contact with all three Ti strips. Polypropylene (PP) 2.555" diameter Industrial Netting ridged mesh tubes were positioned centrally in the baths, separating cathode and anode regions. Thomas Scientific ½" glass stir bars were placed on 316 SS disks in the center of mesh tubes to provide perturbation. All plastic components were rinsed in 2 % Micro90 followed by deionized (DI) water. They were then leached in ACS grade 6 M HNO$_3$ for 72 hrs prior to constructing baths. Cu anode nuggets were etched in ACS grade 6 M HNO$_3$ and double rinsed with DI water immediately prior to setting in a cell.

(a)   (b)   (c)
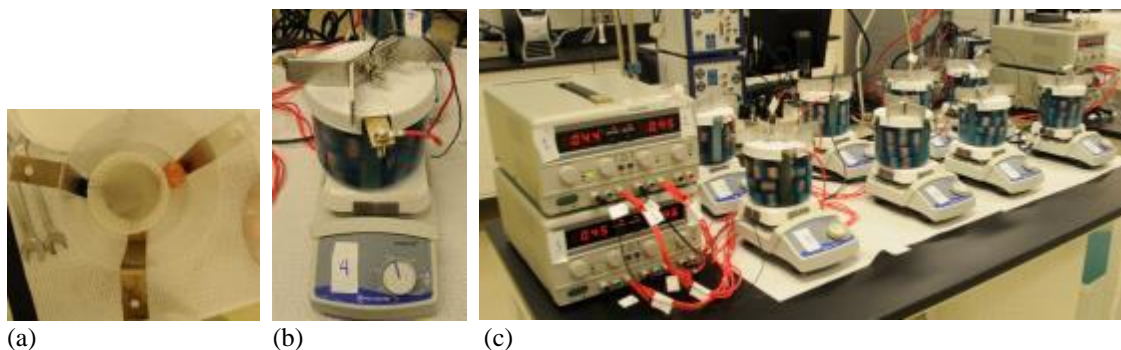
Figure 3.1: (a) Construction of Cu plating cell (b) completed Cu plating cell (c) entire Cu plating run

Five gallons of $CuSO_4 \cdot 5(H_2O)$ electrolyte was initially taken from the PNNL
Shallow Underground electroforming bath waste electrolyte. $CuSO_4$ standards were
made and absorbance was measured with a Cole-Parmer 1200 Unico spectrophotometer
to construct a calibration curve (Appendix C). Initial electrolyte absorbance was
measured to be 0.620 at 810 nm. Concentration of $CuSO_4$ from this was calculated to be
5.058 g_{Cu}/L. A Hatch SC1000 conductivity probe was calibrated using a 463.3 mS/cm
solution and initial electrolyte conductivity was measured at 54.9 mS/cm. Electrolyte
was placed in a filtration system where it was pumped continuously through a 1 um PP
filter. Conductivity was raised by adding H_2SO_4.

A Cu trial plating bath filled with 515 ml electrolyte was operated on a GW Instek
GPC-1850D DC power supply set to 0.45 V voltage control. A 316 SS mandrel with
dimensions 89.01 x 19.06 x 1.15 mm was rinsed with 2 % Micro90, 6 M HNO_3, and DI
water before setting in the cell. Potential drop across the electrodes was measured at 0.40
V with a Fluke Digital Multimeter, and the current response averaged to 0.62 A over the
course of the run. The bath ran for 21.75 hrs. The resulting deposits were very rough.
Filtering electrolyte was diluted by adding 300 ml Fisher Scientific ACS grade H_2SO_4
and 6 L DI water. This brought the concentration to 2.31 g_{Cu}/L and the conductivity to
225.3 mS/cm.

$CuSO_4$ cell parameters were varied to correlate with deposit structure and surface
morphology. Eight Cu baths ran simultaneously under identical conditions for each
variable investigated until reproducibility was established, after which four identical
baths per parameter were used. SS mandrels were rinsed with 2 % Micro90 and wiped
with ACS grade HNO_3 before each run, independent of other mandrel preparation used.

Voltage drop at electrode surface was measured for each run. Electrolyte absorbance,

deposit weight, deposit measurements, and photographs were taken after each run.

A total of 11 runs with eight baths apiece deposited Cu under varied plating

conditions. Cell parameters varied were flow rate, electrolyte conductivity, $CuSO_4$

concentration, mandrel surface preparation, current, and plating potential. Room

temperature electrolyte was measured at 19.1 $^{\circ}$C. Table 3.1 shows parameter values.

Table 3.1: Cu run parameters

Run	Variable	Value
1	concentration	2.31 g_{Cu}/L
	stir rate	350 RPM
	mandrel prep	none
	concentration	224.5 mS/cm
	voltage	0.44 V
2	concentration	2.77 g_{Cu}/L
3	mandrel prep	220 grit sand full
		220 grit sand half
4	stir rate	525 RPM
5	stir rate	700 RPM
6	concentration	1.15 g_{Cu}/L
		0.072 g_{Cu}/L
7	voltage	0.34 V
8	mandrel prep	280 grit
9	same as 6	220 grit
10	voltage	0.25 V
25	conductivity	304 mS/cm

Run 1 was set with baths 1 to 8 to determine a deposit quality baseline with

adjusted filtering electrolyte and no further mandrel preparation. The concentration of

$CuSO_4$ was raised to 2.77 g_{Cu}/L for all baths in Run 2 while maintaining other

parameters. Stainless steel cathode strips for Run 3 baths 1, 2, 6, and 8 were sanded on

all edges with 3M Wetordry 220 grit silicon carbide sandpaper before setting. Baths 3, 4,

5, and 7 cathodes were sanded on only one edge, which was marked. For Run 4 the stir rate was increased from 350 to 525 RPM and all cathode edges were sanded with 220 grit. In Run 5 the stir rate was again increased to 700 RPM. The stir rate in Run 6 was returned to 525 RPM, and mandrel edges were sanded with 220 grit followed by 400 grit. Baths 1 to 4 electrolyte was diluted for to a concentration of 1.15 g_{Cu}/L. Conductivity was raised to 217.0 mS/cm by adding 49.5 ml H_2SO_4 to 3 L of diluted electrolyte. Baths 5 to 8 electrolyte was further diluted to 0.61 g_{Cu}/L. The lowered $CuSO_4$ electrolyte concentrations for baths 1 to 4 and 5 to 8 were maintained through Run 7. Conductivity was brought up to 215.3 mS/cm by adding 59.5 ml H_2SO_4 to 3 L electrolyte. The voltage in Run 7 was reduced to 0.34 V from 0.44 V, dropping current from an average 0.55 A to 0.31 A. All Run 8 cathodes were ground with 280 grit paper while electrolyte and operating parameters were kept the same as Run 7. Run 9 mandrel edges were ground with 220 grit paper while operating parameters were the same as Run 6. Voltage was again reduced to 0.25 V in Run 10 and 280 grit mandrel preparation was returned to. The parameters were varied by a factor of one between any given run.

3.1.1 Temperature Studies

The effect of temperature on Cu deposits was determined. $CuSO_4$ 500 ml baths were operated under the following approximate heightened temperatures: 35, 40, 50, and 65 ^{o}C. Two Teflon baths per run were heated on corning stirring hot plates as shown in Fig. 3.2. Temperature was measured with an Accumet Ag/AgCl reference electrode attached to an Accumet AB150 pH/mV module.

$CuSO_4$ 100 ml baths were operated under the following lowered temperatures: 10 and 0 ^{o}C. Three baths per run were cooled in a Fisher Scientific Isotemp 3006 chiller

circulating 5 L DI water with 50 ml propylene glycol as shown in Fig. 3.2b. Plating

times, exact temperatures, and current response for all temperature varied Cu runs are

listed in Table 3.2.

(a)   (b)
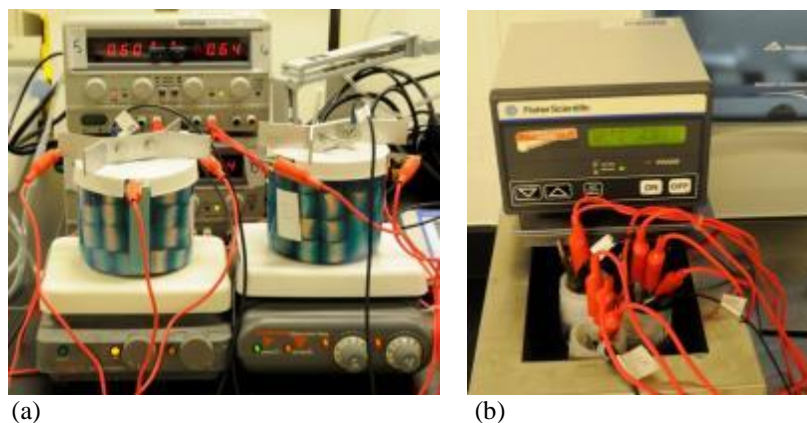
Figure 3.2: (a) Heated Cu plating run baths 1 and 2 (b) cooled Cu plating baths L1 to L3

Table 3.2: Cu temperature runs plating parameters

Run	Bath	Duration (hrs)	Running Parameters		
			I (amps)	$V_{measured}$ (V)	T (^{o}C)
24	1	23.78	0.72	0.229	38.3
	2		0.76	0.237	51.6
25	1	25.68	1.02	0.257	37.1
	2		1.02	0.216	63.4
	3	25.37	0.21	0.242	22.8
	4		0.21	0.177	21.9
26	L1	20.73	0.03	0.253	12.5
	L2		0.05	0.260	12.5
	L3		0.02	0.268	12.5
27	1	19.18	0.58	0.246	36.0
28	L1	30.38	0.01	0.246	3.0
	L2		0.04	0.272	3.0
	L3		0.01	0.273	3.0
29	1		0.01	0.230	64.9

3.1.2 Pulse-Plating

The effect of voltage pulses on Cu deposit structure was examined. Three 100 ml CuSO$_4$ plating cells were set up with 19 mm wide 316 SS mandrels, Ti anode connections, and a single Cu anode nugget for pulse-plating. Cathode edges were sanded with 280 grit paper and surface area was taped to 1277.7 mm^2. Repeating chronoamperometry scans plated Cu at 0.34 V with a frequency of 1 Hz and duty cycle of 80 %. The cycle was restarted every 30 min, when the maximum number of data points was reached. Deposits underwent a total of 35 cycles constituting 12.4 hrs of forward plating time.

All additional higher-frequency plating cycles were controlled by the Gamry Virtual Front Panel Potentiostatic in square-wave mode. Two 100 ml CuSO$_4$ pulse-plating baths were operated for each of the following frequencies: 10, 100, and 1000 Hz. Baths were operated at 0.34 V with an 80 % duty cycle and 275 RPM stir rate. Plating durations are listed in Table 3.3.

Table 3.3: Cu pulse-plating runs operation values

Run	Bath	Duration (hrs)	Freq (Hz)
22	1	12.5	1
	2		
	3		
23	1	41.62	10
	2	302.85	1000
	3	96	100
24	1	77.07	10
	2	96.2	100
	3	94.4	1000

3.1.3 Current Step Waveform

The effect of stepping the current density on dendrite concentration was investigated. Cu Run 20 was set as a control and operated at a constant current. Subsequent Runs 21, 20b, 21b, 8b, and 9b were performed with an increased initial current step. Selected step durations are listed in Table 3.4, all possessing the same step amplitude. Each run contained six to eight baths apiece. Table 3.4 shows cell parameters for the five step-current runs and one control constant-current run.

Table 3.4: Cu current step waveform amplitude and duration

Run	I_1 (A)	t_1 (min)	I_2 (A)	t_2 (hrs)
20	-	-	0.4	37.88333
21	0.8	5	0.40	41.75
20b	0.8	10	0.40	48.98
21b	0.8	10	0.40	45.57
8b	0.8	5	0.45	54.23
9b	0.8	5	0.50	57.05

3.1.4 Flow Rate Determination

Flow rate corresponding to stir rate RPM was measured. Neutrally buoyant BnR Tackle Soft Beads orange spherical beads were placed in a 1 L Teflon bath containing anode nuggets and mesh tube as shown in Fig. 3.3. A ½" Teflon stir bar was placed on SS disk in the center of the mesh tube. $CuSO_4$ electrolyte with concentration 1.95 g_{Cu}/L was added to the bath. For each stir rate the bath was stirred until bead motion reached a steady state. A video was taken in slow motion of moving beads. The following stir rates were recorded: 1500, 1100, 700, 525, 350, 275, and 125 RPM.

Figure 3.3: $CuSO_4$ flow rate determination

3.1.5 Cu Deposit Characterization

Plated Cu deposits were weighed, measured, and photographed. Roughness was determined using a Keyence VHX-5000 Digital Microscope. Specimens from each run were sectioned with a Buehler Isomet 15 HRC precision saw blade, mounted to show both cross section and plan view, and polished. A 1:1:0.3 $NH_4OH : H_2O : H_2O_2$ (3 %) etch was used to reveal grain boundaries. Micrographs were taken on the Keyence 500F digital microscope and grain size was measured. Vickers micro-hardness indents were made using a 200 g force on a Leco LM-247AT hardness indenter.

3.1.6 Analytical Examinations

Analytical charge-transfer measurements were made for various $CuSO_4$ cell parameters. Cu baths with 100 ml electrolyte, inert Ir coated SS anodes, an Ag/AgCl reference electrode, and 1 cm^2 316 SS disk cathodes were constructed. SS cathodes were polished to a mirror finish using the polishing procedure described in Appendix B before measuring each peak. Fig. 3.4 shows SS disks fitted into a polytetrafluoroethylene (PTFE) rotating disk electrode (RDE) holder attached to a Gamry Instruments RDE710.

Cells were purged with N_2 before each experiment for a minimum of 10 min until the electrodes were bubble-free. N_2 gas blanketed the cells for the extent of each experiment.
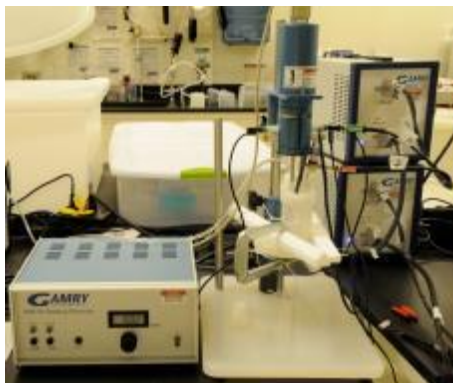
Figure 3.4: Rotating disk electrode

A $CuSO_4$ electrolyte cell with concentration 1.95 g_{Cu}/L was used to perform cyclic voltammetry (CV) measurements from 0 to -0.75 V and 0 to -1.5 V vs. Ag/AgCl using a 15 sec equalization time. CV curves were measured on stationary electrodes at room temperature with no stirring at the following scan rates: 10, 36, 100, 625, and 2500 mV/s. A ½" Teflon stir bar was positioned 1.25" below the cathode and peaks were determined using a scan rate of 100 mV/s for the following stir rates: 60, 125, 350, and 700 RPM. Pre-heated and pre-cooled electrolyte was added to the cell for varied temperature plating studies. Temperature was monitored with the reference electrode and module. CV curves were recorded at 100 mV/s for the following temperatures: 12.7, 19.1, 36.7, 41.3, and 46.3 $^{\circ}$C. Polarization curves were measured from 0 to -1.5 V using the RDE at 10 mV/s for the following rotation rates: 25, 100,144, 225, 324, 400, and 1600 RPM.

RDE studies were investigated at 225 RPM on electrolyte at the following temperatures: 12.7, 19.1, 36.7, and 46.3 $^{\circ}$C

CuSO$_4$ electrolytes at concentrations 0.65, 1.28 , and 3.26 g$_{Cu}$/L were prepared along with 0.75 M H$_2$SO$_4$ supporting electrolyte. CVs scans were recorded for all four electrolytes at 100 mV/s with no stirring at room temperature (19.1 $^{\circ}$C). Polarization Curves were recorded for the four electrolyte concentrations using the RDE at 225 RPM with a scan rate of 10 mV/s from 0 to -1.5 V vs. Ag/AgCl.

Tafel slopes were recorded at 0.25 V +/- E$_{OC}$ on Cu electrolyte with concentration 4.36 g$_{CuSO4}$/L. The scan rate was set at 1 mV/s with a 2 sec sampling period. Chronocoulometry (CC) curves were measured for the step V$_0$ = 0 V, V$_1$ = -0.6 V, and V$_2$ = 0.11 V. Each step was applied for 10 sec. The corrosion potential was monitored for 200 sec. All analytical electrochemical curves were performed on the supporting electrolyte blank in addition to CuSO$_4$ electrolytes.

3.2 Cr Cell Investigations

Three sets of Cr plating cells were constructed with which to examine Cr cell parameters. Baths O1 to O4 contained 750 ml of electrolyte as shown in Fig. 3.5. These cells were constructed from the bottom halves of Optima grade 2 L Teflon acid bottles. The cathode was positioned centrally centrally and anodes radially. The electrode separation was set at 6 cm. Glass ½" stir bars were placed in middle of baths, under the cathode. Baths L1 to L4, shown in Fig. 3.6, were assembled from 100 ml Savillex PerFluroAlkoxy (PFA) vials. Plastic lids contained slits separating electrodes 1.5 cm and Fisherbrand ½" Teflon stir bars were placed at the bottom of each cell. Baths L5 to L8 were composed of 30 ml vials with lids identical to those of Bath L1 to L4 and contained ¼" Teflon stir bars. All plastic components were leached for 72 hrs in 6 M HNO_3 prior to assembling. Electrolyte was filtered before filling the cells.
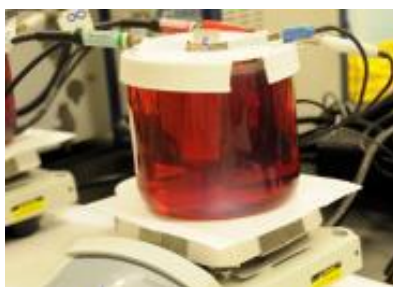
Figure 3.5: O-series 750 ml Cr plating cells

Figure 3.6: Two 30 ml Cr plating cells (left) and one 100 ml Cr plating cell (right)

H_2CrO_4 electrolyte was prepared using 1 kg Alfa Aesar 99 % pure $Cr(VI)O_3$, 13.16 g ACS grade H_2SO_4, and 5.5 L DI water. The solution was circulated through a 1 um PP filter for three days before using. Conductivity was measured to be 559 mS/cm^2. Spectrophotometer maximum wavelength was found at 490 nm for the light yellow solution resulting from a 1:350 dilution. Standards were prepared for the latter and a calibration curve was measured (Appendix C).

Four Gamry Reference 600 and Four Reference 3000 Potentiostats were calibrated using a dummy cell. All baths were connected to potentiostats using banana clips. A set of experiments proceeded with the cell inside and outside a Gamry VistaShield Faraday Cage. Signal noise differences were not noticed and subsequent experiments were operated without the cage. Before each plating run CVs were cycled at 100 mV/s until steady state was reached. The corrosion potential was monitored.

Cathodes composed of 1.27 cm wide 316 SS and rolled Cu strips of unknown purity were purposed for initial Cr cell investigations. Cathode surface area was controlled with PTFE tape. An initial plating trial on a 6 M wiped Cu cathode strip produced no growth. Successive cathodes were rinsed in 2 % Micro90 followed by DI water before setting. Plated Cr deposits were weighed and photographed.

H_2CrO_4 cell parameters were investigated for correlation with deposit finish, throwing power, covering power, current efficiency, and plating voltage. Variables studied were cell volume, flow rate, anode material, electrode ratio, Cr concentration, temperature, and current density. A total of 34 runs with five baths apiece allowed correlation of deposited Cr characteristics with different plating conditions.

Select representative deposits were sectioned, mounted cross-sectionally, polished, and micrographed on the 5000x Keyence. Thickness, adhesion, and cracking were examined. Micrographs were taken of the deposit surface. Vickers micro-hardness indents were made with a 200 gf load on three representative Cr samples per surface finish. Resulting indents were measured and micrographed.

3.2.1 CrO_3 Concentration Studies

The effect of CrO_3 concentration on deposited Cr and Cr cell response was examined. Filtering electrolyte with concentration 107.83 g_{Cr}/L was diluted with DI water to concentrations 65.96, 49.81, and 27.64 g_{Cr}/L while maintaining CrO_3:SO_4 ratio. Cells L1 to L4 were filled with the prepared electrolyte. Cu cylindrical cathodes 6.32 mm in diameter taped a surface area of 1,990.24 mm^2 and cylindrical Ir anodes with the same surface area were rinsed with Micro90 and DI water before setting in baths. Bath L2 is shown during the run in Fig. 3.7. CVs were taken before the run. Cells were potentiostatically controlled. Voltage for each run was set to CV peak potential. Baths were active until electrolyte became spent. Times, current, and voltage for each Cr electrolyte concentration shown relative to initial, undiluted concentration are recorded in Table 3.5.
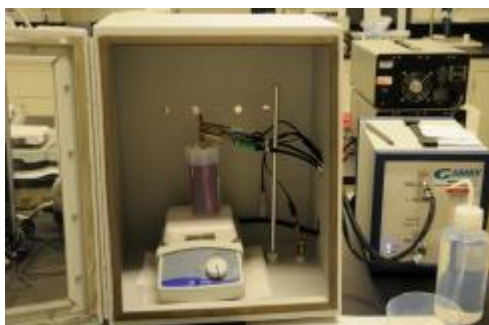
Figure 3.7: Cr concentration determination run bath L2

Table 3.5: H_2CrO_4 electrolyte Cr concentration determination running parameters

Bath	Cr Conc. (g_{Cr}/L)	Relative Cr Conc. (%)	Voltage (V)	Current (A)	Run Time (hrs)
L1	65.96	75	2.1	0.2041	18.28
L2	49.81	50	2.44	0.3997	17.58
L3	27.64	25	2.31	0.1665	10.00
L4	107.83	100	2.43	0.1602	18.00

Following concentration examinations, filtering electrolyte was diluted to 56.42 g_{Cr}/L. The well-mixed electrolyte was removed from the filtration system and bottled in cleaned 2 L Teflon acid bottles. This is considered stock H_2CrO_4 electrolyte. All following plating baths start with this solution.

3.2.2 Current Density Studies

Current density relation to potential and deposit surface finish was investigated for current densities from 0.03 to 0.87 A/cm^2 over the course of 34 runs. Smooth rolled Cu cathodes were taped to ensure uniform surface area for all baths in a run. Baths were driven galvanically and set current was calculated for desired from current density.

Run 13 applied a two-step current to baths. Current was spiked to 0.15 A for 10 sec before lowering to 0.05 A for 3 hrs. Cell volumes 30 ml and 100 ml with identical electrode spacing were operated using PbO_2 anodes.

3.2.3 Temperature Studies

The effect of temperature on Cr deposit structure and plating current density range was investigated. A 267 ml Kocour Ceramic Hull cell was filled with stock H_2CrO_4 as shown in Fig. 3.8, using fresh electrolyte for each plate. Electrolyte was pre-cooled using

the chiller before filling and was in-situ and pre- heated on the hot plate for heightened T experiments. Temperature was monitored using the Ag/AgCl reference electrode. A PbO$_2$ anode sheet was cut to fit the width of the anode slot. A rolled Cu sheet was similarly cut 96.43 mm long to fit the cathode slot. The cell was connected with banana clips to a DC power supply. For each temperature the Hull cell was driven for 4 min at 5 A under current control.

Figure 3.8: Heated ceramic Hull cell

3.2.4 Flow Rate

The effect of flow rate on Cr cell response and deposit quality was investigated. Stir rates 0, 125, 275, and 350 RPM were examined in baths L5 and L7. Smooth rolled Cu cathodes and Pb anodes were set in baths. Electrodes were taped to a 1:1 electrode surface area ratio. Pre-run CVs were taken under each flow rate with fresh stock electrolyte. Baths were set to plate for 2 hrs at voltage of CV peak.

Flow rate corresponding to stir rate RPM was measured. Neutrally buoyant orange spherical beads were placed in a 100 ml Savillex bath. A ½" Teflon stir bar and stock electrolyte were added to the bath. Electrolyte partially filled the bath. For each stir rate the bath was stirred until bead motion reached a steady state. Fig. 3.9 shows a still image from the video taken in slow motion of moving beads, which was used to

determine flow. The following stir rates were recorded: 125, 275, 350, 525, and 700

RPM.

Figure 3.9: H_2CrO_4 flow rate determination

3.2.5 Electrode Considerations

The suitability of the following Cr cell anode materials was studied: Cu, Cr, PbO_2,

and Ir. Corrosion potential between electrodes was monitored and CV peaks were

measured.

PbO_2 anodes were passivated from Pb using oxidation voltages and times listed in

Table 3.6. Pb sheets of unknown purity and origin were cleaned in a 10% HNO_3 rinse for

20 min. They were cut to various strip sizes for use as cathodes. Strips were connected

to a potentiostat and mounted in a 100 ml 3M H_2SO_4 solution containing cell vs. an Ir

counter electrode. The quality of oxidation layer was determined using corrosion

potential scans and CVs.

Titan Metal Powders 99.5 % pure aluminothermic Cr chips were investigated as

Cr anode material. Chips and nuggets vacuum induction melted from the Chips were

placed in connection to a single inactive Ti anode connection strip within the cell. For

study of Cu anodes, anode materials consisted of a single Cu nugget connected to a Ti

strip. The nugget was etched in 6 M HNO_3 and double rinsed in DI water. Prepared Ir

coated SS rod anodes were wiped with dilute HNO_3 before setting.

Table 3.6: PbO_2 anode passivation voltages and durations

Anode	V (v)	Time (s)
Pb L1	0.4	10800
	2.8	20
	1.7	28800
Pb L5; L6	0.4	10800
	2.3	15
	1.7	28800
Pb L7; L8	0.4	10800
	2.3	30
	1.7	28800
Pb L3; L4	0.4	10800
	2.3	45
	1.7	28800
Pb L3,2; L4,2	2.3	60
	1.7	54000
	1.7	54000
Pb A5; A7	0.4	10800
	2.3	120
	1.7	2880
Pb B2	1.3	10800
	4.7	30
	3.6	28800

3.2.5.1 Electrode Ratio

The effect of electrode ratio on plating voltage, current efficiency, and deposit

quality was examined. The following anode : cathode electrode ratios were set with

PbO_2 anodes and rolled Cu cathodes: 1:1; 5:2; 3:1; and 5:1. Electrodes were PTFE taped

to dictate surface area. Chronopotentiometry (CP) scans were monitored at constant

current density j=0.030 A/cm^2 and CVs were measured.

3.2.5.2 Partial Cr Oxidation

Methods listed in Table 3.7 were employed to reoxidize over-concentrated Cr^{3+} electrolyte resulting from Cr plating runs. Oxidation runs were investigated at a range of Cr concentrations, current densities, temperatures, and electrode materials. Spent electrolyte for investigations was initially partially reduced by applying a forward voltage until no charge-transfer peak was distinguishable. Voltage response during subsequent oxidation runs was monitored. CVs were taken both before and after oxidation trials.

Table 3.7: Cr-oxidation investigation parameters

Cathode	Cathode Sa (mm^2)	Anode	Anode Sa (mm^2)	Bath	I (A)	Increased Temp (^{o}F)
Ir	97.75	Ir	2022.62	L2	-2.00	
Ir	97.75	Ir	2022.62	L3	-1.00	100
Ir	97.75	Ir	2022.62	L4	-2.00	
Cu	97.75	Ir	2022.62	L2	-2.00	100
Ir	99.47	Ir	2022.62	L1	-1.00	100
Cu	99.47	Ir	2022.62	L3	-1.00	
Cu	99.47	Ir	2022.62	L4	-1.00	
Ir	99.47	Ir	2022.62	L1	-0.43	
Cu	99.47	Ir	2022.62	L4	-1.00	145
Cu	99.47	Ir	2022.62	L3	-0.43	
Ir	98.68	Ir	2022.62	L4	-0.43	
Cu	99.47	Ir	2022.62	L3	-0.43	200
Ir	99.47	Ir	2022.62	L1	-0.43	
Ir	67.51	Ir	2022.62	L1	-0.43	
Ir	67.51	Ir	2022.62	L1	-0.43	
Ir	67.51	Ir	2022.62	L2	-0.43	
Ir	67.51	Ir	2022.62	L4	-0.43	
Ir	67.51	Ir	2022.62	L2	-0.43	
Ir	857.13	Pb	6453.56	L1	-0.269	

The four Cr electrolyte concentrations shown in Table 3.8 were investigated. Influence of Ir and PbO_2 anodes against Ir and Cu cathodes was studied, as shown for

each experiment listed in Table 3.7. Various electrode ratios were examined by PTFE

taping the cathode. Baths shown in Fig. 3.10a were operated both at heightened

temperature using a hot plate, and at room temperature. Fig. 3.10b shows Ir electrodes

post-oxidation run. The cathode is taped to a surface area $1/40^{th}$ of that of the anode.

The effect of Ir and PbO_2 anode materials on Cr^{3+} oxidation during normal plating

conditions was monitored through examination of oxidation charge-transfer peaks on pre-

and post-run CVs.

Table 3.8: Cr^{3+}-overconcentrated electrolyte Cr Concentrations

Bath	C_{Cr} (g/L)
L1	79.37
L2	52.82
L3	27.37
L4	110.57

(a)   (b)
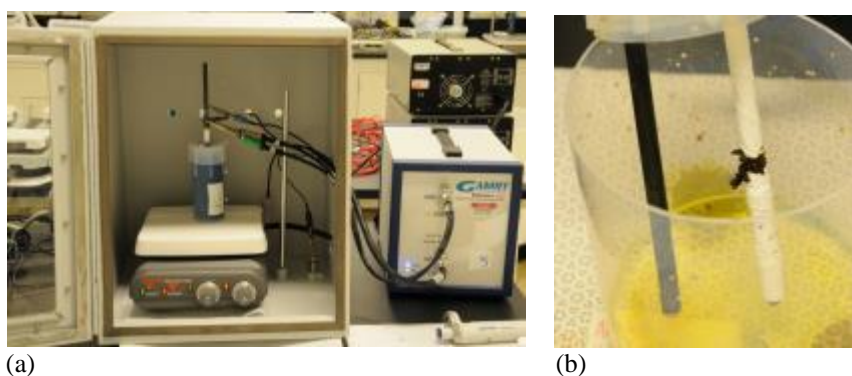
Figure 3.10: (a) Spent bath L2 re-oxidation (b) post-oxidation run Ir anode (left) and cathode (right)

3.2.6 Analytical Examinations

The overall reduction and half-cell potentials for the overall Cr(VI) reduction

sequence was investigated. A 100 ml 1 M H_2CrO_4 solution was prepared by mixing

10.0078 g $Cr(VI)O_3$ with 130 ul H_2SO_4 and balance DI water. CV curves were measured

on the cell using an Ir anode, polished 1 cm^2 cathode, and Ag/AgCl reference electrode. The experiment was repeated using stock Cr Electrolyte.

Analytical charge-transfer measurements were made for selected H_2CrO_4 cell parameters. Four 100 ml cells were set up one at a time with an Ir anode, Ag/AgCl reference electrode and 1 cm^2 polished 316 SS disk cathode on the RDE. SS cathodes were polished to a mirror finish before measuring each peak. Cells were purged with N_2 before each experiment for a minimum of 10 min until the electrodes were bubble-free. N_2 blanketed the cells for the extent of each experiment.

A Cr cell containing stock electrolyte with concentration 56.42 g_{Cr}/L was examined with CVs from -0.4 to -1.5 V vs. AgCl using a 15 sec equalization time. Four CV peaks apiece were measured on stationary electrodes at room temperature with no stirring at the following scan rates: 9, 10, 36, 64, 100, 144, 225, 625, and 2500 mV/s. A ½" Teflon stir bar was positioned 1.25" below the cathode and the cell connected to RDE was placed on a stir plate. Peaks were determined using scan rate 10 mV/s for the following stir rates: 0, 60, 125, 350, and 700 RPM. The electrolyte was heated with a hot plate and cooled with a chiller to take CVs at 10 mV/s for the following temperatures: 9.5, 19.1, 26.6, and 34.4 ^{o}C. Table 3.9 shows RDE rotation speed with associated scan rate for polarization curves measured in RDE studies.

Table 3.9: Cr RDE polarization curve parameters

RDE Rotation Rate (RPM)	Scan Rate (mV/s)
1000	100
	10
8100	10
	5
10000	5
	1

H_2CrO_4 electrolytes at concentrations 79.50, 39.36, and 23.27 g_{Cr}/L were prepared. Supporting electrolyte consisting of 100 ml of 0.025 M H_2SO_4 was prepared by mixing 130 ul H_2SO_4 with balance DI water. CV curves were measured on all four electrolytes at 10 mV/s with no stirring at room temperature (19.1 ^{o}C). Tafel slopes were recorded at 0.25 V +/- E_{OC}, 1 mV/s with a 2 sec sampling period on 56.42 g_{Cr}/L and supporting electrolyte. Corrosion potential was monitored for 200 sec. All analytical electrochemical curves were recorded on the supporting electrolyte blank in addition to H_2CrO_4 electrolytes.

3.3 Cu-Cr Electrodeposition

Cu-Cr alloy electrodeposition was studied for both single and dual electrolyte cells.

3.3.1 Cu-Cr Single Bath

Viability of a single electrolyte Cu-Cr plating cell was preliminarily examined. Cu and Cr SO_4^{2-} based electrolyte plating baths were prepared. Three Cu : Cr concentration ratios were prepared by mixing filtered $CuSO_4$ electrolyte of concentration 1.45 g_{Cu}/L with stock H_2CrO_4 of concentration 56.42 g_{Cr}/L . Baths L6 to L8 were prepared for Cu-Cr Runs 1 to 3, and baths L2 to L4 for Runs 4 to 7. Ir anodes and rolled Cu cathodes of equal taped surface area were set in cells connected to potentiostats. Cu-Cr Runs 1 to 3 were controlled galvanically, and Runs 4 to 7 were controlled potentiostatically. Three baths were run per electrolyte for each condition. CVs and corrosion potential scans were taken before plating. Current density, voltage, and concentration values are given in Table 3.10. Deposits were weighed, photographed, and the surfaces were micrographed.

Table 3.10: Cu-Cr single electrolyte runs plating parameters

Run	C_{Cr6+} (g/L)	C_{Cu2+} (g/L)	Relative Elyte Conc. (%)	j (A/cm^2)	V (V)	Time (hrs)
1	14.11	1.09	75% Cu/25% Cr	0.03		24
2	28.21	0.73	50% Cu/50% Cr	0.03		12
3	42.32	0.36	25% Cu/75% Cr	0.03		12
4	14.11	1.09	75% Cu/25% Cr		0.34	12
5	14.11	1.09	75% Cu/25% Cr		0.7	12
6	14.11	1.09	75% Cu/25% Cr		1.4	6
7	14.11	1.09	75% Cu/25% Cr		2.01	6

3.3.2 Cu-Cr Dual Bath

CuSO$_4$ plating baths developed in § 3.1 and H$_2$CrO$_4$ baths developed in § 3.2 were used for the dual Cu-Cr electrodeposition set-up as shown in Fig. 3.11. Cu was plated with DC power supplies under bias voltage to a thickness of 2.00 mm to 3.55 mm on ground, passivated, and rinsed SS mandrels. Deposits were plated under conditions investigated and described in § 3.1 to produce an average Cu surface roughness r = 18 um lacking dendrites.

Figure 3.11: Cu plating baths C5 - C8 (left) and Cr plating baths O1 - O4 (right)

The surface area of Cu deposits was calculated prior to plating the Cr layer. A roughness factor based upon Keyence 5000 digital microscope measurements was included into surface area calculations. For galvanically controlled Cr runs, current was set independently for each mandrel such that current density was equivalent across all mandrels in the run.

Prepared plated Cu mandrels were set in 750 ml H$_2$CrO$_4$ baths and plated for 12 hrs to thickness approximately 10 to 40 um at j = 0.03 A/cm^2. Fig. 3.12 shows layered mandrels with Cr plated on deposited Cu (Fig. 3.12a), and the subsequent Cu layer plated on Cr (Fig. 3.12b). Cr baths were driven by Gamry potentiostats. CVs and corrosion potential scans were completed before each run. A total of 25 runs with four baths (O1 to

O4) apiece deposited Cr on electroplated Cu. Upon completion of each Cr run, deposits were rinsed, their surface prepared for Cu deposition, and returned to Cu cells.

(a)   (b)
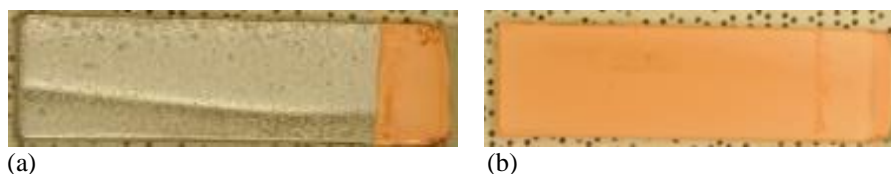
Figure 3.12: Dual cell layered Cu-Cr (a) Cu-Cr layers (b) Cu-Cr-Cu layers

The second Cu layer was plated to an average of 2.18 mm under current-control on DC power supplies. The surface area value calculated for each cathode's Cr plating step were used in this successive Cu plating step. Current was set for uniform current density across each run. Investigated variations in current density and surface preparation are described in § 3.3.2.2.

All deposits were weighed, measured, and photographed between each plating step. Select final deposits underwent further heat treatment (§ 3.4) or were sectioned, mounted, polished and photographed without HT.

3.3.2.1 Stir Rate Determination

Two Cu mandrels, 7.24Jun15 and 8.1Jul15, plated in Cu Run 7 at 0.34 V and Run 8 at 0.25 V, respectively, were taped to restrict the surface area to 780 mm^2 and set in Cr baths L3 and L4. The average plated Cu roughness was measured as described in § 3.1.5 before setting. Baths were set with PbO_2 anodes and stock H_2CrO_4 electrolyte, and operated galvanically at 0.2 A. The voltage response under the following stir rates was measured: 0, 350, 525, and 750 RPM. Deposits were weighed, photographed, mounted cross-sectionally, polished, and micrographed.

3.3.2.2 Cu on Cr Adhesion Studies

Investigated parameters affecting adhesion of Cu plated onto Cr are shown in Table 3.11. Five runs with four baths apiece plated Cu in baths L1 to L4 onto Cr plated rolled Cu cathodes. Ti anode connections with one Cu anode nugget apiece were set in Cu baths. $CuSO_4$ electrolyte of concentration 1.45 g_{Cu}/L and conductivity 226.4 mS/cm was used for all adhesion runs. Duplicate samples were produced for each parameter. Cells were operated in current-control on DC power supplies. The effect of the following Cr finishes was investigated: bright, milky, and frosty. The effect of the following surface preparation techniques was examined for each Cr finish: DI water rinse and 6 M HNO_3 rinse. The following surface preparation techniques were examined only on the bright Cr finish: 10 % H_2SO_4 rinse and 50 % HCl rinse. All acid etches were followed by a DI water rinse. Increased initial current density was applied to bright plated Cr cathodes in conjunction with and without the 6 M HNO_3 rinse.

All deposits were weighed, measured, photographed, and surface micrographs imaged. Deposits were sectioned, mounted cross-sectionally, polished, and micrographed. The thickness of deposits was measured to be less than 5 mm.

Two methods of measuring adhesion were employed. ASTM D 3359a Adhesion Tape Test was used to assess plated Cu adhesion to Cr. An X was made across plated Cu and tape lying across a section was pulled back at approximately a 180° angle. The second method was to examine the interfacial region in cross-sectionally mounted samples. Presence of a Cu-Cr interface gap was noted.

Table 3.11: Cu-Cr adhesion runs parameters

Run	Cu	Cr finish	Etch	j (A/cm^2)	Time (hrs)
1	123	bright	N	0.01	4.33
	126		N		
	153		6 M HNO$_3$		
	154		6 M HNO$_3$		
2	142	frosty	N	0.01	4.33
	143		N		
	146		6 M HNO$_3$		
	147		6 M HNO$_3$		
3	36	dark	N	0.01	4.33
	63		N		
	65		6 M HNO$_3$		
	71		6 M HNO$_3$		
4	116	bright	N	0.03	1.44
	117		N		
	119		6 M HNO$_3$		
	127		6 M HNO$_3$		
5	115	bright	10 % H$_2$SO$_4$	0.01	4.33
	118		10 % H$_2$SO$_4$		
	124		50 % HCl		
	125		50 % HCl		

3.4 Cu-Cr Heat Treating

Cu-Cr annealing and precipitation alloying heat treatments were investigated.

3.4.1 Annealing

Rolled Cu cathodes plated with bright Cr were annealed at 200, 300, 400, and 500 ^{o}C in a pre-heated Thermo Scientific Thermolyne muffle furnace for 20 min. Room air atmosphere was used. Samples were slowly air-cooled. Similarly Cr plated rolled Cu samples were annealed at 200, 300, 400, 500, and 600 ^{o}C. They were quenched with water.

Bright finish Cr plated on electroplated Cu Runs 10 and 7 were annealed in air atmosphere at 200, 300, 400, 500, and 600 ^{o}C. Thinner Run 10 (avg. 0.26 mm) samples were annealed for 20 min and thicker Run 7 (avg. 0.79 mm) samples for 30 min.

All annealed samples were photographed, sectioned, and mounted for cross-sectional and plan views in Buehler VariDur Acrylic. Further metallographic sample preparation followed the polishing procedure in Appendix B.

3.4.2 Preliminary Cu-Cr Alloying Studies

Solution treatment studies to determine Cr diffusion distance were investigated on electroplated Cu-Cr layered samples. Deposits were removed from their SS mandrels by cutting along the sides of the mandrel with a precision saw. They were heat treated (HT) in the muffle furnace with Ar over-pressure followed by a water quench. Cole-Parmer or Sigma-Aldrich alumina crucibles were used. Three samples were treated for each time and temperature. Samples underwent solution treating at three times 6, 12, and 24 min and three temperatures each at 980, 1000, and 1020 ^{o}C. Solution treated samples were

sectioned, mounted in a 1:1 Epoxy : Buehler Conductive Ni filler, polished, and micrographed.

Initial precipitation studies employed the ASM suggested industrial Cu-Cr alloy solution treating time of 30 min/in. Samples measured ~0.2" thick and were soaked for 6 min. Electroplated Cu-Cr layered samples 2., 3., and 4.21Dec were solution treated in the muffle furnace at 980 ^{o}C with Ar purge and water quench before sectioning.

Solution treated and sectioned samples were age hardened at 400, 500, 600, 700, and 800 ^{o}C in the pre-heated muffle furnace for 1 hr. Samples were HT under air atmosphere and slow-cooled in the furnace to room temperature before removing. All samples were mounted cross-sectionally in Buehler EpoQuik Epoxy and polished.

Mounted annealed solution treated, and initial precipitation hardened samples were examined on the Zeiss Supra40 Secondary Electron Microscope (SEM) at South Dakota School of Mines and Technology (SDSMT). Energy-Dispersive X-ray Spectroscopy (EDX) mapped the cross-section to determine Cr diffusion distance. Charging of the epoxy on preliminary annealed samples caused image drift. Further mounts lacking Ni filler were coated with ~10 um of C before examining on the SEM/EDX.

Vickers micro-hardness indents were made in select mounted HT samples with a 200 gf load. Indents were measured.

3.4.3 Precipitation Alloying

A tube furnace set up and operated at SDSMT to solution treat Electroformed Cu-Cr (EFCu-Cr) is shown in Fig. 3.13. Ultra-high purity H_2 was passed through a Johnson Matthey HP-10 H_2 Purifier and bottled argon to form a 5 % H_2 and 95 % Ar furnace

mixture. H_2O vapor present in furnace was measured at 6.7 ppm. A heat treated trial

sample with Ar/H_2 quench showed no oxidation.

(a)   (b)   (c)

(d)   (e)
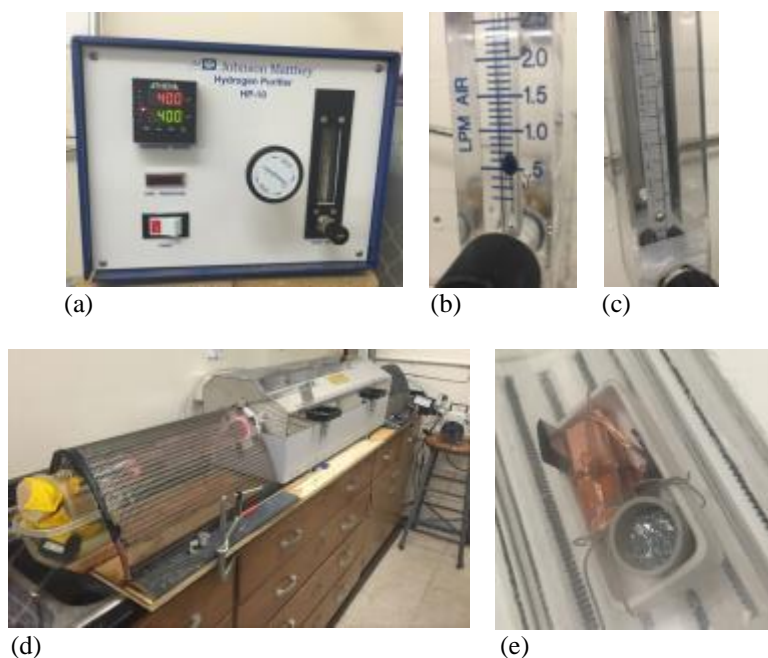
Figure 3.13: SDSMT solution treating tube furnace set-up (a) H_2 purifier (b) H_2 flow rotameter (c) Ar flow
rotameter (d) tube furnace (e) boat with Cr getter chips and Cu-Cr layered samples

Two initial EFCu-Cr samples were solution treated at SDSMT at 1000 ^{o}C for 24

hrs with Cr getter chips and previously described atmosphere and quench. These samples

were mounted, polished, and examined on the SEM. EDX line scans in the Cu-Cr

interfacial region were examined on the SDSMT Zeiss SEM. These samples were

examined a second time using EDX point and scan, over a larger area.

Eight EFCu-Cr samples an average of 61.4 x 21.3 x 1.53 mm in size were solution

treated in the SDSMT tube furnace set-up at 1000 ^{o}C for 24 hrs. Samples were sectioned

into thirds post-HT and select sections were cold rolled. Six sectioned cold-worked

(CW) EFCu-Cr samples were additionally aged at 800 ^{o}C for 12 hrs at SDSMT. All HT

samples were sent for further processing to PNNL.

A TransTemp Transparent tube furnace was set up at PNNL to age harden solution treated samples as shown in Fig. 3.14. A Parker Balston FID-1000NA Gas Station H_2-generator and building supplied boil-off Ar was connected to the tube furnace. A tantalum getter positioned near the atmosphere inlet and quartz boat containing samples were employed. Rotameters were used to meter 4 % H_2 and balance Ar into the furnace. Samples were aged at the following temperatures: 400, 500, 600, 700, and 800 ^{o}C. At each temperature samples were soaked for the following times: 1.3, 4, and 12 hrs. Two non-CW and one CW sample were aged per T and t condition listed in Table 3.12. Samples were left to cool to room temperature in the Ar/H_2-purged furnace. Precipitation hardened and solution treated samples were mounted cross-sectionally in a 1:1 epoxy : Ni filler. They were polished and micrographed.

After hardness was measured on these precipitation hardened samples (discussed later in § 3.6), an additional HT investigation was made to show possibility for increased resulting hardness. Electrodeposited Cu-Cr layered sample 4.14Mar was solution treated in the PNNL transparent tube furnace at 1010 ^{o}C for 24 hrs with the atmosphere previously described for this furnace. It was quenched in Ar/H_2 and aged at 400 ^{o}C for 12 hrs. The sample was mounted, polished, and indented.
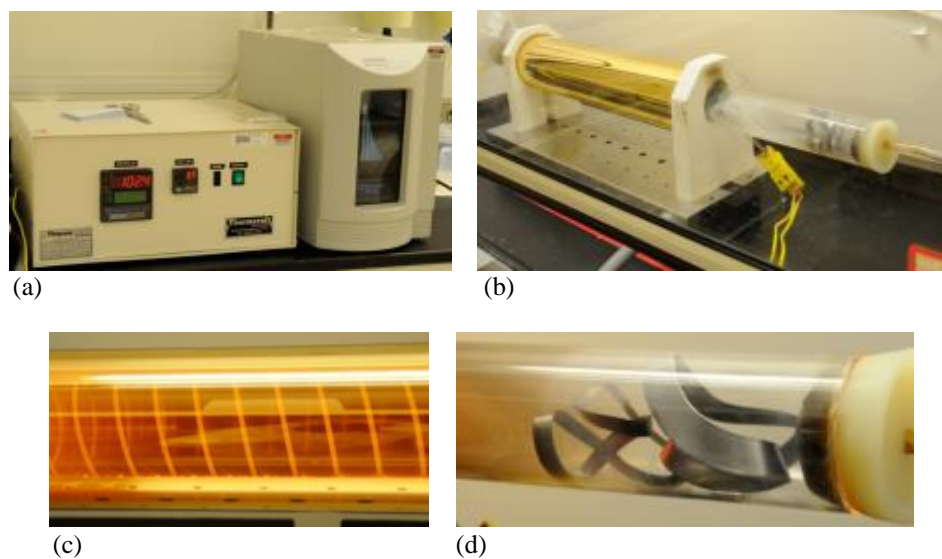
Figure 3.14: PNNL age hardening furnace set-up (a) TransTemp Transparent Tube Furnace temperature controller/programmer and H_2 generator (b) tube furnace (c) operational tube furnace (d) Ta getter foil at atmosphere inlet

Table 3.12: Age hardening heat treatment parameters and samples

Mount #	Age T (^{o}C)	Age t (hrs)	Parent Sample	CW?
1	800	4	5.14Mar16	
			2.2Mar16	
			4.2Mar16	x
2	600	12	1.22Feb16	
			4.22Feb16	
			2.2Mar16	x
3	700	4	1.22Feb16	
			3.14Mar16	
			2.2Mar16	x
4	700	1.3	2.2Mar16	x
			4.2Mar16	
			6.22Feb16	
5	700	12	4.2Mar16	x
			1.22Feb16	
			3.14Mar16	
6	600	1.3	1.22Feb16	x
			4.2Mar16	
			6.22Feb16	

Table 3.12: Age hardening heat treatment parameters and samples (cont'd)

Mount #	Age T (^{o}C)	Age t (hrs)	Parent Sample	CW?
7	800	1.3	3.2Mar16	
			3.14Mar16	
8	500	12	4.22Feb16	
			3.2Mar16	
			5.14Mar16	x
9	600	4	2.2Mar16	
			5.14Mar16	
			2.2Mar16	x
10	800	12	4.2Mar16	x
			2.2Mar16	x
11	500	4	4.22Mar16	
			3.2Mar16	
			4.2Mar16	x
12	400	12	4.22Feb16	
			4.22bFeb16	
			5.14Mar16	x
13	400	4	4.22Feb16	
			4.22Feb16	
			5.14Mar16	X
18	800	12	2.2Mar16	
			5.14Mar16	
19	800	12	3.2Mar16	
			4.22Feb16	
24	400	12	1.14Mar16	
			1.14Mar16	
			1.14Mar16	
26	400	24	3.2Mar16	
			4.22Feb16	
			3.14Mar16	x
27	300	24	3.2Mar16	
			4.22Feb16	
			3.14Mar16	x
28	500	18	3.2Mar16	
			4.22Feb16	

3.5 Electron Microscopy Characterization

A Rapid Access Proposal was submitted to PNNL's user facility Environmental Molecular Sciences Laboratory (EMSL) for use of their electron microscopy instruments. Precipitation alloyed samples were further analyzed at EMSL.

3.5.1 Scanning Electron Microscopy

Cross-sectionally mounted precipitation hardened samples were examined on the EMSL Quanta 3D FEG SEM with a working distance of 10 mm at 20.00 kV using the high-contrast backscatter (vCD) detector. Point and Analyze spectra in a line away from the Cr strip were examined to determine Cr diffusion distance and concentration.

3.5.2 Focused Ion Beam Sample Preparation

Six HT samples were selected for Transmission Electron Microscopy (TEM) analysis, including one CW and non-CW sample for the same T and t.

Lift-out of TEM samples was performed on an FEI Helios Field Emission Focused Ion Beam (FIB) - SEM. Regions bisecting the Cr ribbon and extending out into the Cu-Cr alloyed region on cross-sectionally mounted and polished samples were selected for lift-out. The process, shown in Fig. 3.15, is as follows:

1. An area 5 um x 30 um was selected to lift-out for TEM examination

2. A bar of Pt 5 um x 10 um was deposited with the ion-beam and used to find eucentric height

3. C was deposited over the entire selected area

4. The area on either side of the C bar was trenched out using a gallium ion-beam

5. The TEM sample was welded to an atom probe and removed from the mounted sample

6. The sample was welded onto a Mo TEM grid and the atom probe was removed

7. The sample was thinned to ~100 nm thickness
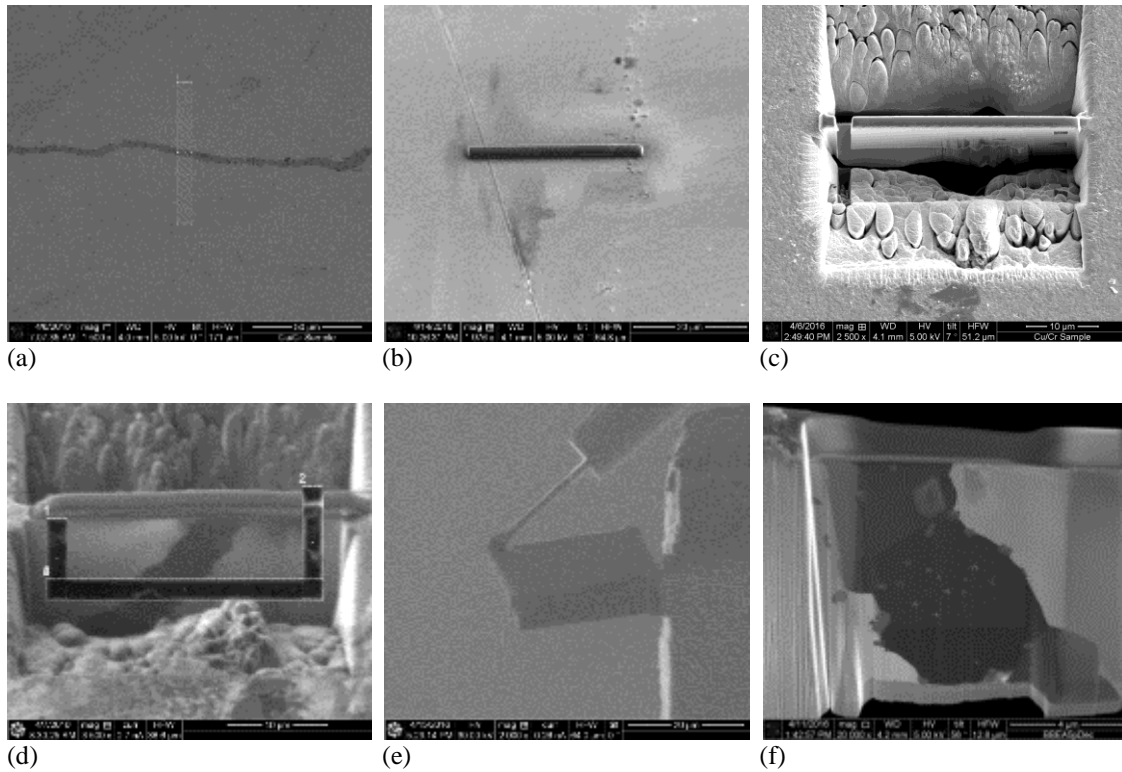
Figure 3.15: FIB sample prep for TEM (a) TEM sample area selection (b) ion-beam Pt and C deposition (c) ion-beam sample trenching (d) separating sample from bulk (e) sample attached to atom probe and TEM grid (f) thinned sample

3.5.3 Transmission Electron Microscopy

TEM examination of precipitation hardened lifted-out samples was completed on a FEI Titan 80-300 TEM operated at 300 kV with CEOS GmbH double-hexapole aberration corrector. All images were recorded on the High Angle Dark Field detector with a detection angle 1 to 3 times higher than the convergence angle.

Table 3.13 shows prepared TEM sample name and HT. The first sample examined on the TEM was M8 (4.22Feb16) age hardened at 500 ^{o}C for 12 hrs. The voltage during lift-out had been set too high during grid-welding. Fig. 3.16 shows holes burnt through the sample. There was not enough area left in the sample to examine, so it was determined to re-FIB the sample from another area of the mount.

Table 3.13: TEM examined samples

Sample	Age T (^{o}C)	Age t (hrs)	Parent Sample	CW?
M1	800	4	5.14Mar16	
M2	600	12	4.22Feb16	
M8	500	12	4.22Feb16	
M9	600	4	5.14Mar16	
			2.2Mar16	x
M12	400	12	4.22bFeb16	
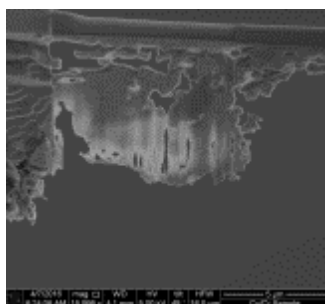
Figure 3.16: High current electron beam dissolved sample

Sample M1 (5.14Mar16) age hardened at 800 ^{o}C for 4 hrs was briefly examined in the TEM and sent back for further FIB thinning. Sample M9CW (5.14Mar16) age hardened at 600 ^{o}C for 4 hrs after CW was examined next on the TEM. Feature spectra and background spectra were measured. Selected area diffraction (SAD) diffraction patterns of the matrix and a large Cr precipitate were acquired.

Samples M8 and M1 which had been re-FIBed were again analyzed on the TEM. Sample M8 broke during re-thinning leaving approximately half for examination. Samples M9 (5.14Mar) age hardened at 600 ^{o}C for 4 hrs and M2 (4.22Feb) age hardened at 600 ^{o}C for 12 hrs were also examined and feature spectra peaks were recorded. In this last sample diffraction contrast was suppressed in an off-axis condition different features emerged. Their spectra and neighboring background spectra were acquired. Samples M9, M8, and M1 were re-examined mimicking the suppressed diffraction contrast conditions of M2. SAD patterns were imaged on a large precipitate and its adjacent matrix in M8. M9CW was not re-examined. Final sample M12 (4.22bFeb) age hardened at 400 ^{o}C for 12 hrs was analyzed on the TEM under the new contrast conditions.

3.6 Cu-Cr Physical Characterization

Alloyed Cu-Cr and parent electroplated Cu-Cr physical characterization
techniques include hardness and grain size.

3.6.1 Vickers Hardness

Vickers micro-hardness was indented with a 200 gf load on cross-sectionally
mounted precipitation hardened, solution treated, and non-HT parent samples at varying
distances from the Cu-Cr interface as shown in Fig. 3.17. Indents were micrographed
and Fig. 3.17b shows measurement of distance of indent from original Cu-Cr interface on
micrographs.

(a)   (b)
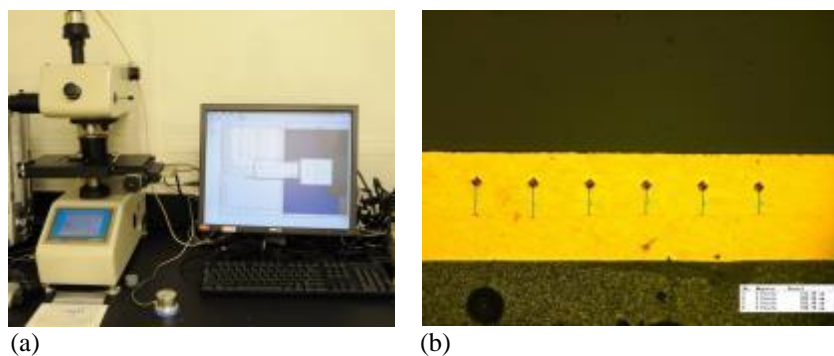
Figure 3.17: Sample indentation (a) hardness indenter (b) hardness indent distance measurement

3.6.2 Grain Size Determination

Indented samples were etched for grain boundaries with one or both in sequence
of the following etchants:

1.   1:1:0.3 $NH_4OH:H_2O:H_2O_2$

2.   1:5:14 $Fe(NO_3)_3:HCl:H_2O$.

Both dark field and bright field illumination as shown in Fig. 3.18 were used to reveal

GBs, as dictated by sample. Micrographs of etched samples were imaged. Grain size

was determined using the Heyn Intercept method. A line was drawn on the micrographs

perpendicular to the Cu-Cr interface at varying distances. The number of boundaries

crossed was enumerated.

(a)   (b)
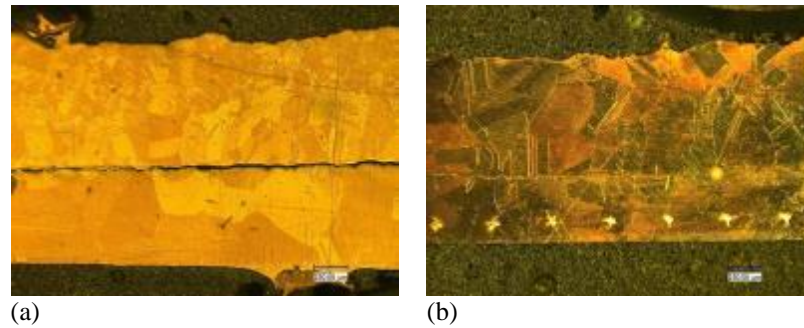
Figure 3.18: Cross-sectionally mounted and etched Cu-Cr samples (a) bright field illumination (b) dark field illumination

3.7 Purity Assay

Electrorefined Cr radiopurity was characterized using ICP-MS assay techniques.

3.7.1 Sample Screening

Concentration of U and Th was determined using several preparation methods on

an ICP-MS. Samples were screened first, in which concentration limits establishing

general magnitude of purity were found. For initial screening the samples were diluted to

metal ion concentrations of 100 ppb in a 2 % HNO_3 matrix. Density was measured by

weighing 100 ul of each sample solution. The dilute solution was aspirated into the ICP-

MS. All ICP-MS sample preparation steps involved optima grade acids, DI water,

implements and vials validated as having U, Th counts under 10 on the ICP-MS, and

leached plastics. The following samples shown in Fig. 3.19 were prepared for screening

with the ICP-MS:

1. Source Cr:
    a. Fisher Scientific 99 % purity $Cr(VI)O_3$ anhydrous powder with contents
       listed in Table 3.14, used as Cr-ion addition source in the majority of
       electrochemical experiments and plating runs
    b. Titan International aluminothermic 99.95% purity Cr chips, used as anode
       material and Cr-ion addition source in several experiments and plating
       runs
    c. Vacuum induction melted (VIM) Cr nugget sourced from Cr chips shown
       in Fig. 3.19a
2. Electroplated Cr on rolled Cu cathodes of unknown purity shown in Fig. 3.19b

a. Two samples plated from the first run of a fresh electrolyte

b. Two samples plated from the subsequent run with the same electrolyte

3. Electrolyte samples corresponding to each of the four plated samples

4. Electroformed Cu-Cr (EFCu-Cr) layered samples from a single mandrel shown in
   Fig. 3.19c

a. One sample without heat treatment

b. One sample heat treated on SS mandrel

c. One sample heat treated without SS mandrel

(a)   (b)   (c)
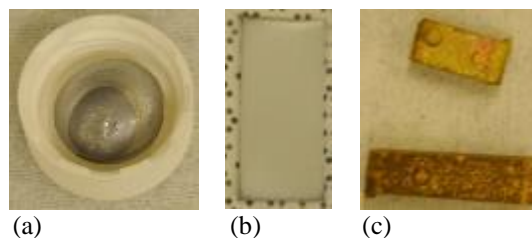
Figure 3.19: ICP-MS for purity assay Cr samples (a) VIM Cr nugget (b) electrorefined Cr deposited onto rolled Cu (c) alloyed Cu-Cr

Table 3.14: CrO_3 anhydrous powder Certificate of Analysis concentrations

Content	Concentration (lot 1)	Concentration (lot 2)
CrO_3	99.8%	99.8%
Cr	51.9%	51.9%
Insolubles	23 ppm	38 ppm
Sulfate	47 ppm	100 ppm
Sodium	925 ppm	862 ppm
Chloride	23 ppm	40 ppm
Fluoride	2 ppm	2 ppm
Iron	4 ppm	9 ppm

$Cr(VI)O_3$ powder was added to a 5 ml Savillex vial in the amount of 0.03568 g.

A dilute solution was prepared by pipetting 3 ml 2% HNO_3 into the vial. The brightly

colored sample was further diluted by adding 250 ul of the solution to 4.75 ml 2 %

HNO_3. The final solution included an addition of 50 ul radioisotope tracer containing 4

ppt ^{229}Th and ^{233}U.

The VIM Cr nugget and the Cr chips were sonicated in individual vials in a 1 %

Micro90 solution. The Cr nugget was etched in 50 % HCl. Etching dissolved 5.17g

(94.5%) of the nugget. Cr chips were rinsed in 6 M HNO_3 for 24 hrs. Both Cr sources

were rinsed with DI water and placed into vials. The minimum volume of acid for

dissolution was calculated using stoichiometry. The nugget and chips were dissolved

with additions of 8 ml and 4.5 ml 50 % HCl, respectively. Vials were sonicated to assist

in digestion. A thick black sludge resulted from both sources, and they were deemed

unsuitable for aspirating into the ICP-MS using the screening method.

The diluted CrO_3-baring solution was assayed on the tuned Agilent 8800 (S

configuration) ICP-MS following 20 samples for a different project, tracer, and 2 %

HNO_3 solutions. Fig. 3.20 shows the ICP plasma cone, which vaporizes aspirated

samples. Micrographs of the cone before (Fig. 3.20b) and after (Fig. 3.20c) assaying Cr

screening samples show it is coated by the Cr.

(a)   (b)   (c)
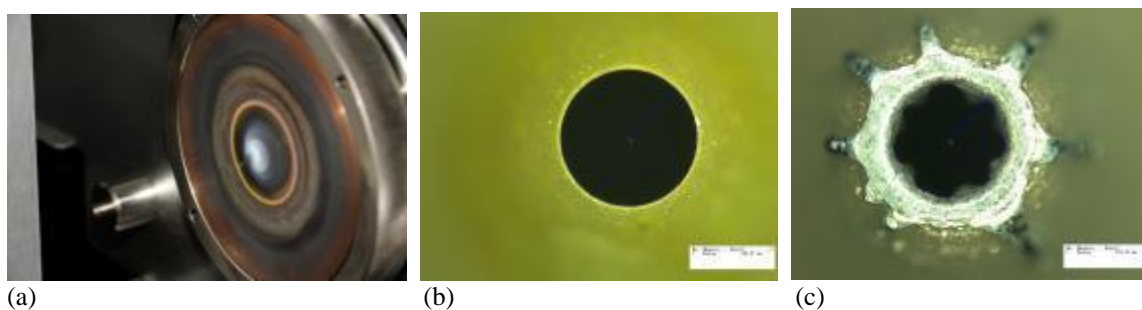
Figure 3.20: (a) ICP-MS plasma cone (b) plasma cone before running CrO_3 screening sample (c) cone after running Cr sample

3.7.2 Initial Column Separations

Two Cr plating baths were set-up, the deposits from which were prepared for assay. In the first Cr run, baths were set with fresh electrolyte in 100 ml HNO_3-rinsed vials. PbO_2 anodes were sonicated in a 10 % H_2SO_4 solution before being rinsed with DI water and set in Cr baths. Rolled Cu cathodes 0.47 mm thick were cut to 15.71 mm wide and rinsed with DI water before setting. Baths were operated for 24 hrs at 0.03 A/cm^2 galvanic control. Post-run electrolyte samples were taken. A successive run was set. For the second run new cathodes were set in each bath, using the same electrolyte and anodes. The same plating parameters were used and electrolyte samples were again set aside.

Strips of Cr on rolled Cu were cut from each of the four plated samples. These along with EFCu-Cr samples were etched briefly in 50 % HCl as shown in Fig. 3.21. They were placed in individual Savilex vials and 4.5 ml 50 % HCl was added to dissolve the Cr. Upon later examination it was noticed that some of the Cu, shown in Fig. 3.22, had partially dissolved in the HCl. Because of uncertain dissolved Cu contamination contribution, the four rolled samples were discarded.

The remaining Cu in EFCu-Cr samples was completely dissolved using 8M HNO_3 additions. Fig. 3.23 shows Cr oxides which remained in vials of heat treated EFCu-Cr samples post-dissolution. They were sonicated, eventually dissolving entirely the sample HT without SS.
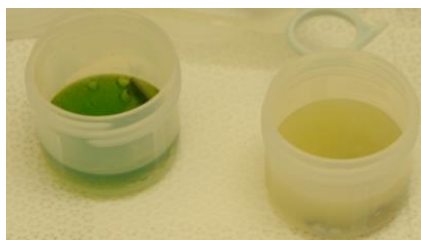
Figure 3.21: Cr assay sample etching
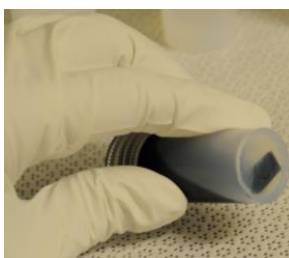
Figure 3.22: Partially dissolved rolled Cu strip
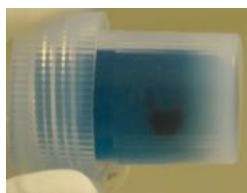
Figure 3.23: Oxides from EFCu-Cr sample

New strips of Cr on rolled Cu were cut from the same parent samples, placed in vials, and prepared as shown in Fig. 3.24. Fig. 3.24a shows vials with 5.5 to 7 ml 8 M HNO_3 which was added to dissolve the Cu cathodes. Dissolved Cu solution was drained while plated Cr films remained in vials. Samples in vials were rinsed six times with DI water, then left to dry in a laminar flow hood as shown in Fig. 3.24b. Fig. 3.24c shows samples after adding 50 ml tracer and 6 ml 50 % HCl to dissolve the Cr. Three process blanks (PB) were also prepared in 5 ml vials with 50 ul tracer and 5 ml 50 % HCl.

Cr on rolled Cu, EFCu-Cr, and PBs were boiled down simultaneously on a hot plate 7 times as shown in Fig. 3.24d, adding 1 ml of 8 M HNO_3 after each boil-down. After final boil-down 4 ml 8 M HNO_3 was added to each sample.

(a)   (b)

(c)   (d)
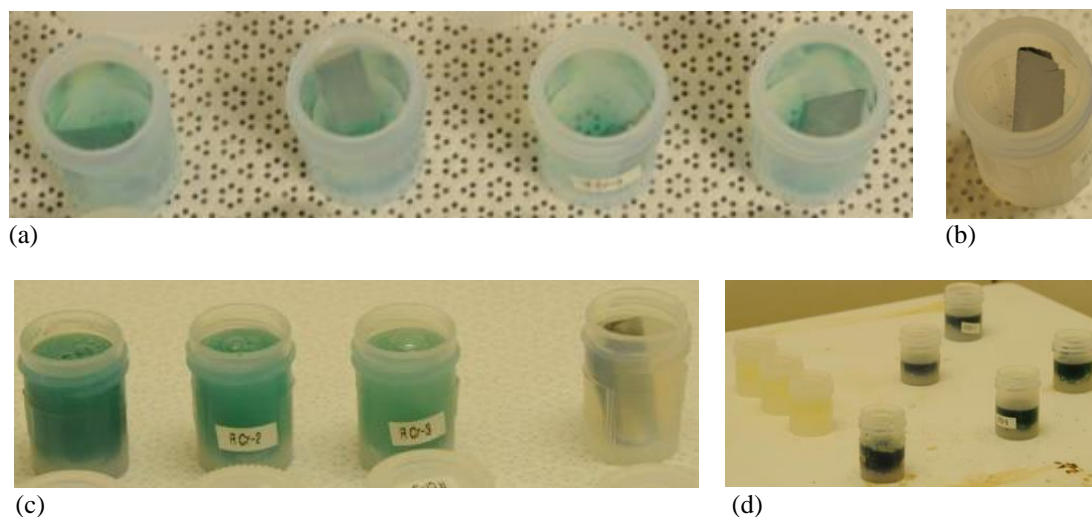
Figure 3.24: Cr on rolled Cu assay preparation (a) Cu cathode HNO_3 dissolution (b) remaining Cr (c) Cr HCl dissolution (d) hot plate boil-down

Environmental Express R1040 2.5 ml columns with frit were prepared with cleaned AG 1-X4 anion exchange resin and conditioned with 2 ml 8 M HNO_3. Samples were processed in the columns as shown in Fig. 3.25. Individual validated pipets were used to slowly add each prepared sample in 8 M HNO_3 matrix to ion-exchange columns. Remaining metal ions were washed from columns using 600 ul 8 M HNO_3. U and Th were eluted from the columns into vials using 1.8 ml 2 % HNO_3. Samples were assayed on the tuned Agilent 7700 (X configuration) ICP-MS following tracer and 2 % HNO_3 solutions.

(a)   (b)   (c)
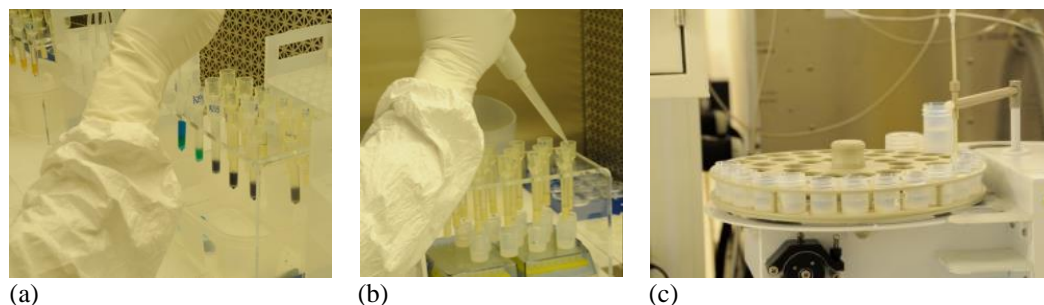
Figure 3.25: (a) Samples pipetted into anion exchange columns (b) samples eluted from columns (c) eluted sample aspiration into the ICP-MS

3.7.3 Final Column Separations

New plated Cr samples shown in Fig. 3.26 were prepared. High purity electroformed Cu foil <0.10 mm thick was used as cathode material. Five Cr samples were plated from fresh electrolyte in HNO_3-rinsed 30 ml vials onto 1.27 cm wide EFCu foil cathodes. PbO_2 anodes were sonicated in a 10 % H_2SO_4 solution before being rinsed with DI water and set in Cr baths. EFCu foil was rinsed in a dilute sulfuric acid solution to remove oxide film followed by ethanol to remove ink from cutting position marks. Foil was taped off with PTFE tape to a surface area of 254 mm^2, rinsed with DI water, and dried with N_2 before setting into baths. Baths were driven for 10 sec at 0.05 A/cm^2 then reduced to 20 hrs at 0.02 A/cm^2 galvanic control.

Figure 3.26: Cr on EFCu foil cathode

Electrolyte was taken from each bath post-run and placed in individual vials. Added to the 3 ml samples was 50 ul tracer. Three PBs were created with 50 ul tracer and 3 ml 8 M HNO_3. Previously prepared VIM and Chip source Cr samples has 50 ul tracer additions. Electrolyte, PB, and source samples were boiled down on the hot plate.

The former two sets were boiled down once followed by a 4 ml 8 M HNO_3 addition. The latter was boiled down 5 times followed by a 4 ml 8 M HNO_3 addition.

Plated Cr cathodes were placed in vials with 4 ml 8 M HNO_3. The resulting dissolved Cu solution was drained and vials were rinsed once with 6 M HNO_3 and six times with DI water. Sample number four fell apart during rinsing and was lost. Remaining samples shown in Fig. 3.27 were left to dry in a laminar flow hood. The Cr was dissolved by adding 5 ml 50 % HCl following 50 ml tracer additions. Cu was observed in each sample vial after Cr dissolution and 1 ml 8 M HNO_3 was added. Three PBs were prepared with 50 ul tracer and 5 ml 50 % HCl.

(a)   (b)   (c)
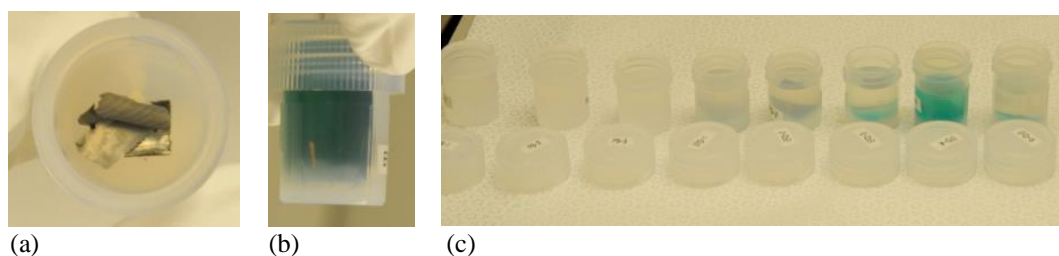
Figure 3.27: Cr on EFCu foil ICP preparation (a) post-Cu dissolution (b) remaining Cu piece (c) process blanks and dissolving Cr

Plated Cr samples, their PBs, and source Cr samples were boiled down 5 times. A total of 6 ml 8 M HNO_3 was added to the former two sets, and 9 ml to the latter. Plated Cr sample number two spilled and was lost during boil-down.

All prepared samples were pipetted through anion-exchange columns. Cr chips, electrolytes, CrO_3, and VIM Cr were not successfully separated by the column method as shown in Fig. 3.28. The Chip Cr solution would not diffuse down through the resin-bed and the three electrolyte solutions ate the resin-bed. The majority of these samples were set aside for future analysis, and not entirely used on the columns. Metal ions from the CrO_3 would not clean from the resin, causing the colored eluted solution shown in Fig.

3.29. The VIM Cr solution resin bed also remained colored after cleaning, although the eluted solution appeared clear. These eluted solutions were set aside and not directly aspirated into the ICP-MS.

The three plated Cr on EFCu foil samples and their process blanks were assayed on the 7700 ICP-MS following tracer and 2 % HNO_3 solutions.

(a)　　　　　　　　　　　　　(b)　　　　　　　　　　　　　(c)
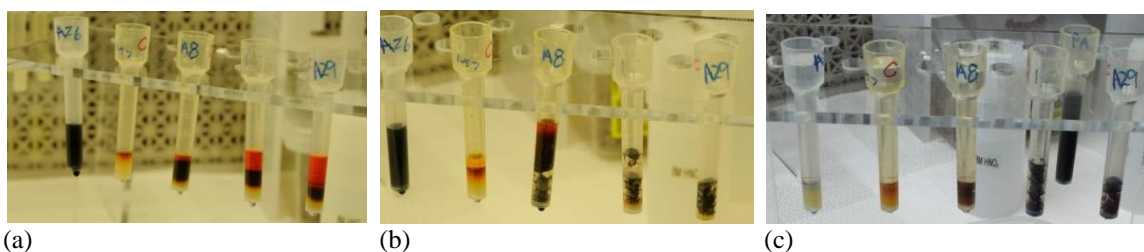
Figure 3.28: Source Cr columns. From left to right: VIM Cr nugget, CrO_3 powder, and post-run electrolyte samples for plated Cr samples 1, 3, and 5 (a) immediately after sample addition (b) within 5 minutes of addition (c) after eluting samples
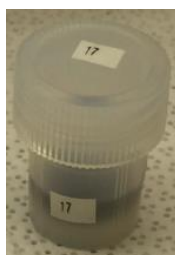
Figure 3.29: Eluted VIM Cr source sample

3.7.4 Diluted Solutions

VIM Cr, the colored column-processed CrO_3 solution, three H_2CrO_4 electrolytes, and their three PBs were diluted to ~1 ppb to safely aspirate into the ICP-MS. Serial dilutions were prepared using 10 ul of sample solution pipetted into vials with 990 ul of 2 % HNO_3. Of this diluted solution 30 ul was pipetted into new vials with 50 ul of radioisotope tracer and 3400 ul 2 % HNO_3.

The aforementioned diluted source Cr and electrolyte samples, as well as the

eluted chip Cr sample vials were assayed on the tuned 7700 ICP-MS following tracer and

2 % HNO_3 solutions.

4. EXPERIMENTAL RESULTS

4.1 Cu Experimental Results

Qualitative means taken to categorize Cu deposits include dendrite concentration and surface roughness. Quantitative deposit quality measurements made were current efficiency, hardness, and grain size. Presence of dendrite growth, average current density and current efficiency are given in Table 4.1 for the 11 Cu variable runs and 6 current step waveform runs. Current efficiency is calculated by Eq. 2.36; equation constant values are given in Table 4.2. Explanation of variables tested and images of representative resulting deposits for the 11 variable runs are shown in Table 4.3. Cu bath operation parameter values are chosen based upon deposit quality and listed in Table 4.4.

Images of Cu deposits relative to plating temperature for variable temperature tests are shown in Fig. 4.1. Current efficiency and current density for the six temperature runs are calculated and given in Table 4.5. These values for the three pulse-plating runs are calculated in Table 4.6. Current responses for voltage-controlled pulse-plating runs are shown in Fig. 4.2.

$CuSO_4$ electrolyte flow rates measured relative to stir rate (§ 3.1.4) are plotted in Fig. 4.3. Measurements of average surface roughness (§ 3.1.5) for cell-variable Runs 7 and 10 and pulse-plating frequency runs at 1 Hz and 10 Hz are given in Table 4.7.

Table 4.1: Cu cell variable investigation results

Run	Current Efficiency (%)	j (A/cm^2)	Deposits with Dendrites	$V_{measured}$ (V)
1 (5JUN15)	89.4	0.030	2	0.407
2 (9JUN15)	91.4	0.025	2	0.409
3 (12JUN15)	87.4	0.030	1	0.408
4 (16JUN15)	91.3	0.024	2	0.411
5 (18JUN15)	88.0	0.026	2	0.409
6 (22JUN15)	91.8	0.021	3	0.416
7 (24JUN15)	91.3	0.012	5	0.323
8 (27JUN15)	95.4	0.011	8	0.323
9 (29JUN15)	91.4	0.018	2	0.414
10 (1Jul15)	95.2	0.006	7	0.235
13(21Dec15)	93.3	0.020	0	0.323
20(14Mar16)	87.0	0.014	7	0.290
21(16Mar16)	94.7	0.014	4	0.333
20b(18Mar16)	100.1	0.012	0	0.305
21b(20Mar16)	100.6	0.011	0	0.295
8b(24Mar16)	100.7	0.012	0	0.353
9b(29Mar16)	100.8	0.013	2	0.374
25(22Sep16)	94.0	0.016	2	0.241

Table 4.2: Current Efficiency constants for the $CuSO_4$ and H_2CrO_4 systems

Element	A_{wt} (g/mol)	Density (g/cm^3)	Electrons n	Faraday F (C/mol)	Z (g/C)
Cu	63.55	8.93	2	96487	0.000329319
Cr	52	7.19	6		8.98221E-05

Table 4.3: Effect of varied cell operation parameters on Cu deposit quality and morphology

Run	Variable	Deposit
1	Starting Conditions	
2	Higher $CuSO_4$ Concentration	
3	One Side Sanded	
4	stir rate increased from 350 to 525 RPM	
5	stir rate increased to 700 RPM	
6	$CuSO_4$ Concentrations decreased (top = 1.15 g_{Cu}/L, bottom = 0.61 g_{Cu}/L)	
7	Voltage reduced from 0.44 V to 0.34 V	
8	280 grit mandrel prep	
9	Same as 6 with 22 grit mandrel prep	
10	Voltage reduced to 0.25 V	
25	Conductivity raised to 300 mS/cm	

Table 4.4: Selected Cu cell parameter values

Parameter	Selected Value
$CuSO_4$ Concentration	1.15 - 2.00 g_{Cu}/L
Stir Rate	525
Mandrel Prep	280 grit
Conductivity	Medium
Current Density	two-step: high j for 10 min, low j for remainder

(a)　　(b)　　(c)　　(d)　　(e)　　(f)
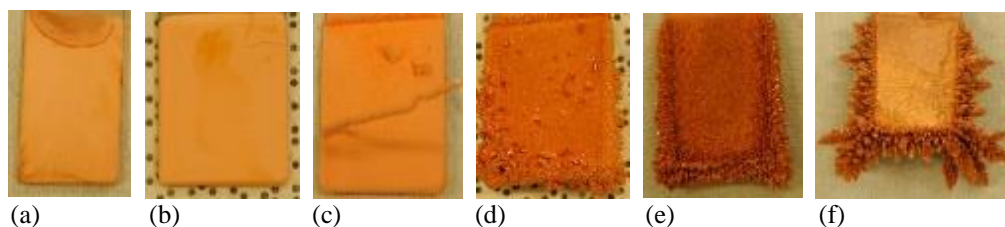
Figure 4.1:Cu deposited at temperatures (a) 3 ^{o}C (b) 12 ^{o}C (c) 22 ^{o}C (d) 36 ^{o}C (e) 52 ^{o}C (f) 65 ^{o}C

Table 4.5: Current density and current efficiency of Cu temperature investigative runs

Run	Bath	T (^{o}C)	j (A/cm^2)	Current Efficiency (%)
24	1	38.3	0.063	34.4
	2	51.6	0.054	64.0
25	3	37.1	0.081	63.9
	4	63.4	0.081	99.4
	1	22.8	0.017	94.0
	2	21.9	0.019	93.9
26	L1	12.5	0.0028	117.7
	L2	12.5	0.0038	77.4
	L3	12.5	0.0018	118.7
27	1	36.0	0.047	88.3
28	L1	3.0	0.00074	326.0
	L2	3.0	0.0030	64.6
	L3	3.0	0.00079	4.1
29	1	64.9	0.083	50.1

Table 4.6: Current density and current efficiency of Cu pulse-plating runs at various frequencies

Run	Bath	Freq. (Hz)	j (A/cm²)	Current Efficiency (%)
22	1	1	0.00618	69.64891354
	2		0.00462	91.13140043
	3		0.00470	82.26854387
23	1	10	0.00470	-
	2	1000	0.00548	21.01195746
	3	100	0.00689	24.2393995
24	1	10	0.000783	204.6050774
	2	100	0.00798	27.8172384
	3	1000	-	-

(a)

(b)

(c)

(d)
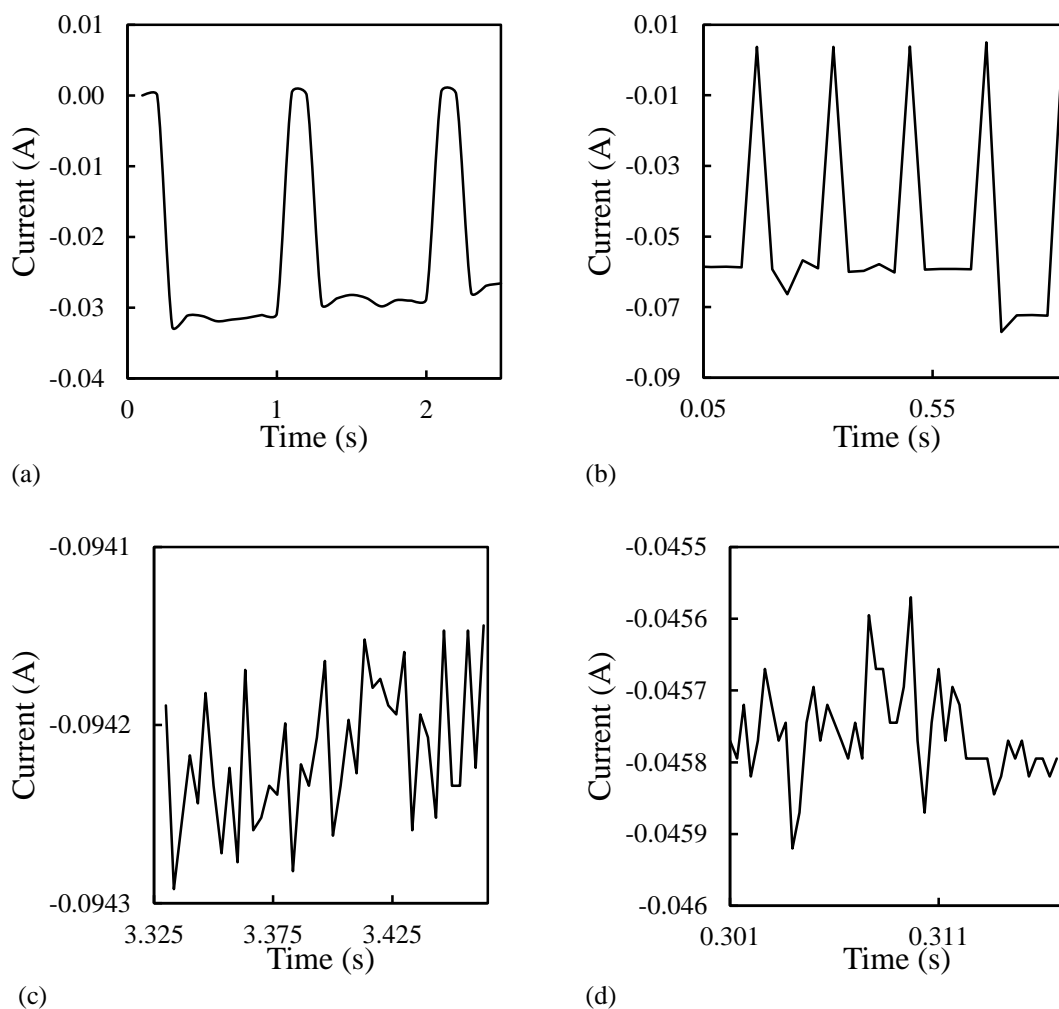
Figure 4.2: Current response of voltage-controlled Cu pulse-plating runs operated at (a) 1 Hz (b) 10 Hz (c) 100 Hz (d) 1000 Hz
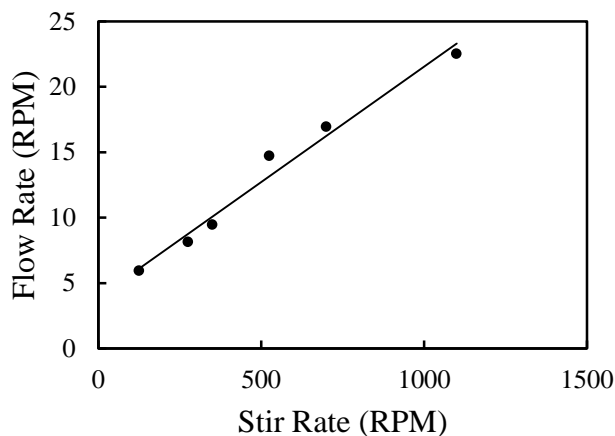
Figure 4.3: Flow rate in Cu plating baths corresponding to stir bar rotation rates

Table 4.7: Average surface roughness for selected parameter runs

Run	Variable	Avg. Roughness (um)
7	$j = 0.012$ A/cm^2	51.36
10	$j = 0.006$ A/cm^2	18.32
22	1 Hz	4.67
23	10 Hz	2.75

Vickers micro-hardness, current density and grain size for samples from Run 4, 7, 10, and pulse-plating Runs at 1, 10, 100, and 1000 Hz are given in Table 4.8. Micrographs of associated etched samples are shown in Fig. 4.4. Hall-Petch Plots (§ 2.2.4) are shown in Fig. 4.5. Relationship between hardness, grain size, current density, and deposition frequency is plotted in Fig. 4.6.

Levich plots from polarization curves measured with the RDE on CuSO$_4$ electrolytes are shown in Fig. 4.7. The diffusion coefficient calculated from the Levich equation (Eq. 2.22) is shown with equation constants in Table 4.9. Diffusion layer thickness relative to CuSO$_4$ concentration is calculated using the diffusion coefficient (Eq. 2.23). Kinematic viscosity for the molar range of CuSO$_4$ and H$_2$SO$_4$ in solution is given by Roy and Landolt[76].

Table 4.8: Average hardness, grain size, and current density of selected Cu-variable and pulse-plating runs

Run	Avg. Hardness (HV)	Avg. Grain Diameter L_3 (um)	ASTM G	Avg j (A/cm^2)
4 (16Jun)	165.53	-	-	0.024
7(24Jun)	151.42	182.87	1.6	0.012
10 (1Jul)	95.77	6.38	11.3	0.006
1Hz	87.98	2.02	14.6	0.005
10Hz	71.33	5.34	11.8	0.003
100Hz	73.15	6.92	11.1	0.007
1000Hz	89.94	27.27	7.1	0.005
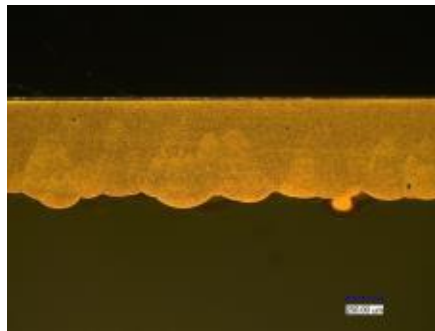
(a)
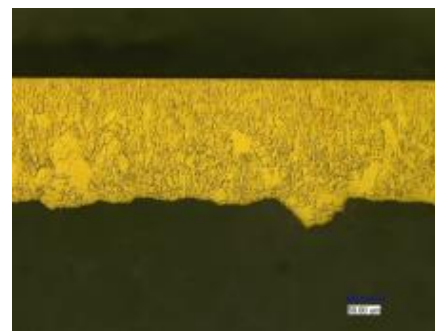
(b)
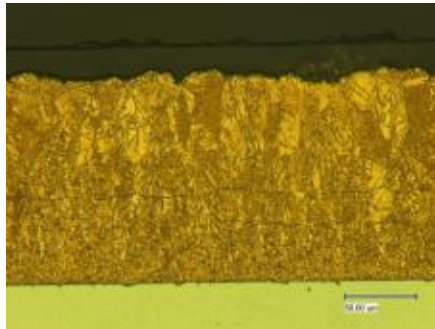
(c)
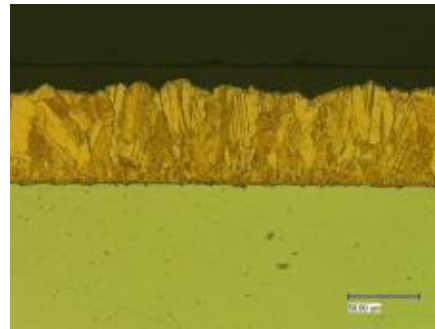
(d)
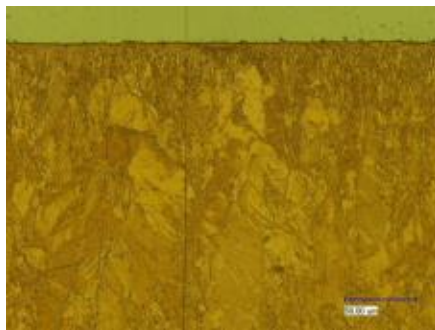
(e)
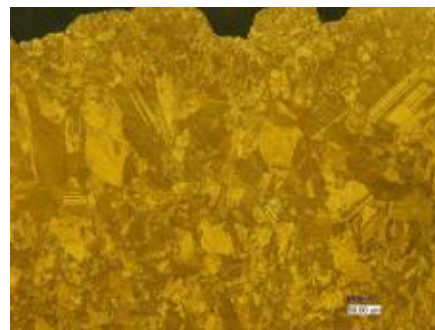
(f)

Figure 4.4: Micrographs of etched Cu deposits (a) Run 7 (b) Run 10 (c) 1 Hz (d) 10Hz (e) 100 Hz (f) 1000 Hz
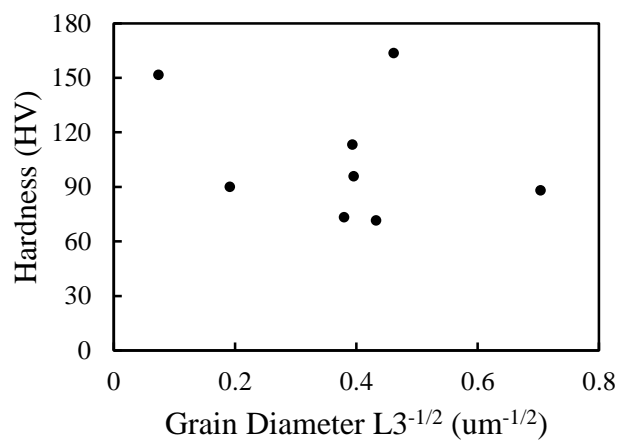
Figure 4.5: Electrodeposited Cu Hall-Petch Plot

(a)

(b)
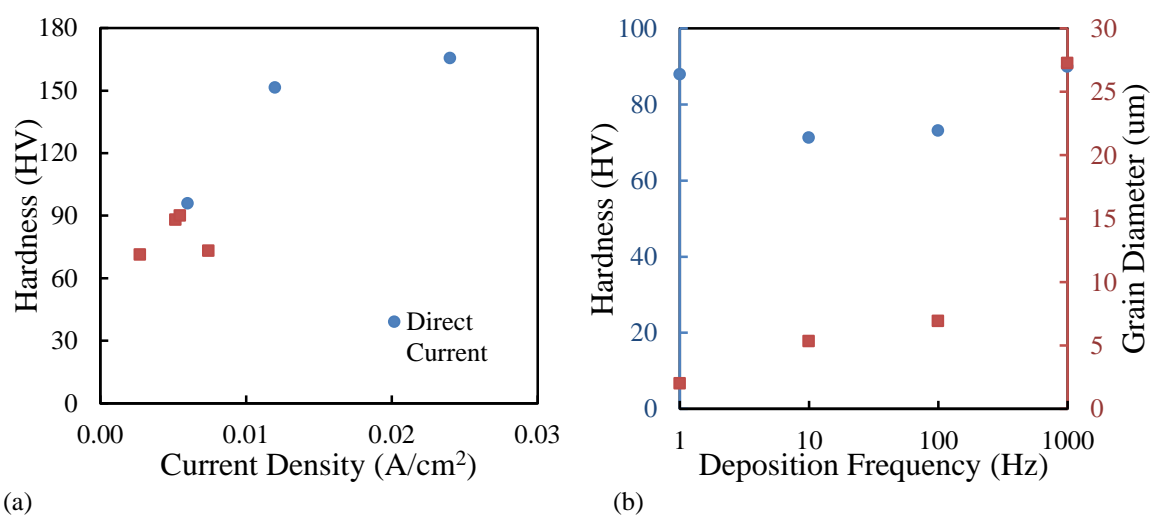
Figure 4.6: (a) Direct current and pulse-plated Cu hardness's with respect to plating current density (b) average hardness (blue) and grain size (red) for pulse-plated Cu

(a)

(b)

(c)
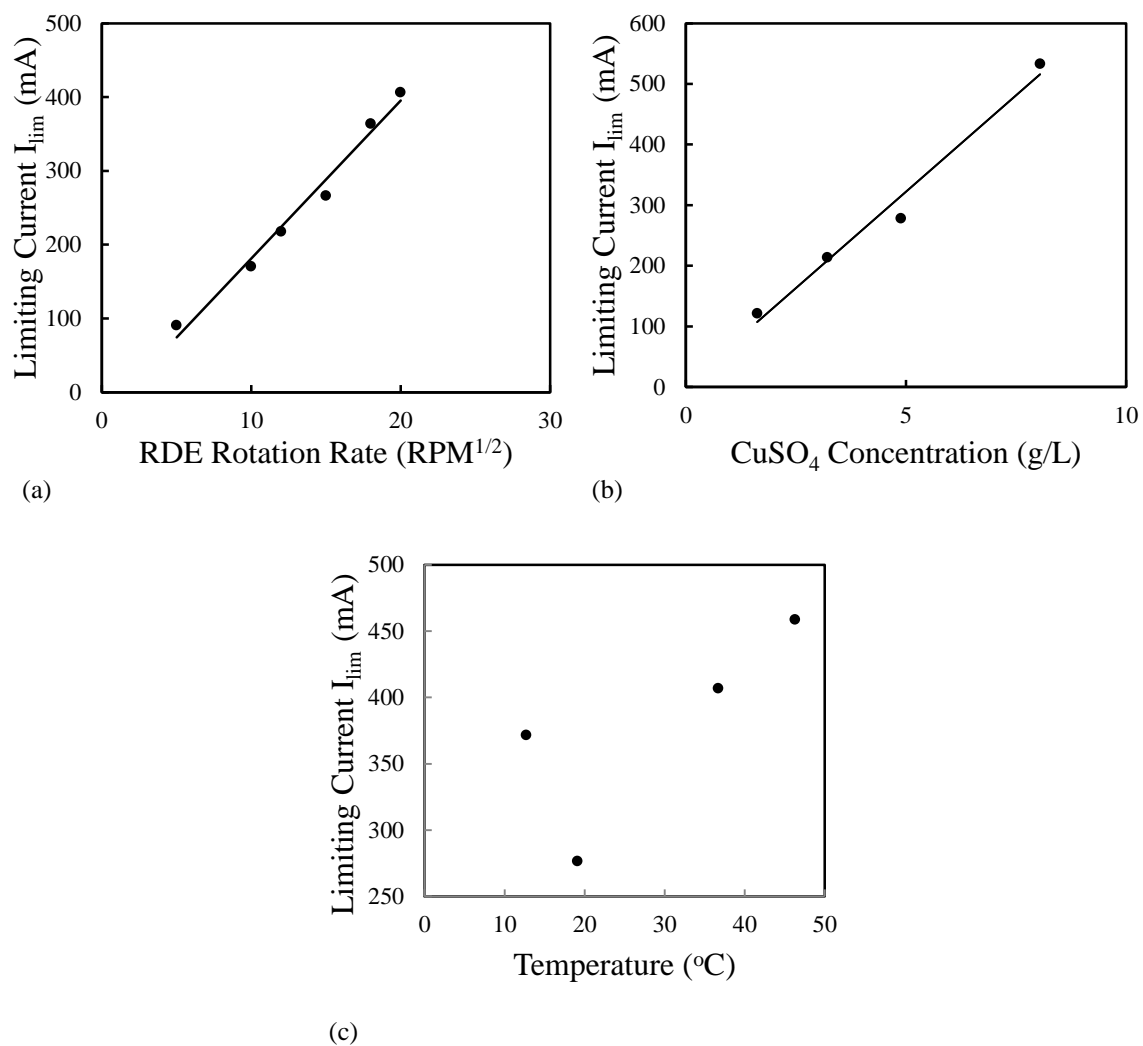
Figure 4.7: $CuSO_4$ RDE studies (a) Levich Plot (b) effect of $CuSO_4$ concentration on limiting current (c) effect of $CuSO_4$ electrolyte temperature on limiting current

Table 4.9: Levich Equation variables

Variable	Value	Units
z	2	electrons
F	96487	C/mol
A	1	cm^2
C_b	2.73E-05	mol/cm^3
D	0.0011694	cm^2/s
υ	0.011	cm^2/s
δ	$0.128\,\omega^{-1/2}$	-

Cu deposition peak relative to scan rate is plotted in Fig. 4.8. Plots of potential peak position and current peak magnitude (§ 3.1.6) are shown for concentration in Fig. 4.9, stir rate in Fig. 4.10, and temperature in Fig. 4.11.
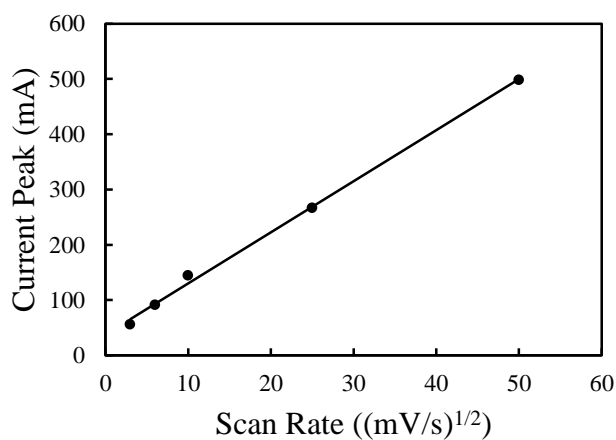
Figure 4.8: CuSO$_4$ current peak position relative to scan rate

(a)   (b)
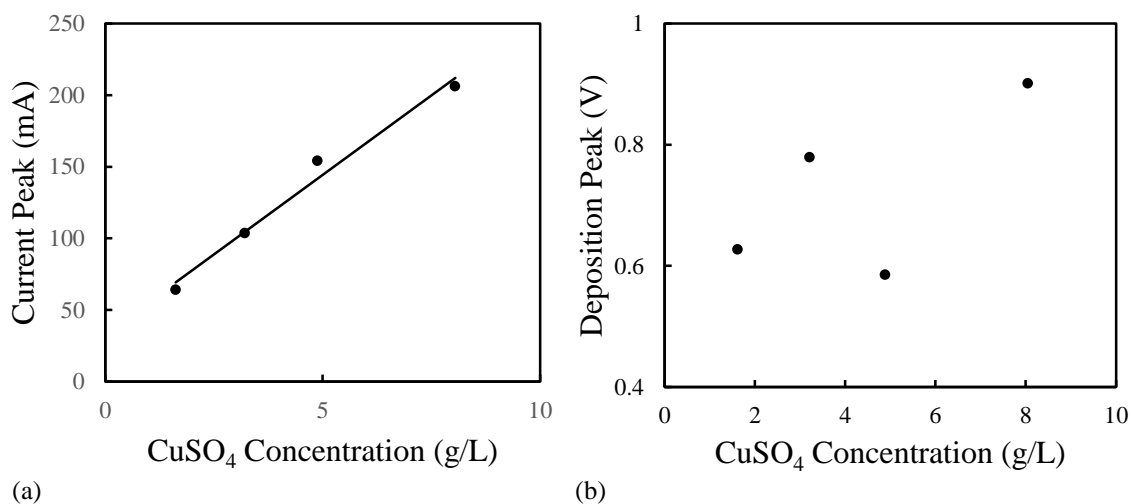
Figure 4.9: Effect of CuSO$_4$ Concentration on (a) current deposition peak (b) deposition peak potential
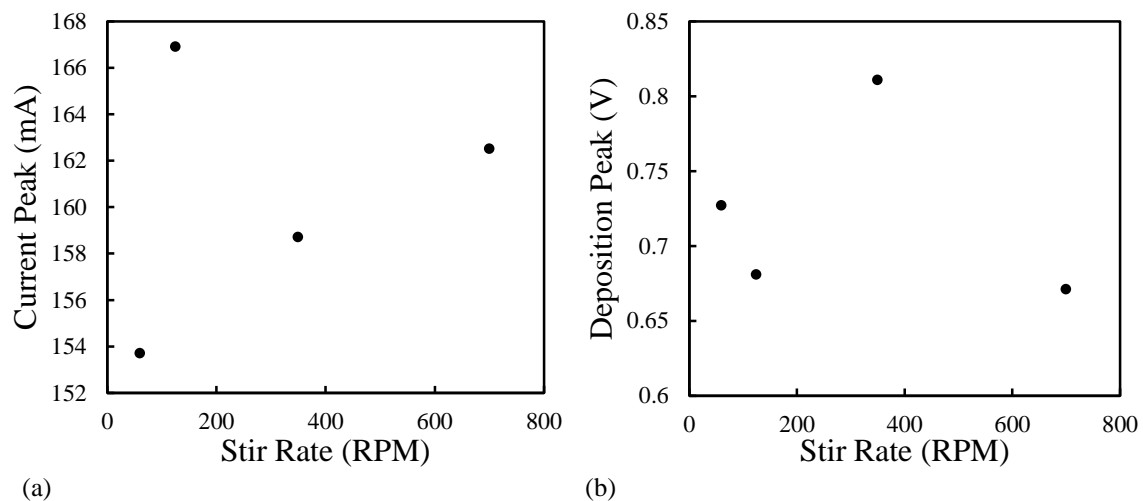
Figure 4.10: Effect of stir rate on (a) current deposition peak (b) deposition peak potential
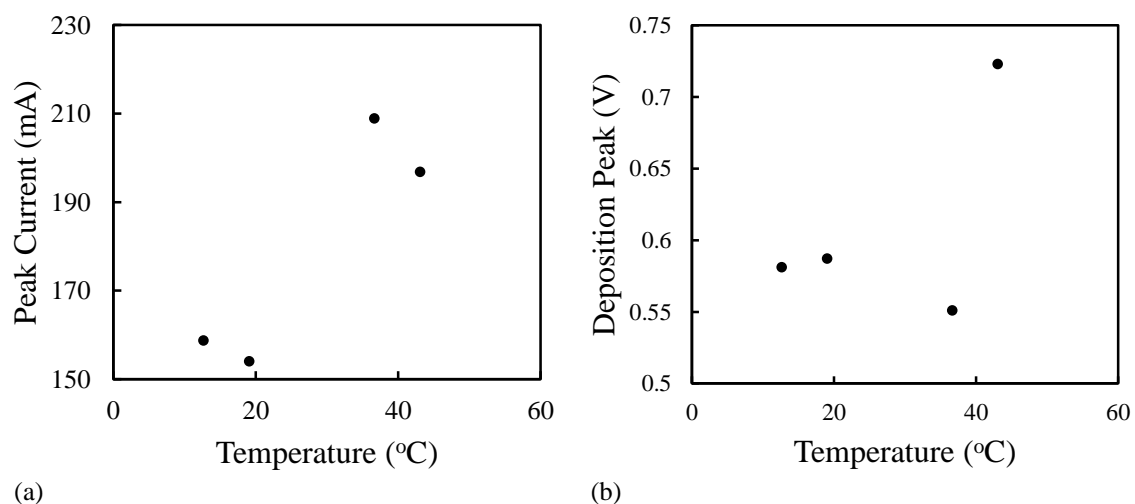
Figure 4.11: Effect of $CuSO_4$ electrolyte temperature on (a) current deposition peak and (b) deposition peak potential

The $CuSO_4$ Tafel plot is shown in Fig. 4.12. Constants for the Tafel equation (Eq. 2.18, .19) are calculated in Table 4.10. The Anson plot from chronocalorimetry slopes run at $V_0 = 0$ V, $V_1 = -0.6$ V and $V_2 = 0.11$ V is shown in Fig. 4.13. Integrated Cottrell Equation (Eq. 2.16) constants and values calculated from the Anson plot is listed in Table 4.11. Supporting electrolyte and charging current backgrounds have been subtracted from all plots with the exception of the Anson Plot.
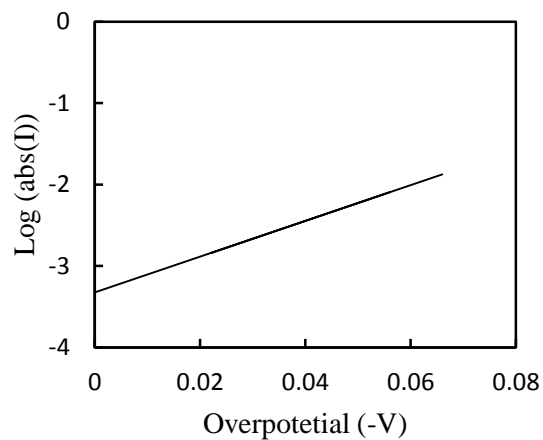
Figure 4.12: CuSO$_4$ Tafel Plot

Table 4.10: CuSO$_4$ Tafel constants

Slope b	Intercept a	i$_0$	α
-21.942	-3.3244	2.51E-03	0.0430951
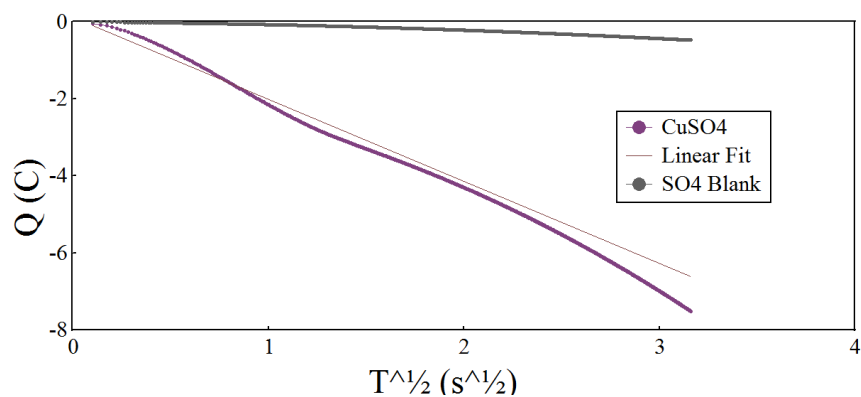
Figure 4.13: CuSO$_4$ Anson plot

Table 4.11: CuSO$_4$ integrated Cottrell values

Variable	Value	Unit
z	2	electrons
F	96487	c/mol
A	1	cm^2
C$_b$	2.73E-05	mol/cm^3
D$_M$	1.28E-01	cm^2/s

4.2 Cr Experimental Results

Qualitative means taken to categorize Cr deposits include finish categorization, extent of cracking, and extent of pitting. Quantitative deposit quality measurements made were current efficiency, hardness, and covering/throwing power.

Produced Cr deposit surface finishes were categorized as dark, bright, frosty, barely plated or a combination thereof. Table 4.12 shows finish resulting from various cell volumes and current densities of the 34 Cr on rolled Cu runs. Cr finish relative to current density is plotted in Fig. 4.14.

Table 4.12: Cr parameter runs' results

Run	Bath	Volume (ml)	Current density (A/cm^2)	Cr Finish
1	L5	28	0.021	frosty
	L6			frosty
	L1	135		barely
	L2			barely
	L4			dark
2	L5	28	0.021	bright
	L6			bright
	L1	135		none
	L2			none
	L4			bright
3	L5	28	0.021	bright
	L6			bright
	L1	135		none
	L2			none
	L4			bright
4	L5	28	0.021	frosty
	L6			frosty
	L1	135		frosty

Table 4.12: Cr parameter runs' results (cont'd)

Run	Bath	Volume (ml)	Current density (A/cm^2)	Cr Finish
4	L1	135	0.021	frosty
	L2			dark
	L4			dark
5	L5	28	0.021	bright
	L6			bright
	L1	135		bright
	L2			none
	L4			bright
6	L5	28	0.021	frosty/bright
	L6			frosty/bright
	L1	135		bright
	L2			bright
	L4			barely
7	L5	28	0.031	dark
	L6			dark
	L1	135		dark
	L2			dark
	L4			dark
8	L5	28	0.031	bright
	L6			bright
	L1	135		bright
	L2			bright
	L4			bright/frosty
9	L5	28	0.031	frosty
	L6			frosty
	L1	135		frosty
	L2			frosty
	L4			frosty
10	L5	28	0.01	barely
	L6			none
	L1	135		none
	L2			none
	L4			barely
11	L5	28	0.01	dark/bright
	L6			dark/bright
	L1	135		dark/bright
	L2			dark/bright
	L4			dark/bright

Table 4.12: Cr parameter runs' results (cont'd)

Run	Bath	Volume (ml)	Current density (A/cm²)	Cr Finish
12	L5	28	0.01	none
	L6			none
	L1	135		none
	L2			dark
	L4			none
13	L5	28	0.031 for 10sec followed by 0.01	dark
	L6			dark
	L1	135		bright
	L2			dark
	L4			dark
14	L5	28	0.01	barely
	L6			barely
	L1	135		barely
	L2		0.016	barely
	L4			none
15	L5	28	0.042	bright/frosty
	L6			bright/frosty
	L1	135		frosty
	L2			frosty
	L4			bright/frosty
16	L5	28	0.042	bright/frosty
	L6			frosty
	L1	135		frosty
	L2			bright/frosty
	L4			bright/frosty
17	L5	28	0.042	none
	L6			none
	L1	135		none
	L2			none
	L4			none
18	L5	28	0.042	bright
	L6			dark
20	L5	28	0.052	frosty
	L6			frosty
21	L5	28	0.052	bright/frosty
	L6			bright/frosty
	L1	135		bright/frosty
	L2			frosty
	L4			bright/frosty

Table 4.12: Cr parameter runs' results (cont'd)

Run	Bath	Volume (ml)	Current density (A/cm²)	Cr Finish
22	L5	28	0.063	frosty
	L6			frosty
	L1	135		frosty
	L2			frosty
	L4			frosty
23	L5	28	0.063	bright/frosty
	L6			bright/frosty
	L1	135		dark/bright
	L2			dark/bright
	L4			dark/bright
24	L5	28	0.073	bright/frosty
	L6			bright/frosty
	L1	135		frosty
	L2			frosty
	L4			bright/frosty
25	L5	28	0.031	bright
	L6			bright
	L1	135		bright
	L2			bright
	L4			bright
26	L7	28	0.031	bright
27	L5	28	0.03	dark
	L7			bright
	L1	135		dark
	L2			dark
	L4			dark
29	L5	28	0.087	frosty
	L1	135		bright
	L2			bright
	L4			bright
	O1	750	0.03	bright
	O2			bright
	O4			bright
30	L5	28	0.031	bright/frosty
	L1	135		bright/frosty
	L2			bright
	L4			frosty

Table 4.12: Cr parameter runs' results (cont'd)

Run	Bath	Volume (ml)	Current density (A/cm^2)	Cr Finish
30	O1	750	0.031	bright
	O2			bright
	O4			frosty
31	L5	28	0.031	frosty
	L1	135		frosty
	L2			bright/frosty
	L4			frosty
	O1	750		frosty
	O2			frosty
	O4			frosty
32	L5	28	0.031	bright
	L1	135		bright
	L2			frosty
	L4			bright
	O1	750		frosty
	O2			frosty
	O4			bright/frosty
33	L5	28	0.031	none
	L1	135		bright/frosty
	L2			bright
	L4			bright/frosty
	O1	750		bright
	O2			bright
	O4			none
34	L1	135	0.03	bright/frosty
	L2			bright
	L4			none
	O1	750		dark
	O2			bright
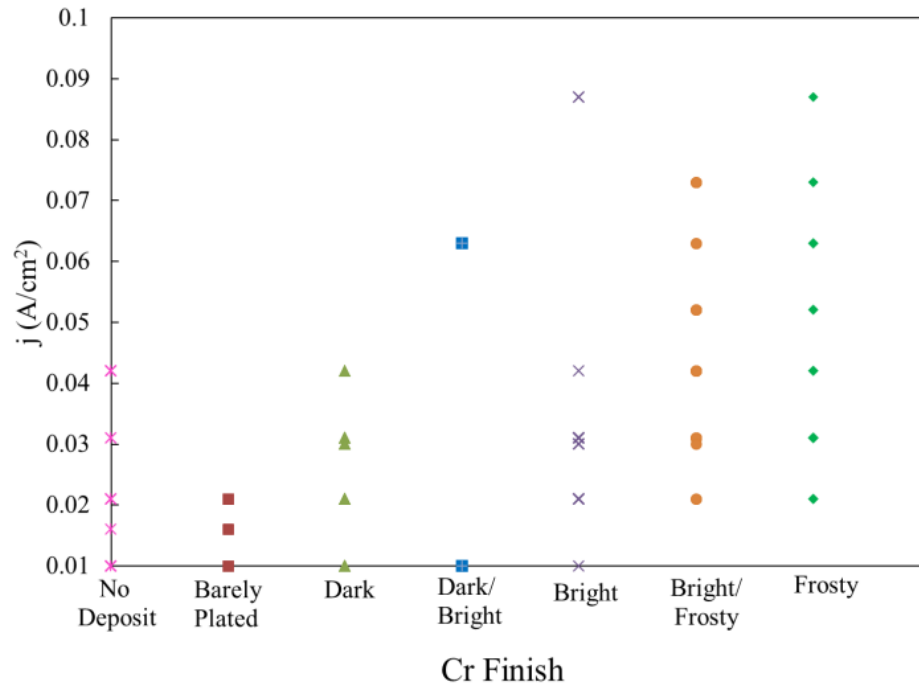
Figure 4.14: Cr surface finish relative to current density j

Measured Vickers hardness values for each Cr finish described in § 3.2 are given in Table 4.13. Micrographs of Cr finishes and hardness indents are shown in Figure 4.15.

Table 4.13: Average Vickers hardness of Cr finishes on rolled Cu

Finish	Avg. Hardness (HV)
not plated	73.96
Barely Plated	75.26
Dark	81.73
Bright	90.90
Frosty	74.93
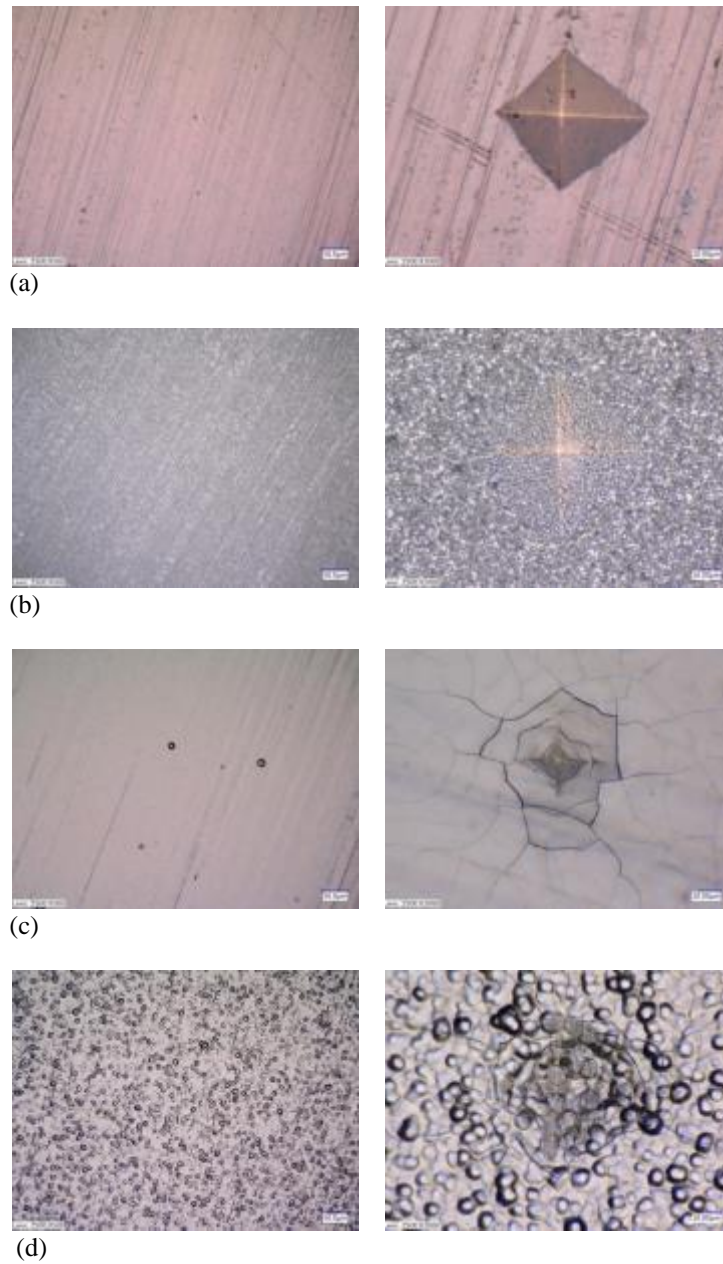
Figure 4.15: Micrographs of Cr finish surface and hardness indent (a) barely plated (b) dark/milky (c) bright (d) frosty

4.2.1 CrO$_3$ Concentration

CVs measured pre-plating for each of the four H$_2$CrO$_4$ variable concentration baths described in § 3.2.1 are shown in Fig. 4.16. Resulting Cr deposits are shown in Fig. 4.17.
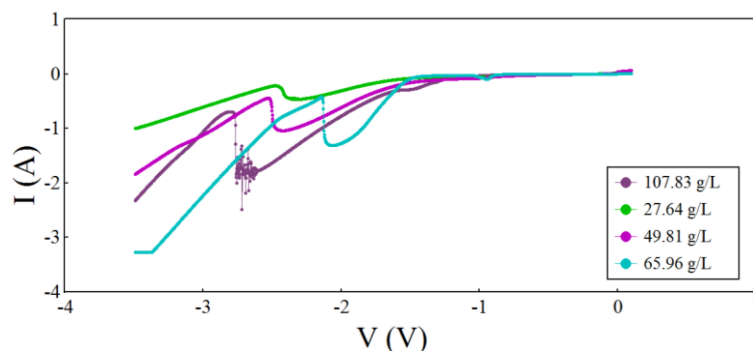
Figure 4.16: Cr concentration determination bath CVs

(a)

(b)

(c)

(d)
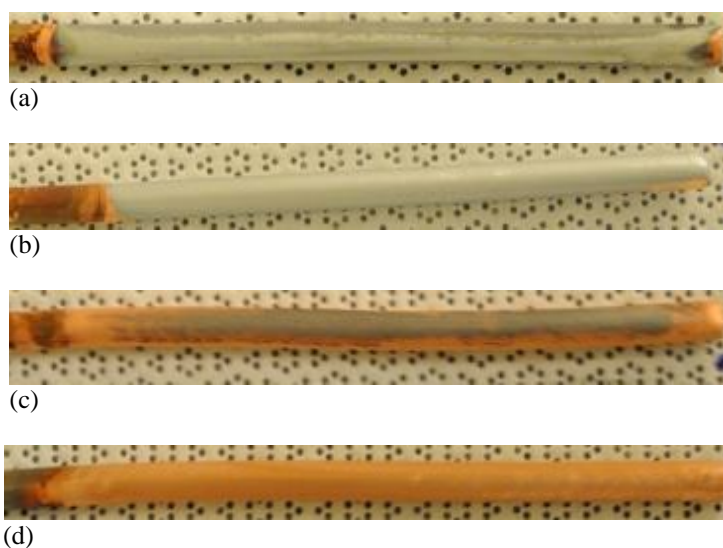
Figure 4.17: Cr deposited from H_2CrO_4 concentrations (a) 107.83 g_{Cr}/L (b) 65.96 g_{Cr}/L (c) 49.81 g_{Cr}/L (d) 27.64 g_{Cr}/L

4.2.2 Temperature

Hull cell rolled Cu cathodes plated with Cr at various electrolyte temperatures as described in § 3.2.3 are shown in Fig. 4.18. Minimum plating current density resulting from Hull cell test relative to temperature is plotted in Fig. 4.19.
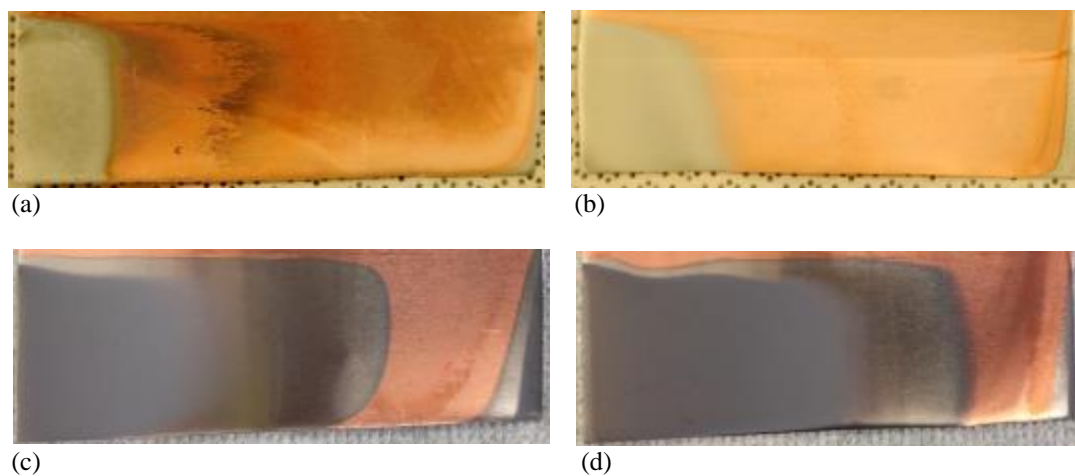
Figure 4.18: Hull cell Cr deposited at temperatures (a) 50.2 ^{o}C (b) 40.5 ^{o}C (c) 19.1 ^{o}C (d) 9.5 ^{o}C
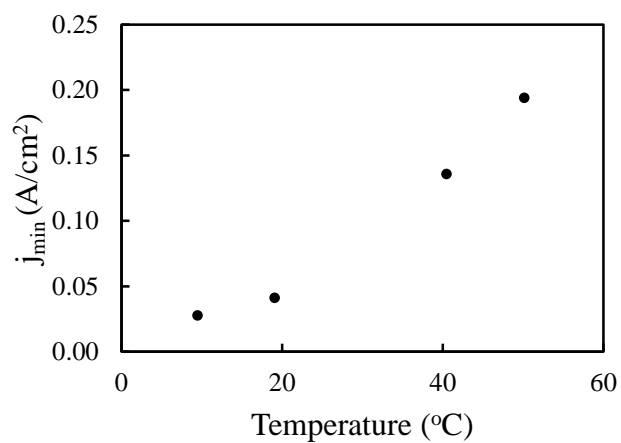
Figure 4.19: Minimum Cr reduction current density relative to temperature

4.2.3 Flow Rate

Flow rate investigation CVs described in § 3.2.4 are shown in Fig. 4.20. Flow rate measured relative to stir rate is plotted in Fig. 4.21.
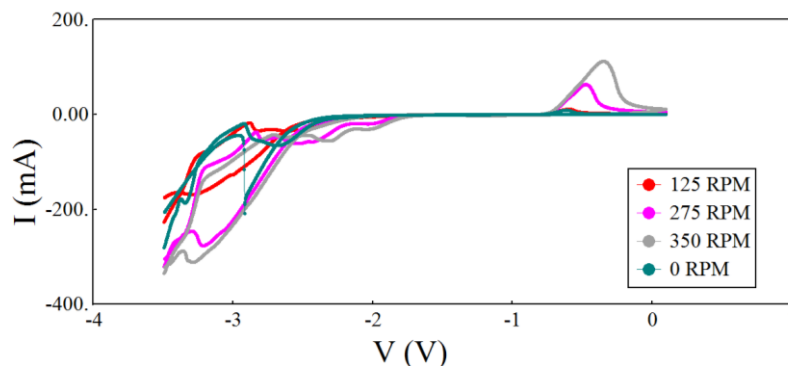
Figure 4.20: Varied H_2CrO_4 stir rate CVs
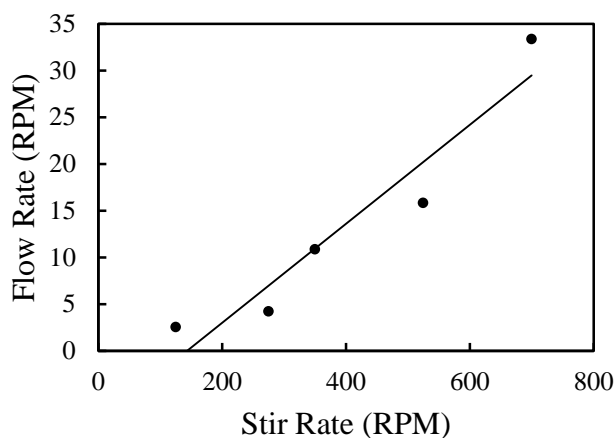
Figure 4.21: H_2CrO_4 flow rate corresponding to stir bar rotation rate

4.2.4 Electrode Considerations

Slopes from corrosion potential curves for PbO_2 anodes passivated according to procedures described in Table 3.7 are given in Table 4.14 (curves are shown in Appendix D). Anode B4 corrosion potential and CVs showing increasing charge transfer with each successive cycle are shown in Fig. 4.22.   Also shown is voltage response for B4 anode relative to other anodes used in Run 47.

Cr^{3+} partial oxidation investigations were run at constant current, while monitoring changes in voltage. Effect of parameters on extent of Cr^{3+} oxidation

described in § 3.2.5.2 is shown through cyclic voltammetry. Oxidation run voltage

responses with pre- and post-run CVs and are plotted in Fig. 4.23.

Table 4.14: Corrosion potential linear fit slope and correlation coefficient R^2

Anode	Slope (uV/s)	R^2
L3	-27.85	0.918
L4	-62.36	0.996
L3,2	-45.27	0.959
L4,2	43.52	0.881
A5	-10.91	0.980
A7	7.56	0.8058
L5	-64.38	0.9073
L6	-949.2	0.940
B2	38.22	0.923
B1	-103.8	0.976

(a)

(b)

(c)
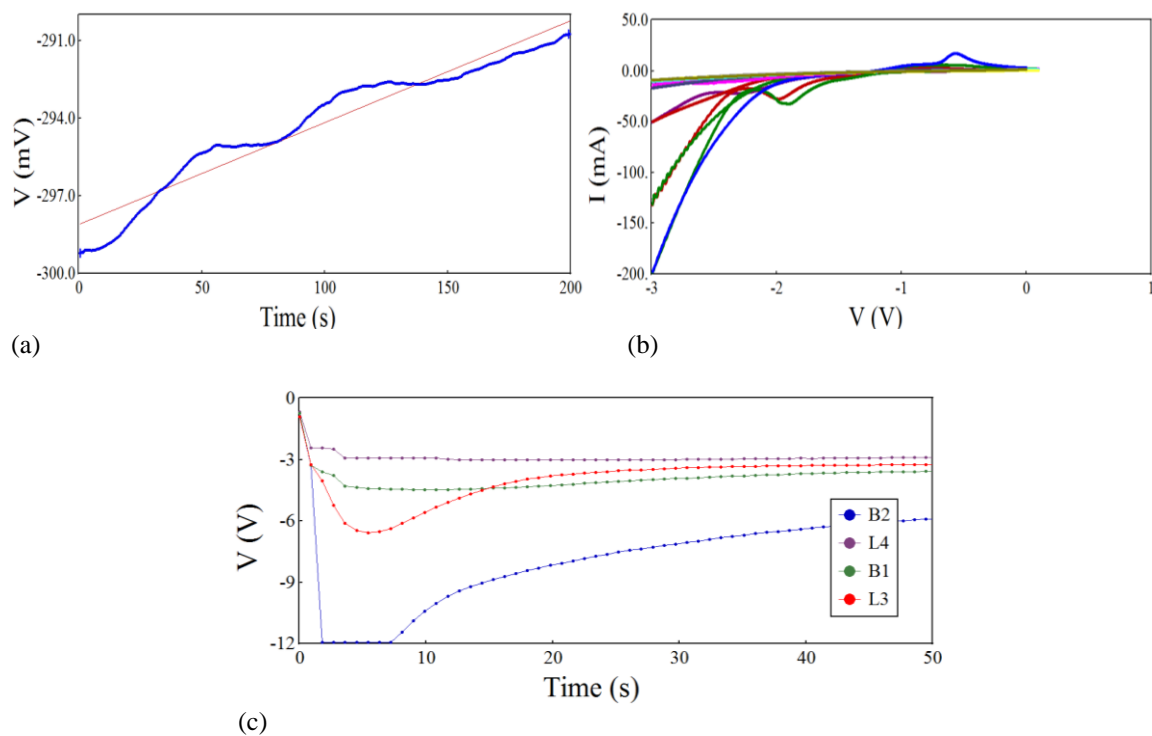
Figure 4.22: Passivated lead anode B2 (a) corrosion potential curve (b) successive CVs (c) Run 47 anode voltage responses

(a)

(b)

(c)
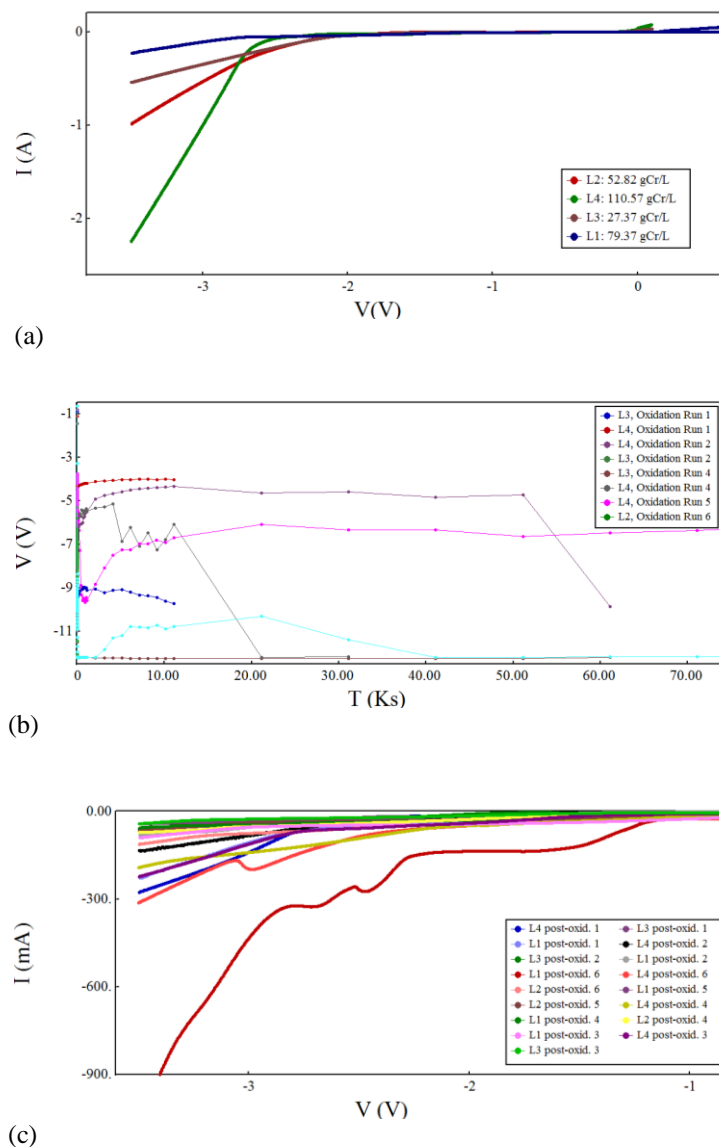
Figure 4.23: (a) Spent H2CrO4 pre-oxidation run CVs (b) Cr oxidation runs voltage response (c) post-oxidation run CVs

Voltage response for current-controlled anode material investigation run with Cr-anode described in § 3.2.5 is plotted in Fig. 4.24. Responses for Cu-anode bath 3 Runs 9 and 12, along with produced deposit images, are shown in Figure 4.25. Runs 9 and 12 were directly successive runs using the same electrolyte under otherwise identical operation conditions.
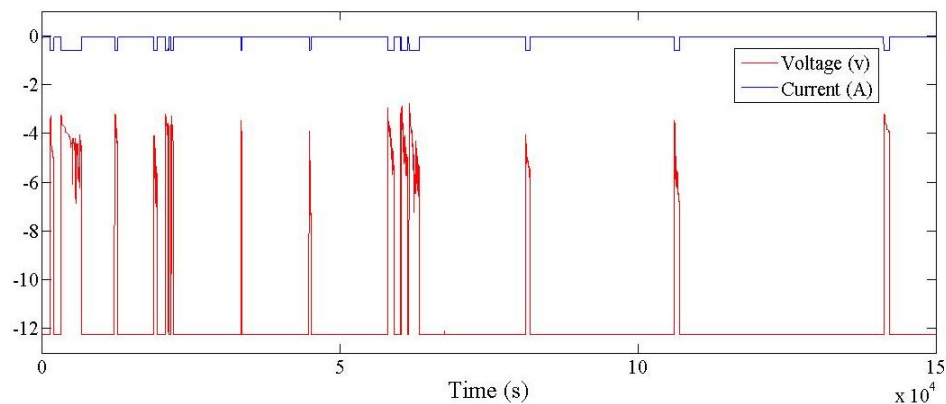
Figure 4.24: Cr-anode run voltage and current
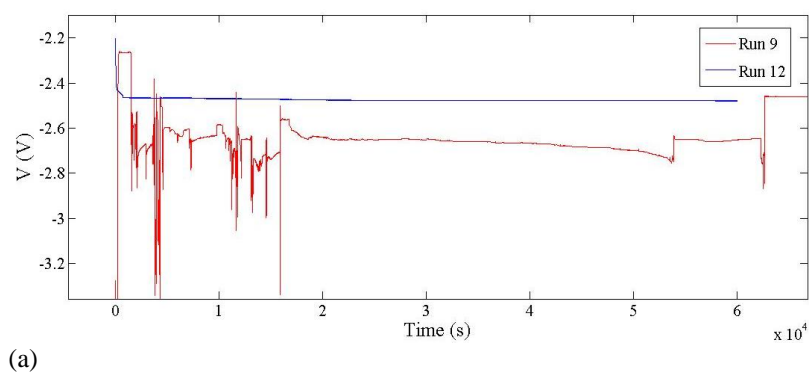
(a)
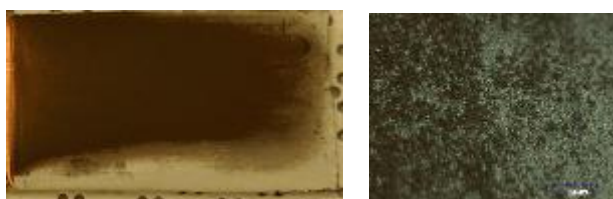
(b)
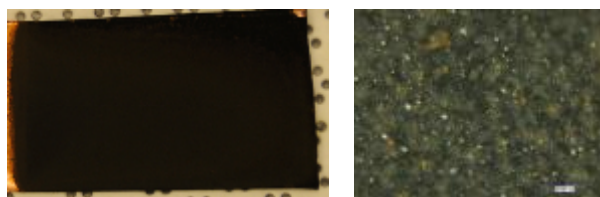
(c)

Figure 4.25: (a) Cu-anode Cr Runs 9 and 12 voltage response (b) Run 9 deposit (c) Run 12 deposit

Chronopotentiometry voltage response from electrode ratio investigations

described in § 3.2.5.1 are normalized by subtracting open circuit potential E_{OC} from

measured voltage. Corrosion potential curves scanned directly prior to plating runs are

averaged to determine E_{oc}.   Overpotential (Eq. 2.21) for constant current density j = -0.3

A/cm^2 is plotted in Figure 4.26. Resulting current efficiency and Cr surface finish are

listed in Table 4.15.
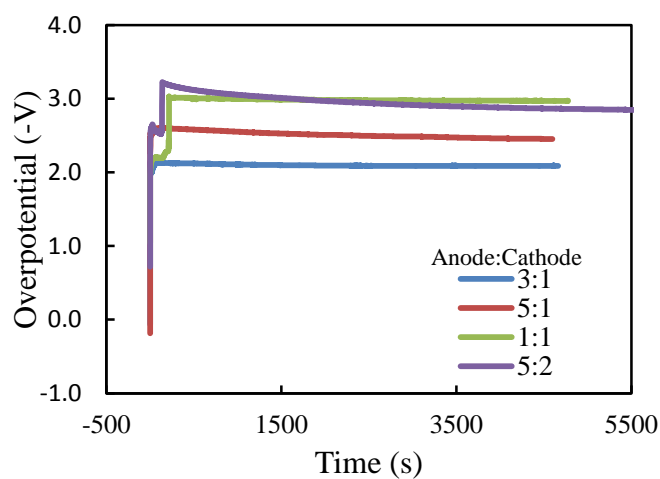
Figure 4.26: Voltage response for Pb anode : cathode surface area ratio

Table 4.15: Current efficiency and surface finish results of electrode ratio studies

Ratio (anode : cathode)	CE (%)	Finish
1:1	2.38	Bright
5:2	2.78	Bright
3:1	7.11	Frosty
5:1	9.47	Frosty

4.2.5 Analytical Examinations

Polarization curves measured with the RDE on H_2CrO_4 electrolytes described in §

3.2.6 are shown in Fig. 4.27.
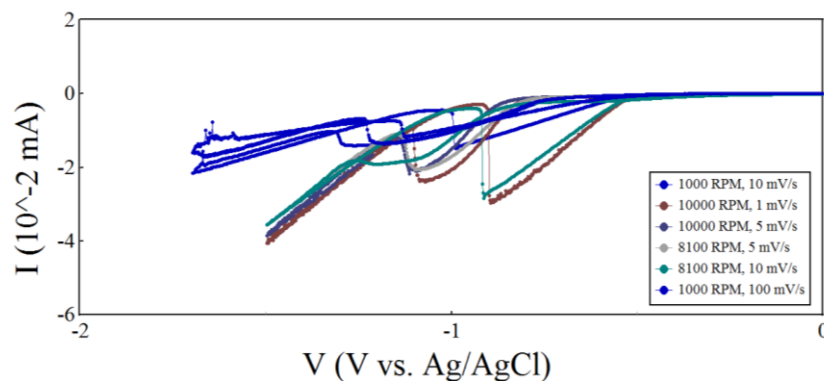
Figure 4.27: H_2CrO_4 RDE polarization curves

Cr current peak magnitude at low scan rates is plotted in Fig. 4.28 (all scan rates showing quasi-reversible behavior are plotted in Appendix D). Plots of potential peak position and current peak magnitude measured in § 3.2.6 are shown relative to concentration in Fig. 4.29, stir rate in Fig. 4.30, and temperature in Fig. 4.31. Cr Tafel plot is shown in Fig. 4.32. Constants for the quasi-reversible Tafel equation (Eq. 2.20) are calculated in Table 4.16.
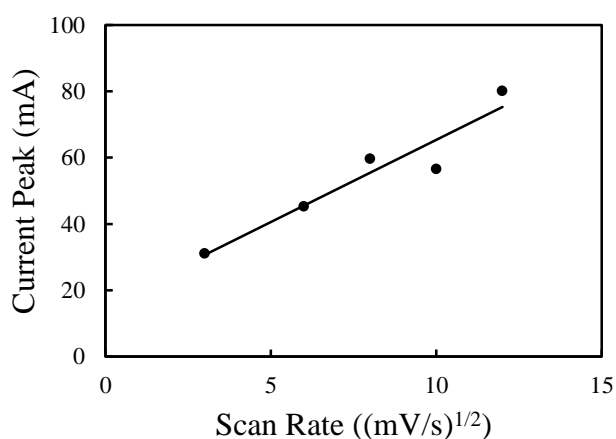
Figure 4.28: H_2CrO_4 CV Peak current relative to scan rate
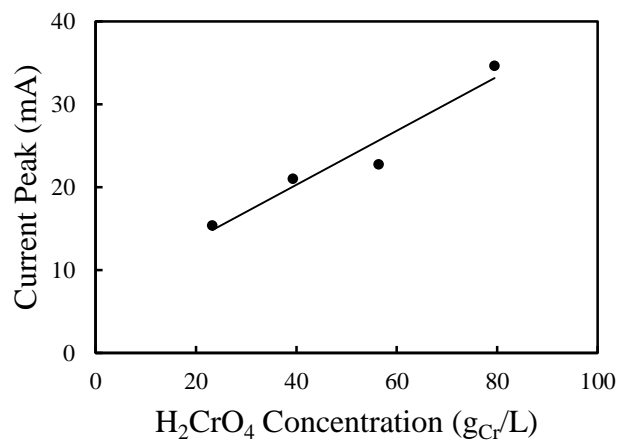
Figure 4.29: Effect of H_2CrO_4 concentration on current deposition peak

(a)

(b)
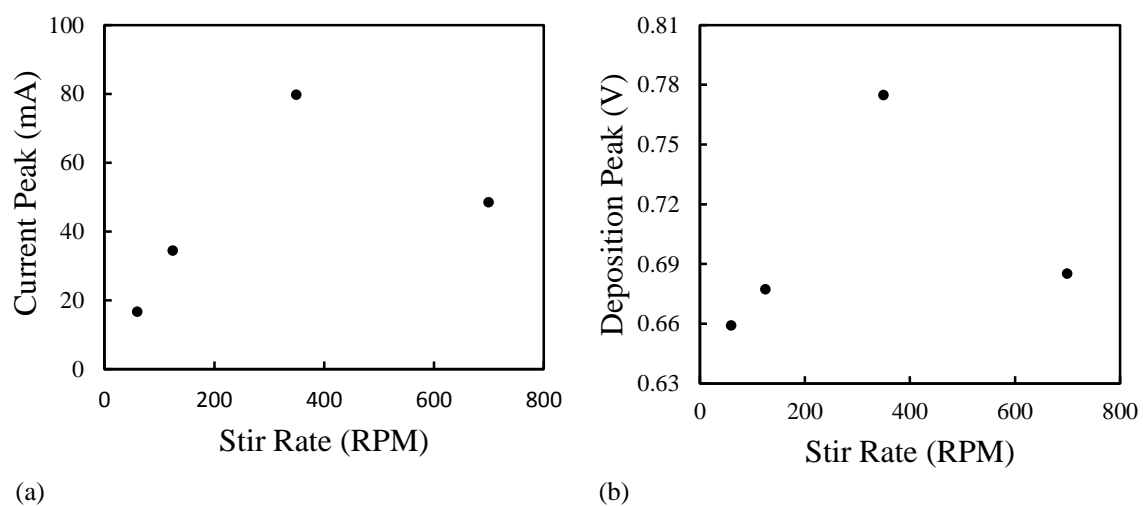
Figure 4.30: Effect of H_2CrO_4 stir rate on (a) current deposition peak (b) deposition peak potential

(a)

(b)
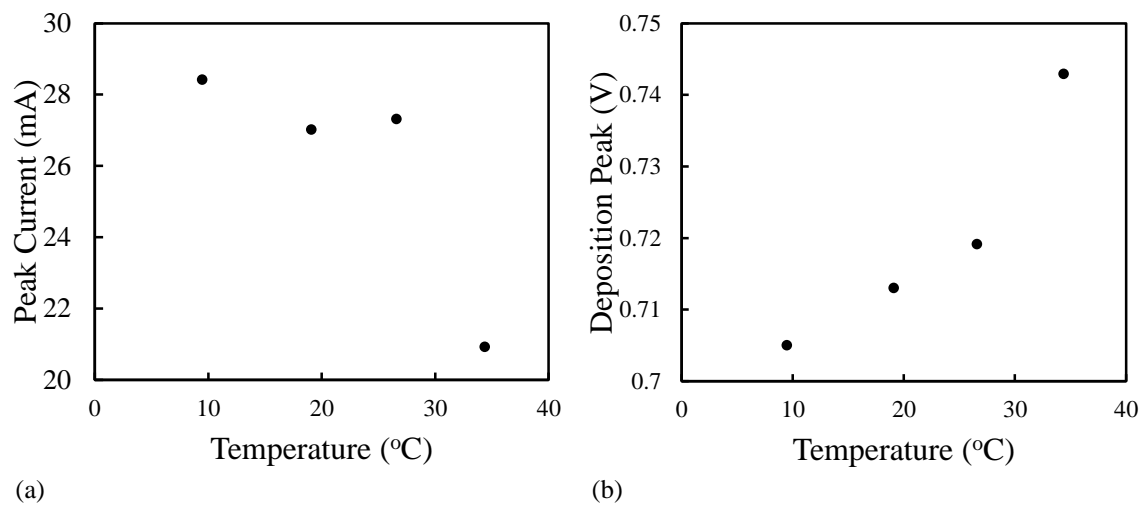
Figure 4.31: Effect of H_2CrO_4 temperature on (a) current deposition peak (b) deposition peak potential
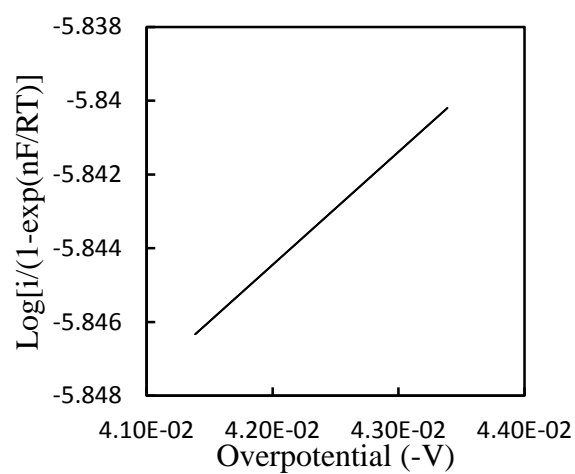
Figure 4.32: H_2CrO_4 Tafel plot

Table 4.16: H_2CrO_4 Tafel constants

Slope b	Intercept a	i_0	α
-3.0616	-5.973	1.0641 E-06	0.1687

4.3 Cu-Cr Experimental Results

4.3.1 Cu-Cr Single Bath

Quality of Cu-Cr deposits resulting from single electrolyte investigations described in § 3.3.1 is shown by images in Fig. 4.33 and micrographs in Fig. 4.34. Pre-run CVs are shown in Fig. 4.35. Voltage response for the current-controlled runs is plotted in Fig. 4.36 and normalized current for the voltage-controlled runs is plotted in Fig. 4.37.

(a) (b) (c)
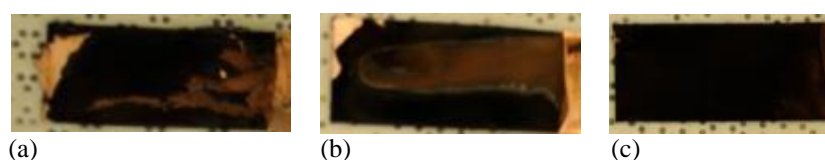
Figure 4.33: Cu-Cr single electrolyte deposits from Cu/Cr relative electrolyte concentrations (a) 75% Cu / 25% Cr (b) 50% Cu / 50% Cr (c) 25% Cu / 75% Cr

(a) (b)

(c) (d)
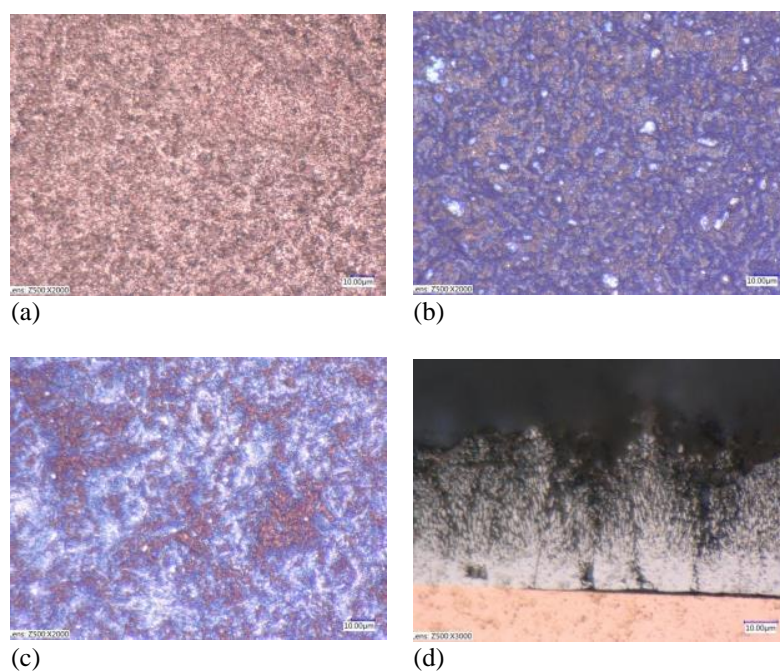
Figure 4.34: Surface micrographs of Cu-Cr single electrolyte deposits produced from Cu/Cr relative concentrations (a) 75% Cu / 25% Cr (b) 50% Cu / 50% Cr (c) 25% Cu / 75% Cr (d) cross-sectional view of co-plated Cu-Cr
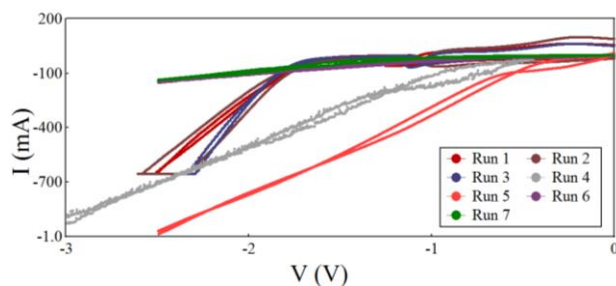
Figure 4.35: CVs for Cu-Cr single electrolyte Runs 1-7
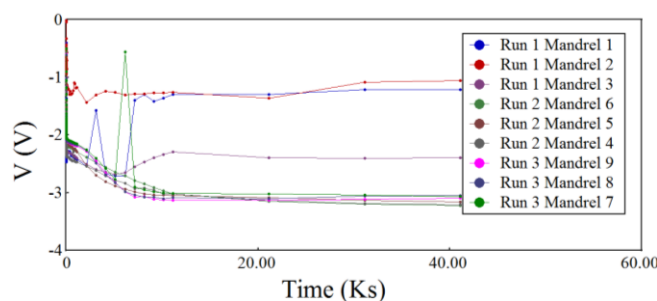
Figure 4.36: Cu-Cr single electrolyte Runs 1-3 voltage response
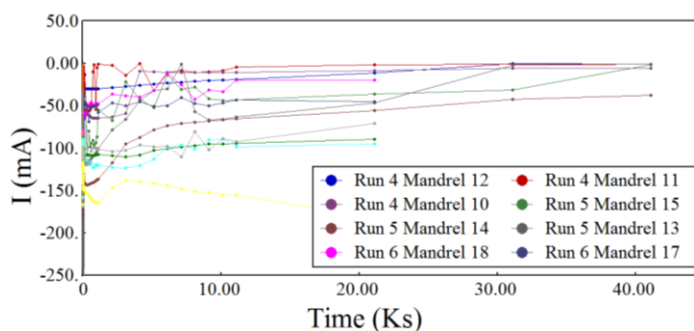
Figure 4.37: Cu-Cr single electrolyte Runs 4-9 current response

4.3.2 Cu-Cr Dual Baths

Cr layer deposits on plated Cu described in § 3.3.2 are qualitatively categorized by deposit finish. Quantitative means of assessing Cr layer deposits are current efficiency, overpotential, and measured throwing power. Throwing power is calculated by measuring Cr deposit thicknesses on cathode both facing and opposing the anode.

The digital microscope is used to measure thicknesses on cross-sectionally mounted and polished samples. Results for Cu-Cr runs with corresponding Cr current density and current efficiency are listed in Table 4.17. Current density is set at 0.03 A/cm^2 for samples with surface area 2700 to 3000 mm^2 by calculation with roughness correction factor listed in Table 4.18 (§ 3.3.2).

Table 4.17: Throwing power of Cr for select electrodeposited Cu-Cr samples

Sample	Throwing Power (%)	j (A/cm^2)	Stir Rate	Finish	Current Efficiency (%)
5.14Mar	26.91		525	Frosty	2.02
2.2Mar	71.92		200	bright	1.61
3.2Mar	62.27	0.03	200	bright	1.64
4.2Mar	94.44		200	bright	2.10

Table 4.18: Roughness correction factor

Run	Roughness correction factor (mm^2)	Finish
35	0	milky
36	0	milky
37	30	milky/bright
38	110	milky/bright
39	130	bright
40	130	bright

Effect of H$_2$CrO$_4$ stir rate on Cr deposited onto plated Cu described in § 3.3.2.1 is shown by voltage response and ability to reduce Cr. Voltage response for each stir rate is shown in Fig. 4.38. The only investigated stir rate to reduce Cr on the Run 7 Cu cathode was 525 RPM. Cr was reduced on the Run 10 Cu cathode at 0 RPM.
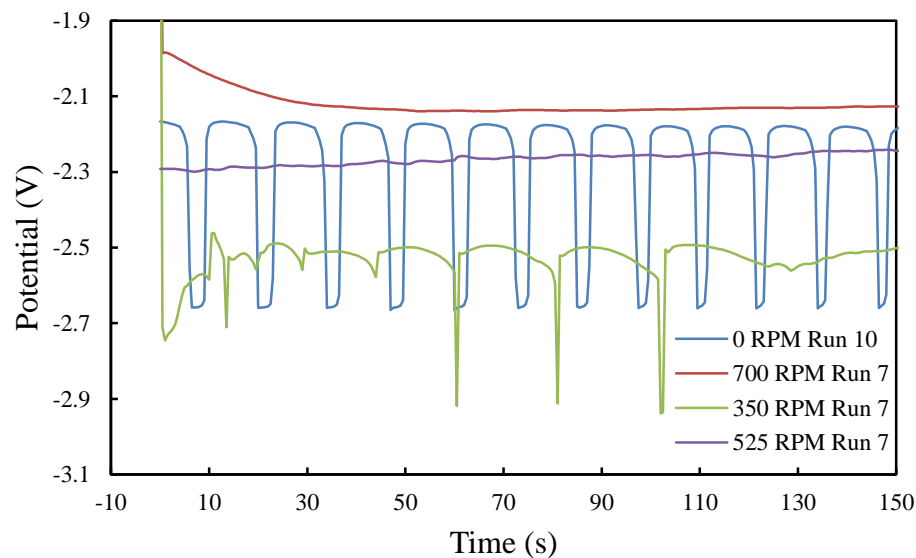
Figure 4.38: Cr deposition voltage response under different stir rates

Adhesion of Cu to plated Cr quantified by ASTM D 3359a tape test resulted in a zero classification for all tests. Results are further qualified by presence of interfacial gap between plated Cu and Cr layers as described in § 3.3.2.2. Table 4.19 shows percentage of samples examined, for under each set of experimental parameters, which exhibited no gap (success rate).

Table 4.19: Results of Cu adhesion tests

Success Rate (%)	Test	Etch
50	Finish: bright	None
50		6 M HNO_3
0	Finish: frosty	None
50		6 M HNO_3
0	Finish: dark	None
50		6 M HNO_3
0	High j	None
50		6 M HNO_3
50	Other Etchants	10 % H_2SO_4
100		50 % HCl

4.4 Heat Treatment Experimental Results

Hardness and extent of Cr-drift were used to quantify annealing and precipitation alloying heat treatments.

4.4.1 Preliminary Heat Treatment Results

EDX maps overlaying SEM images of annealed electrodeposited Cu-Cr samples described in § 3.4.1 are shown in Fig. 4.39. Measured hardness for annealed samples is given in Table 4.20. Initial precipitation hardened samples heat treated as described in § 3.4.2 are shown in Fig. 4.40. EDX revealed Fe contaminants up to 30 um from the Cr layer on several electroplated Cu-Cr samples as shown in Fig. 4.41. Al and Si were detected as being uniformly dispersed in small concentrations over all samples.
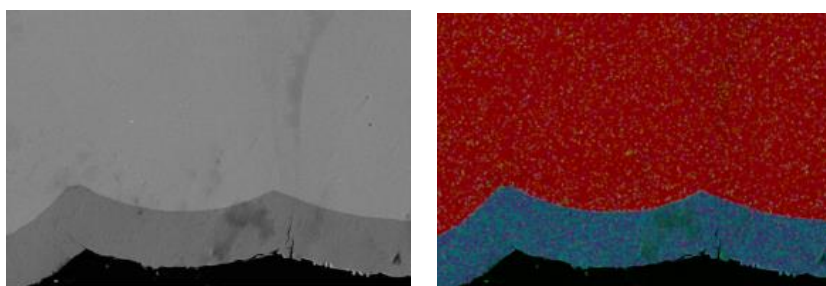
Figure 4.39: SEM image and corresponding EDX map of electrodeposited Cu (red), Cr (blue) layered sample

Table 4.20: Average hardness for select annealing treatments

Annealing T (^{o}C)	Avg Hardness (HV)
no HT	86.37
400	85.85
500	66.45
600	61.17
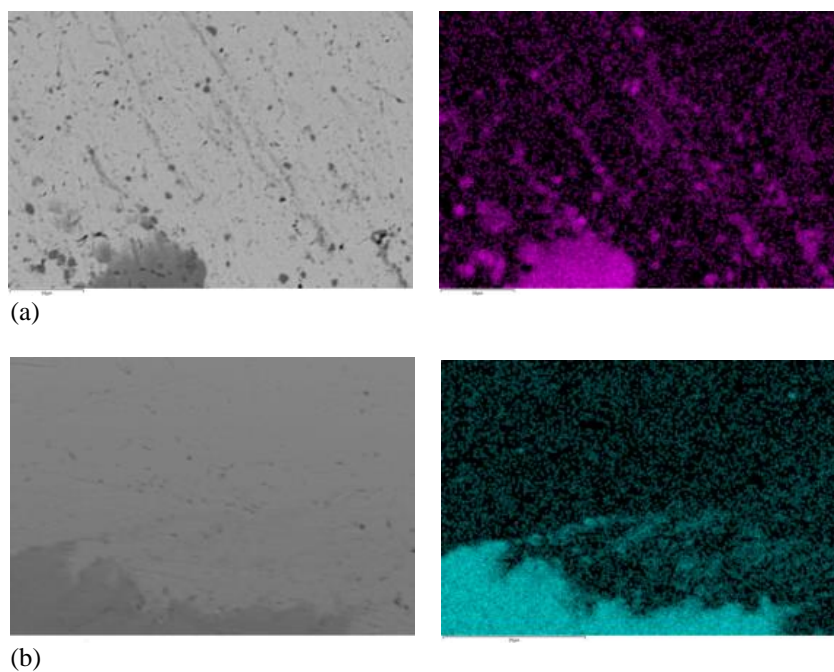
Figure 4.40: Cu-Cr SEM images with associated EDX maps of Cr diffusion for samples (a) Aged at 500 ^{o}C (b) Aged at 400 ^{o}C
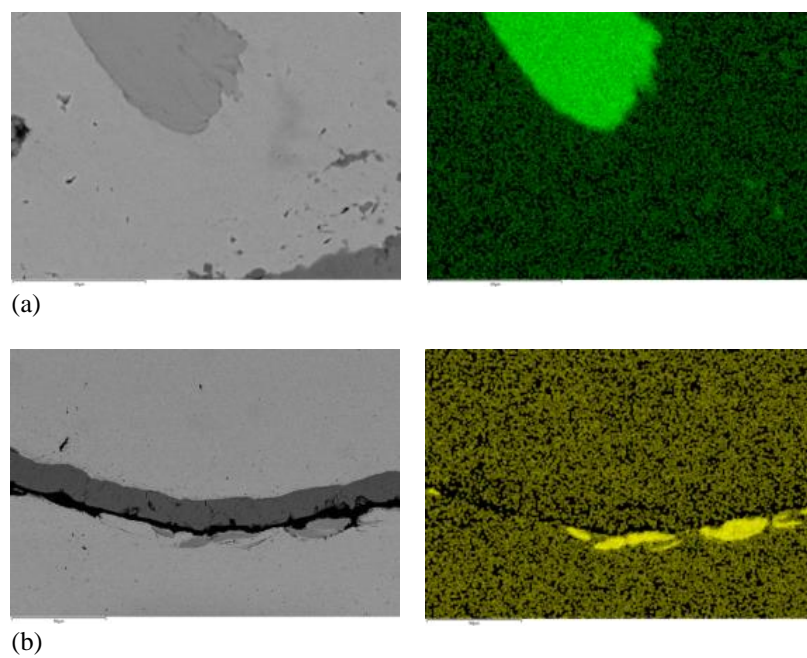
Figure 4.41: Cu-Cr SEM images with associated EDX maps of Fe (a) Solution treated at 980 ^{o}C (b) No HT

Micrographs shown in Fig. 4.42 and EDX overlays with SEM images of solution treatment study samples shown in Fig. 4.43 are described in § 3.4.2. These images show dark, high-contrast bands on either side of the Cr layer. The bands were identified in EDX maps (Fig. 4.43) as being composed of Cr and O, notably devoid of Cu. Average distance of band from Cr-Cu interface is plotted in Fig. 4.44. Ni and Fe were also searched for in EDX spectra; however, no concentrations above background were found.
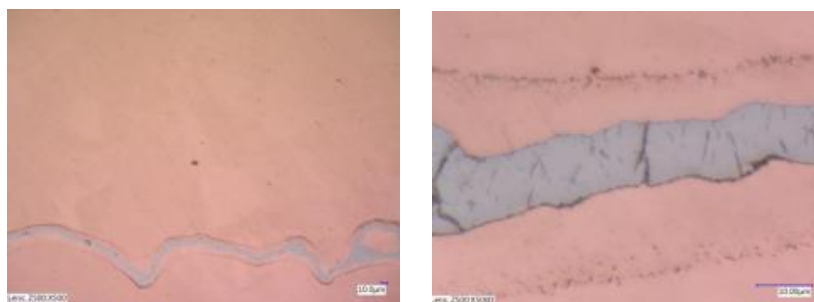
Figure 4.42: Oxide bands in solution treated Cu-Cr sample
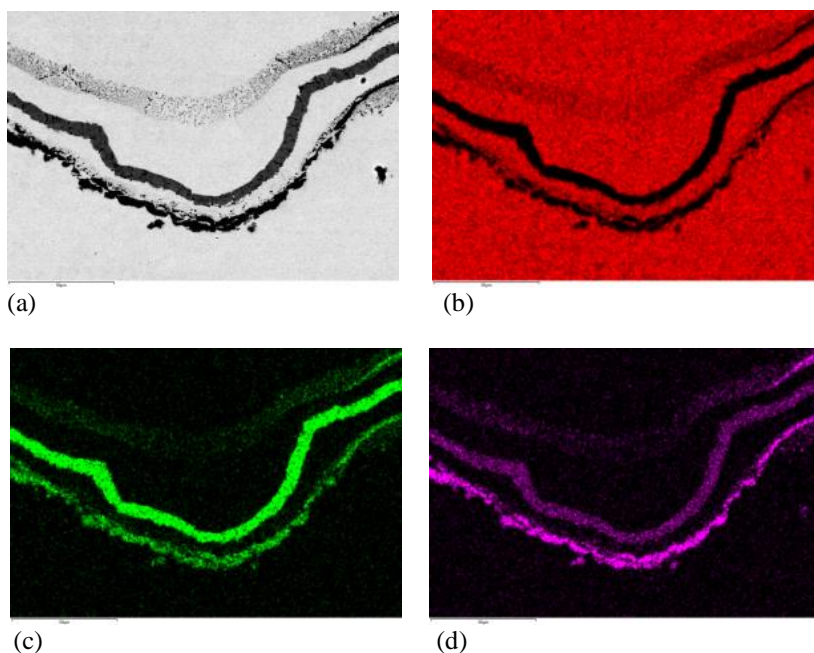
Figure 4.43: Cu-Cr (a) SEM image with (b) EDX map for Cu (c) Cr (d) O
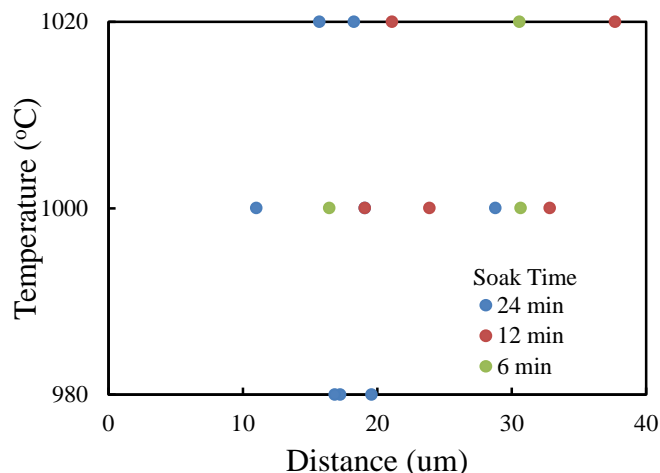
Figure 4.44: Cr-oxide band distance from Cr with solution treating time

4.4.2 Precipitation Alloying

Diffusion of Cr into Cu during solution treating was examined using the SEM as described in § 3.4.3. Fig. 4.45 shows EDX line scans on a solution treatment trial sample exhibiting Cr diffused to a depth of ~1 um in the Cu matrix. When using EDX point and scan, over the larger area, diffusion of Cr was shown to a distance of 40 um from the interface as shown in Fig. 4.46. The diffusion coefficient for Cr in electrodeposited Cu is calculated to be D = 2.24 x 10^{-11} cm^2/s. A least squares fit on the error function solution to Fick's Second Law was used to model experimental diffusion.

(a)   (b)
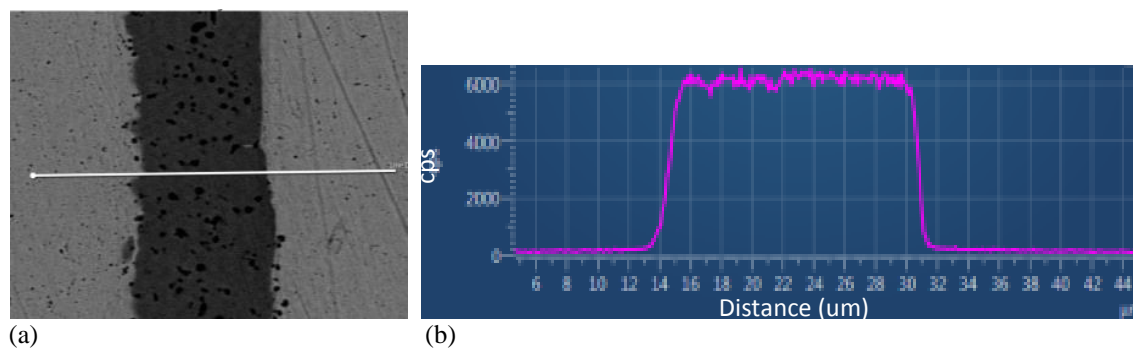
Figure 4.45: SDSMT solution treatment trial SEM analysis (a) Examined interfacial area (b) Cr counts from EDX line scan
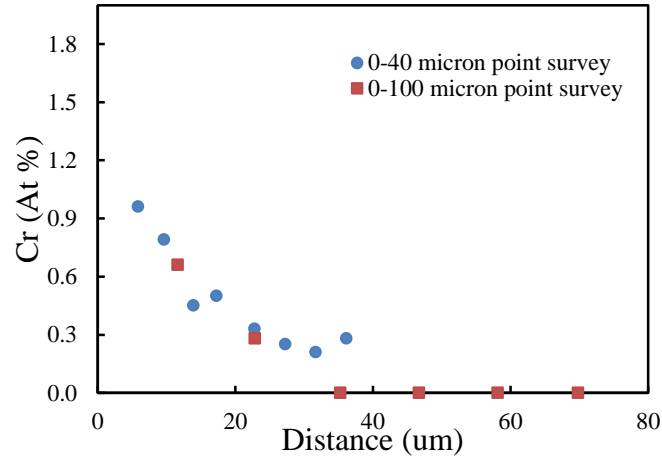
Figure 4.46: EDX determined Cr diffusion into electrodeposited Cu

Electroplated Cu-Cr samples analyzed on the EMSL SEM as described in § 3.5.1 used point and analyze to determine depth of Cr diffusion. The determined Cr diffusion coefficient calculated with least squares treatment of the error function solution (Eq. 2.50) is $D = 3.40 \times 10^{-11}$ cm^2/s with $C_o = 1.70$ wt% Cr as plotted in Fig. 4.47. This value is modeled against the literature diffusion value calculated for solution treatment 1000 ^{o}C 24 hrs with Eq. 2.52 to be $D = 5.086 \times 10^{-10}$ cm^2/s as shown in Fig. 4.48.
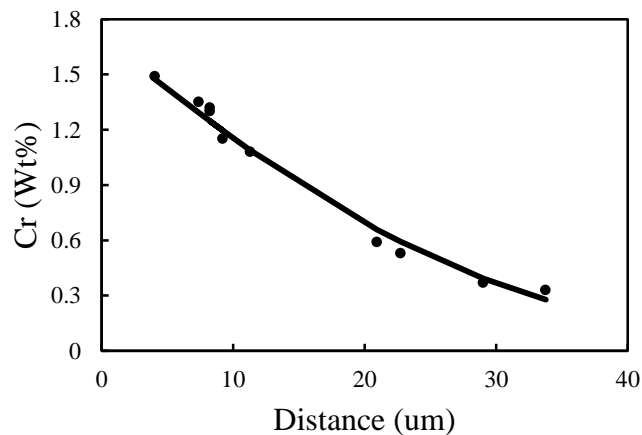
Figure 4.47: EMSL SEM determined Cr diffusion
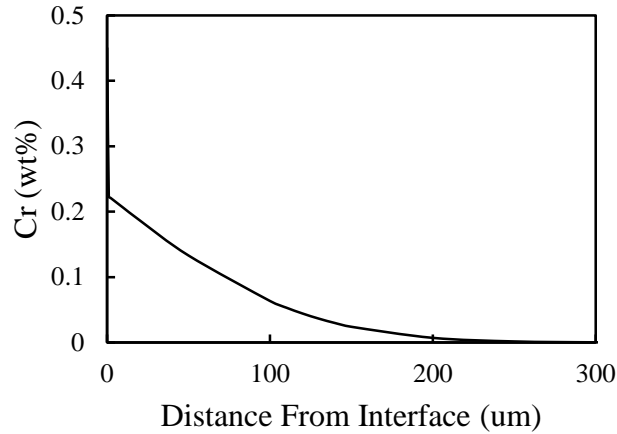
Figure 4.48: Literature Cr Diffusion coefficient

Six samples were rolled in between solution treating and precipitation hardening.

Extent of CW is calculated according to Eq. 2.9. Percent CW for each sample is given in

Table 4.21.

Table 4.21: Percent reduction of Cu-Cr solution treated samples

Sample	% CW
6.22Feb	34.57
5.14Mar	13.45
4.2Mar	40.49
2.2Mar	35.25
1.22Feb	53.33
3.14Mar	38.46

Concentration of Cr dissolved into the Cu matrix is calculated using thickness of

the Cr band in cross-sectionally mounted samples measured with the digital microscope.

Band thickness is determined in each parent, solution treated, and age hardened sample as

shown in Fig. 4.49. Cr band width reduction (% dissolved) for each age hardened sample

is shown Table 4.22. Thickness of band measured in sample 1.14Mar solution treated at

950 ^{o}C at incremental times is plotted in Fig. 4.50.

Figure 4.49: Micrograph measuring plated Cr band width

Table 4.22: Amount of Cr dissolved into Cu matrix during HT

Age T (^{o}C)	Age t (hrs)	% Cr Dissolved
800	4	81.47
		63.02
		82.14
600	12	76.25
		82.73
		77.29
700	4	69.39
		76.81
		80.43
700	1.3	75.15
		62.43
700	12	56.08
		61.03
		57.73
600	1.3	57.42
		49.29
		51.64
800	1.3	35.22
		66.06
500	12	62.07
		22.45
		52.44

Table 4.22: Amount of Cr dissolved into Cu matrix during HT (cont'd)

Age T (°C)	Age t (hrs)	% Cr Dissolved
600	4	100.00
		100.00
		100.00
800	12	58.22
		61.01
500	4	38.38
		16.30
400	12	79.31
		69.20
		52.03
400	4	47.94
800	12	85.02
800	12	100.00
		100.00
400	24	66.18
		100.00
300	24	41.41
		100.00
		100.00
500	18	44.09
		100.00
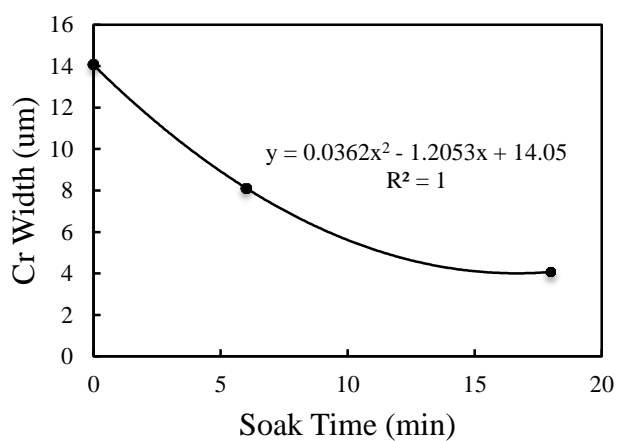
Figure 4.50: Cr ribbon thickness at intermediate solution treatment durations

4.5 Electromicroscopic Characterization

Precipitation alloyed samples prepared as described in § 3.4.3 were examined at EMSL, making use of their SEM and TEM facilities.

4.5.1 SEM

Fig. 4.51 shows SEM texture of each non-CW precipitation hardened sample examined at EMSL using a 10 mm working distance as described in § 3.5.1. CW sample aged at 600 ^{o}C for 4 hrs was imaged on the EMSL FIB/SEM as well, having a working distance of 4 mm. The improvement in resolution is seen in Fig. 4.52. Cr concentration with respect to distance from the Cu-Cr interface as found by point and analyze EDX spectra is plotted in Fig. 4.53 for all samples. Cr concentration from selected area scans of the Cu matrix adjacent to Cr interface are given in Table 4.23.
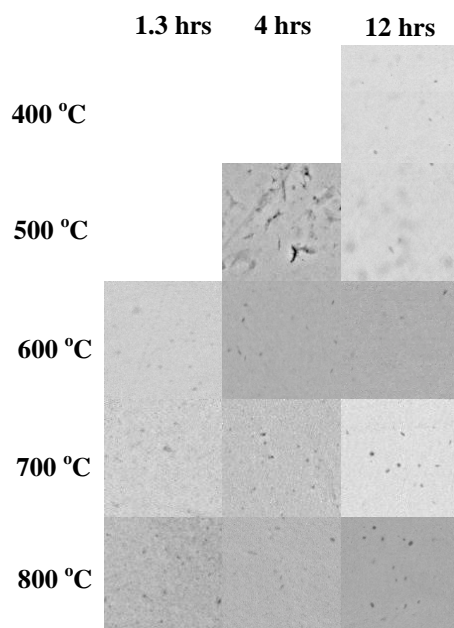
Figure 4.51: Texture of Cr in Cu matrix on precipitation hardened samples of indicated temperature and time
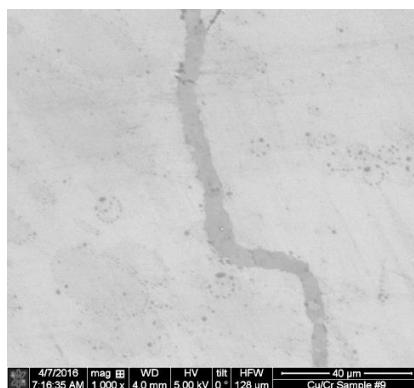
Figure 4.52: SEM image of CW sample aged at 600 ^{o}C 4 hrs
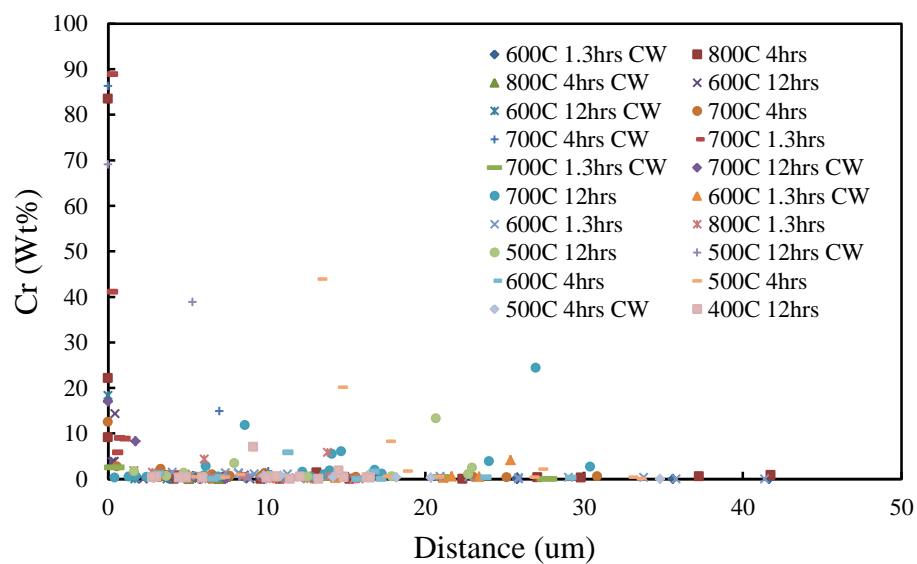
Figure 4.53: EDX spectra Cr concentration relative to distance from Cu-Cr interface for all age hardened samples

Table 4.23: EDX measured average concentration of Cr in Cu matrix for various aging conditions

Aging T (^{o}C)	Aging t (hrs)	Cr (wt%)
500	4	0.47
500	12	0.29
600	1.3	0.75
600	4	0.43

4.5.2 TEM

Precipitates shown in Fig. 4.54 were identified and verified in samples 500 ^{o}C 12

hrs, 600 ^{o}C 12 hrs, and 600 ^{o}C 4 hrs and its CW sample. No verifiable precipitates were

found in samples 800 ^{o}C 4 hrs and 400 ^{o}C 12 hrs as shown in Fig. 4.55. Features shown

in Fig. 4.56a have the appearance of coherent coffee-bean contrast precipitates, and were

found in all samples. Spectra taken of these features show only background Cr

concentrations (Fig. 4.56c). Cr precipitates were found off-axis, as shown in Fig. 4.56b,

and were verified with EDX spectra (Fig. 4.56d). Sulfur was identified in cloud-like

clusters on one side of the Cr strip in M1 as shown in Fig. 4.57. Verified Cr precipitates

and their spacing within the Cu matrix were measured and are listed in Table 4.24.

(a)   (b)

(c)   (d)
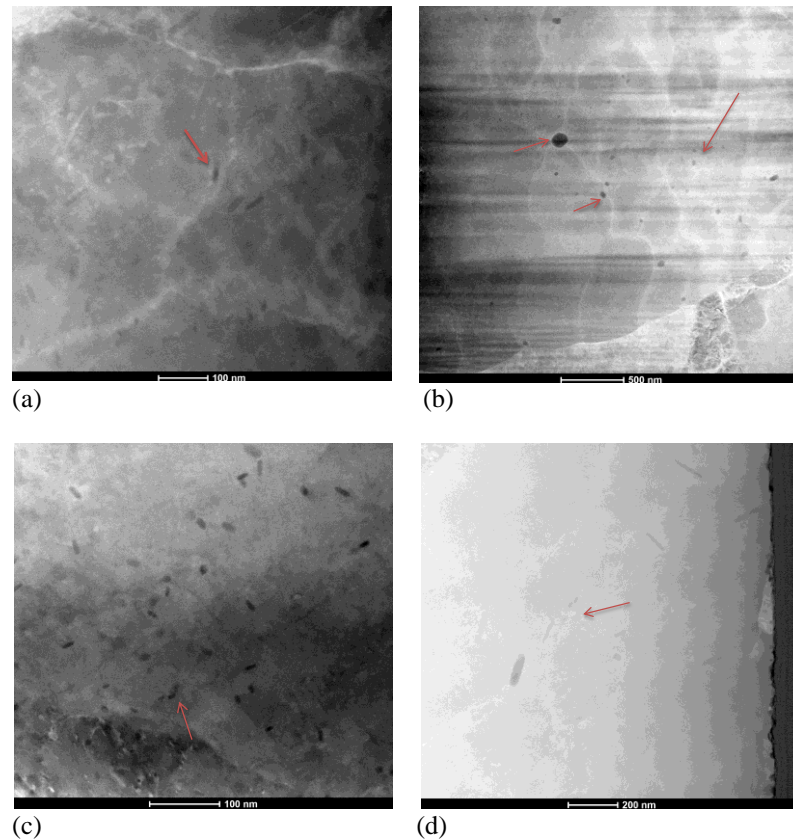
Figure 4.54: TEM images of spectra-verified Cr precipitates in alloyed Cu-Cr sample (a) 600 ^{o}C 4 hrs (b)
600 ^{o}C 4 hrs CW (c) 500 ^{o}C 12 hrs (d) 600 ^{o}C 12 hrs

(a)   (b)
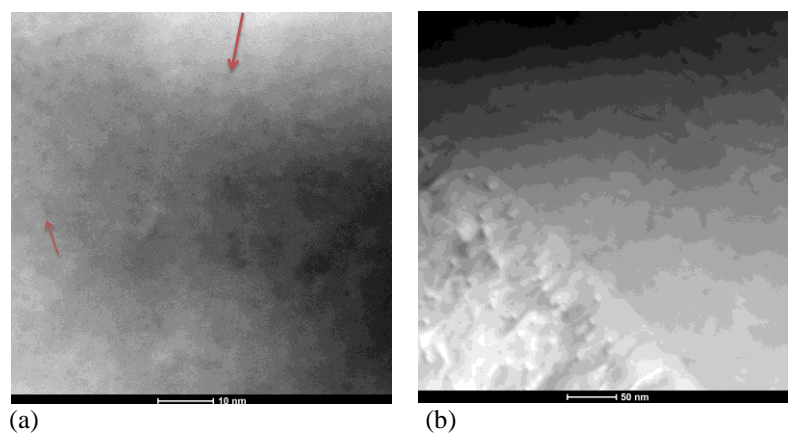
Figure 4.55: Cu-Cr alloy TEM images showing no verifiable precipitates (a) sample aged at 800 ^{o}C 4 hrs (b) sample aged at 400 ^{o}C 12 hrs

(a)   (b)

(c)

(d)
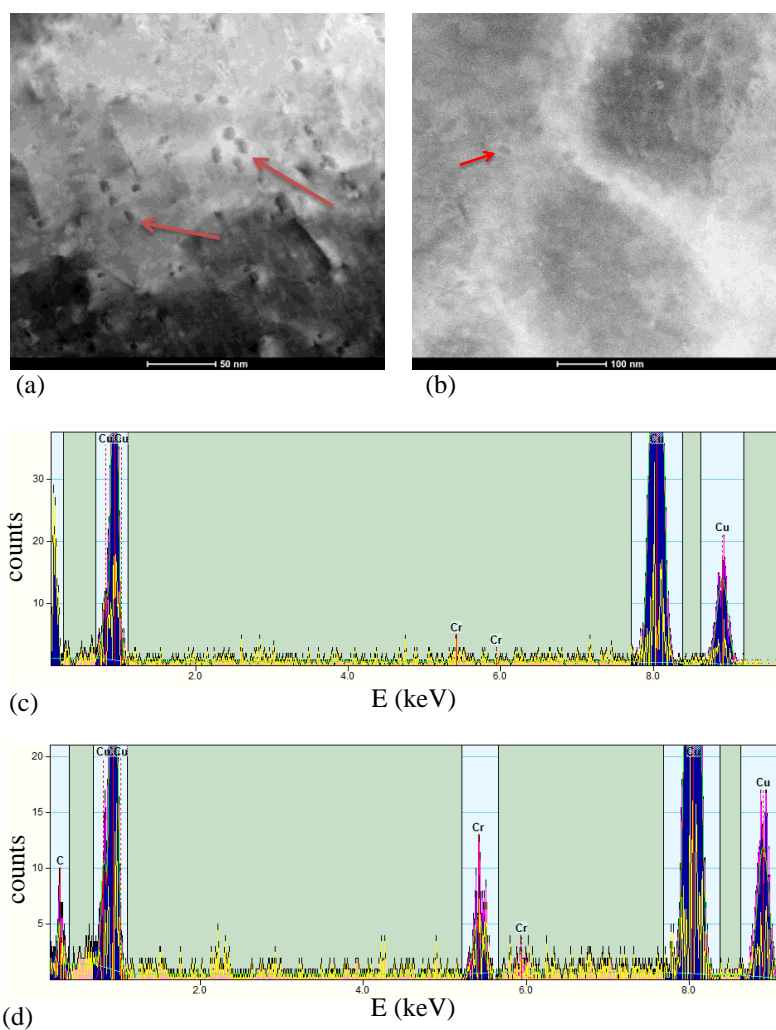
Figure 4.56: (a) Coffee-bean contrast features (b) verifiable Cr precipitates (c) spectrum of features from a (d) spectrum of precipitates from b
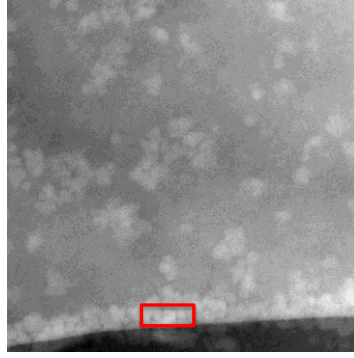
Figure 4.57: TEM image showing Cu-Cr interface with sulfur clusters

Table 4.24: Non-CW alloyed Cu-Cr Cr precipitate size and spacing

	600 ^{o}C, 12 hrs			500 ^{o}C, 12 hrs			600 ^{o}C, 4 hrs		
	length (nm)	width (nm)	Spacing (nm)	length (nm)	width (nm)	Spacing (nm)	length (nm)	width (nm)	Spacing (nm)
avg:	84.86	20.74	148.29	13.03	6.39	12.15	23.08	9.56	19.12
std. dev:	36.57	8.80	103.12	2.59	1.26	7.31	8.70	1.92	7.01
min:	26.10	13.20	20.40	8.15	4.42	3.68	12.00	6.43	8.72
max:	134.00	48.30	293.00	18.90	8.20	30.20	45.60	15.50	32.50

Lattice fringes for sample 600 ^{o}C 4 hrs CW are shown in Fig. 4.58 and sample 500 ^{o}C 12 hrs in Fig. 4.59. Selected area diffraction (SAD) fast Fourier transform (FFT) diffraction patterns were acquired for large Cr precipitates in these samples (Fig. 4.58, Fig. 4.59) and the adjacent Cu matrix in 500 ^{o}C 12 hrs as shown in Fig. 4.60. The crystal orientations were determined and are shown on each SAD image. Measured and calculated lattice constants for the Cr precipitate and Cu matrix are shown in Table 4.25. The linear lattice misfit (Eq 2.4) is calculated for literature[77] and measured values (Table 4.25).

(a) (b)
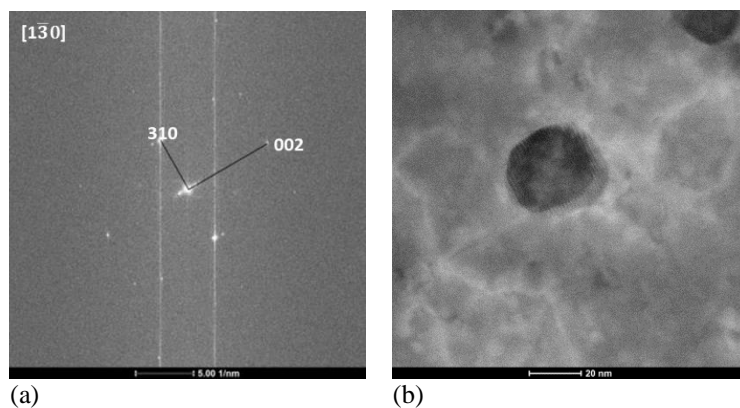
Figure 4.58: (a) Indexed SAD FFT of Cr precipitate in CW sample (b) TEM image with lattice fringes of selected precipitate

(a) (b) (c)
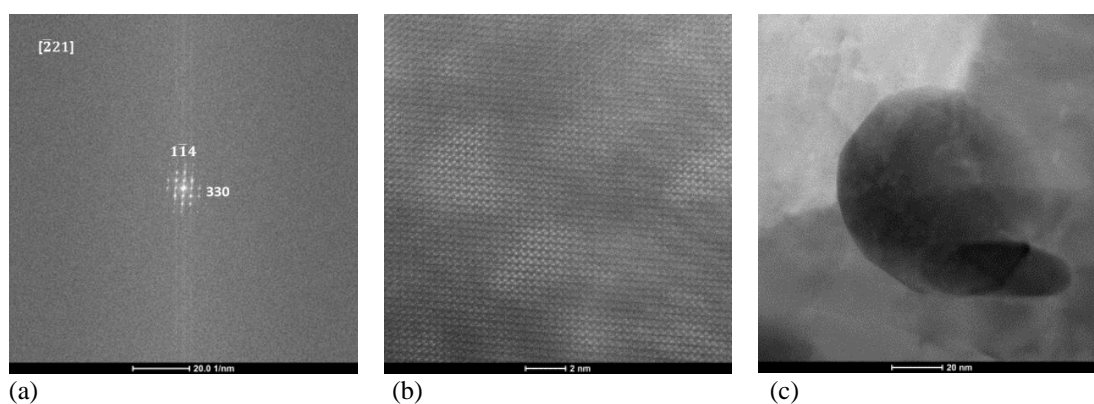
Figure 4.59: (a) Indexed SAD FFT of a Cr precipitate (b) lattice image of selected precipitate (c) associated Cr precipitate

(a) (b)
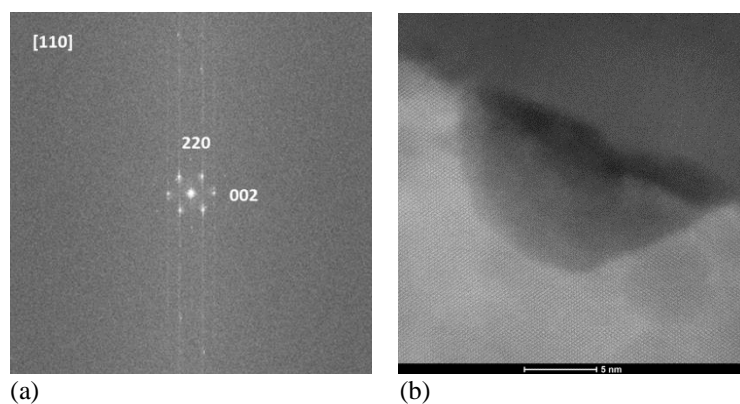
Figure 4.60: (a) Cu matrix indexed SAD FFT (b) Selected Cu area lattice image

Table 4.25: Measured alloy lattice constants and calculated misfit compared to published values

	a_{meas} (pm)	a_{lit} (pm)
Cu	371.75	361
Cr	254.47	288
Misfit (%)	31.55	20

4.6 Physical Characterization Experimental Results

4.6.1 Vickers Hardness

Vickers hardness of electrodeposited Cu-Cr samples described in § 3.6.1 is plotted relative to distance from original Cu-Cr interface. Hardness for all parent samples before and after solution treating is shown in Fig. 4.61. Hardness for the four precipitation HT times and temperatures tested with the highest resulting hardnesses are shown in Fig. 4.62. A summary of min, max, and average hardness results for EFCu produced by PNNL (PNNL Cu), alloyed Cu-Cr parent samples (no HT), solution treated (Sol), solution treated and cold worked (Sol + CW), and aged hardened samples (Aged) is shown in Table 4.26. Aging curves showing max hardness per aging T and t are plotted for both CW and non-CW samples in Fig. 4.63.

The hardness of sample 4.14Mar solution treated at the higher temperature of 1010 ^{o}C as described in § 3.4.3 was measured. The result is a max hardness of 136.73 HV with a 400 ^{o}C 12 hr precipitation hardening.
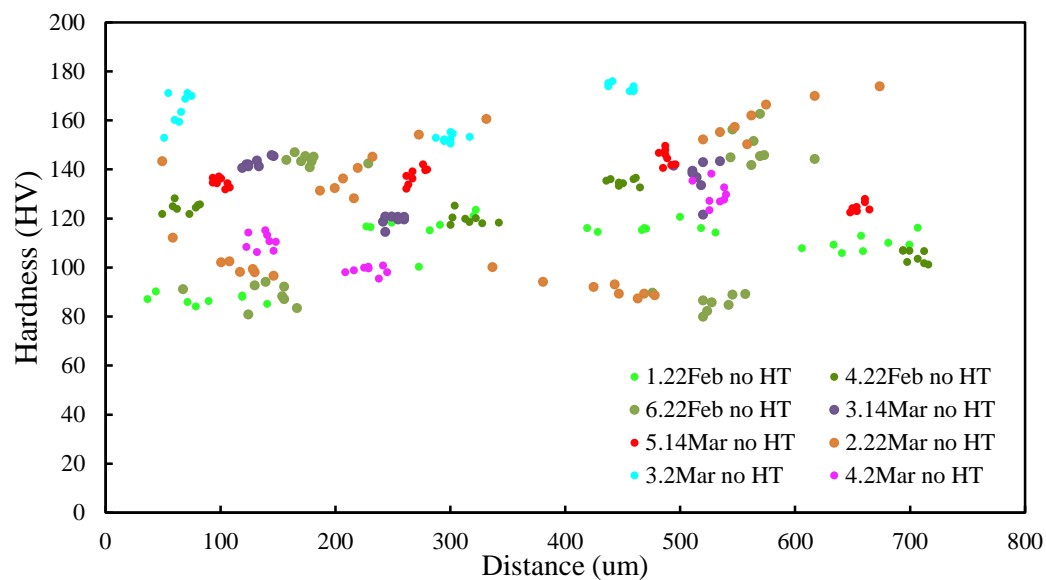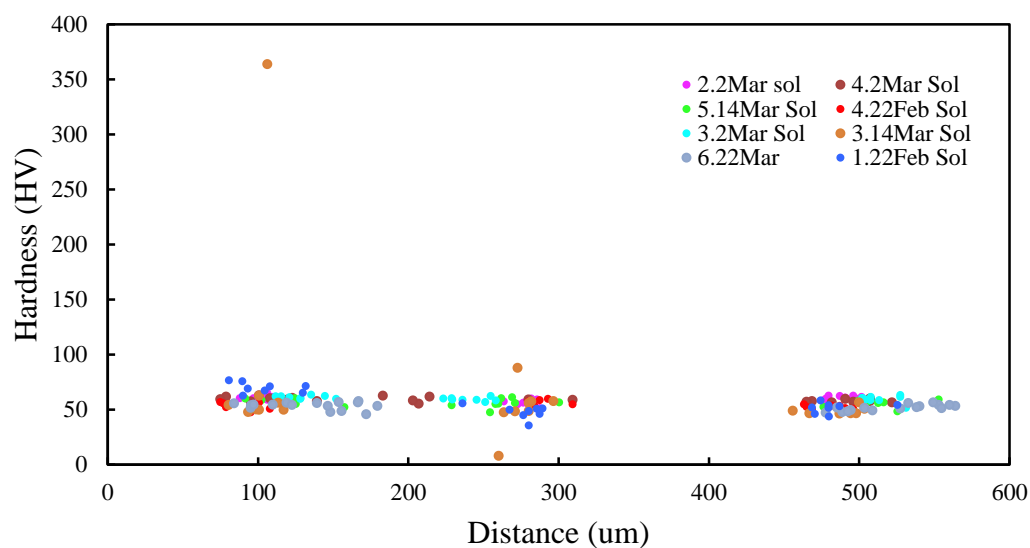
Figure 4.61: Vickers hardness of Cu-Cr parent samples relative to distance from Cu-Cr interface (a) prior to heat treating (b) between solution treating and age hardening
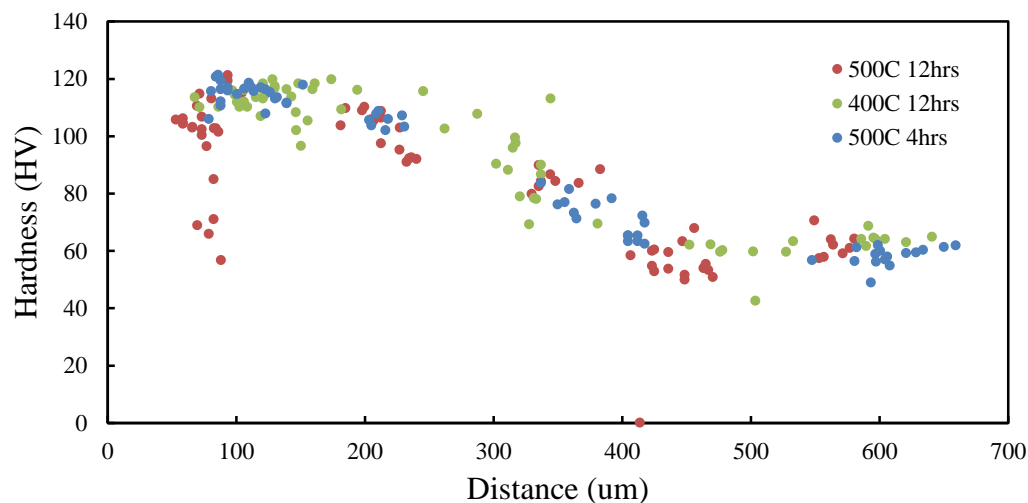
Figure 4.62: Hardness of three hardest precipitation alloyed samples relative to distance from Cu-Cr interface

Table 4.26: Summary of Vickers hardness results

Sample Set	Max (HV)	Min (HV)	Avg (HV)	Std Dev (HV)
PNNL Cu	117	53	72	7.5
No HT	176	80	126	24
Sol	76	35	56	5.6
Sol + CW	142	68	104.9	15.9
Aged	153.8	42.6	77.4	25

(a)

(b)
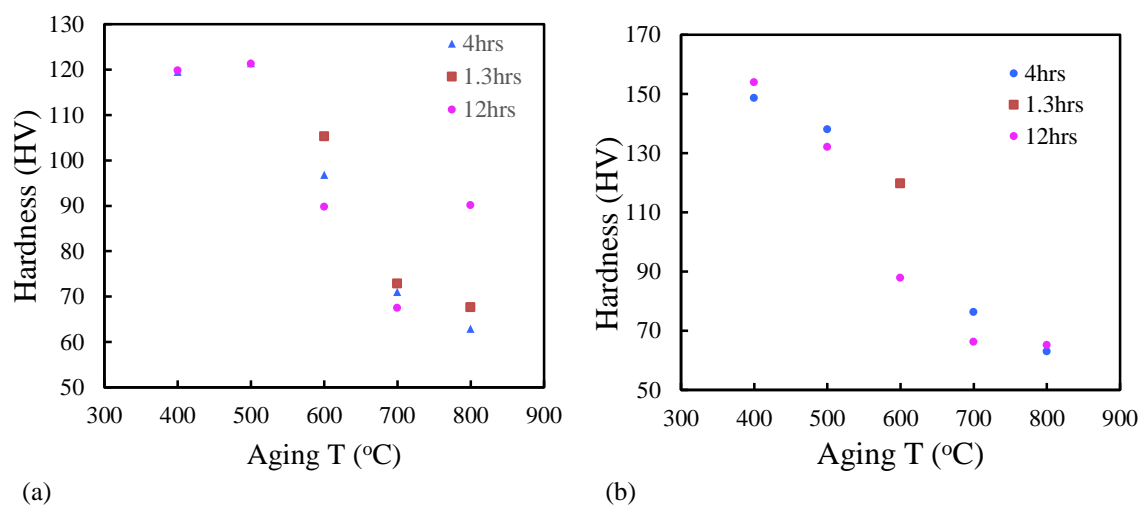
Figure 4.63: Cu-Cr aging curves showing maximum hardness achieved with each T and t (a) non-CW age hardened samples (b) CW age hardened samples

4.6.2 Grain Size

Grain size G is a dimensionless ASTM E112 grain size number calculated by[78]

$$G = [6.6457 \cdot \log(L_3)] - 3.298 \tag{4.1}$$

For mean lineal intercept (grain diameter)

$$L_3 = \frac{1}{N} \tag{4.2}$$

where N is the number of intercepts/length in mm at the specified distance from interface. Grain size values of 00 indicate negative G and annealing twins are ignored in intercept numeration. Solution treated sample grain sizes, for both CW and non-CW samples, are listed in Table 4.27. Grain sizes measured at specified distances from Cu-Cr interface in age hardened samples are listed in Table 4.28.

Hall-Petch plots (Eq. 2.10) for age-hardened CW and non-CW samples are shown in Fig. 4.64. Grain sizes of solution treated CW and non-CW samples are shown in Fig. 4.65.

Table 4.27: Average grain size values for solution treated samples

Parent Sample	L_3 (um)	ASTM G	CW?
6.22Feb	34.09	6.5	
5.14Mar	52.54	5.2	
4.2Mar	209.34	1.2	
2.2Mar	160.34	2.0	x
1.22Feb	49.70	5.4	
3.14Mar	138.55	2.4	
2.2Mar	280.12	0.4	
4.2Mar	322.29	0	
5.14Mar	150.97	2.2	
4.22Feb	469.28	00	

Table 4.28: Average grain diameter and ASTM grain size values for precipitation hardened samples

| HT | | CW? | Dist. From Interface (um) | Avg L_3 (um) | ASTM G |
T (^{o}C)	t (hrs)				
800	4		320.60	315.71	0
		x	95.23	49.98	5.3
600	12		483.28	286.06	0.3
		x	153.08	68.74	4.4
700	4		487.79	615.54	00
		x	39.71	27.46	7.1
700	1.3		201.81	112.95	3.0
		x	86.57	163.68	1.9
700	12		49.40	54.64	5.1
		x	49.40	35.93	6.3
600	1.3		370.79	46.91	5.5
		x	128.49	11.74	9.5
800	1.3		225.90	527.11	00
500	12		201.81	226.91	1.0
		x	62.87	66.49	4.5
600	4		99.40	245.78	0.8
		x	74.63	18.66	8.2
800	12	x	117.91	30.45	6.8
500	4		150.60	301.20	0.2
		x	174.70	272.38	0.5
400	12		297.45	349.34	00
		x	61.27	16.15	8.6
400	4		109.89	193.21	1.4
		x	131.99	229.19	1.0
300	24		142.53	315.76	0
			34.99	39.77	6.0
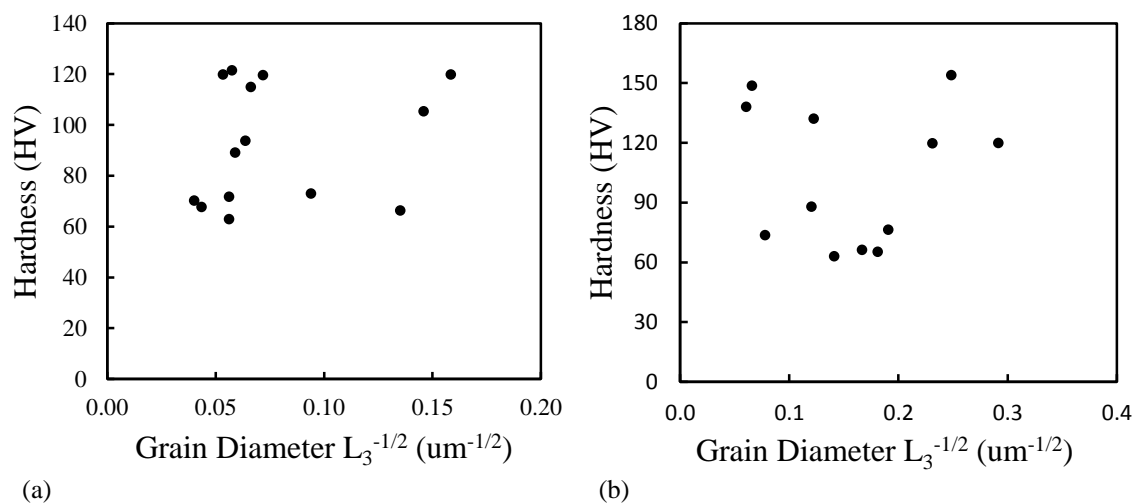
Figure 4.64: Hall-Petch Plot showing hardness relative to grain size for age hardened (a) non-CW samples (b) CW samples
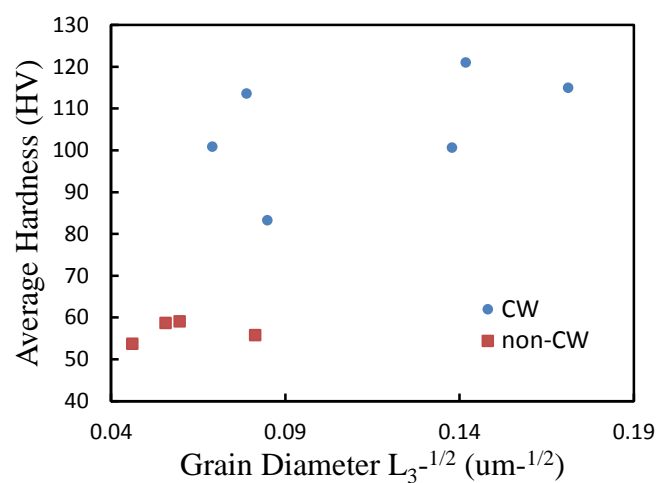
Figure 4.65: Hall-Petch Plot showing hardness relative to grain size for solution treated CW and non-CW samples

4.7 Purity Assay

Plating run voltage response for the three assayed Cr samples plated onto EFCu foil cathodes as described in § 3.7.3 is shown in Fig. 4.66. ICP-MS raw count data output is calibrated in-situ using radioisotope tracers ^{229}Th and ^{233}U. The quantity of ^{232}Th present in each sample is calculated using

$$pg_{Th} = \left(\frac{pg_{229Th}}{Counts_{229Th}}\right) \cdot counts_{232Th} \tag{4.3}$$

where process blank average values are subtracted from sample values. The percent standard deviation is

$$StdDev_{Th} = \left(\frac{\sqrt{RSD_{229}^2 + RSD_{232}^2}}{100}\right) \cdot pg_{Th} \tag{4.4}$$

and it follows for ^{238}U. The limit of detection (LOD) is three times the standard deviation of the process blanks. The amount of each radioisotope recovered is calculated by

$$pg_{recovered} = \frac{process\ blank\ counts}{check\ standard\ tracer\ (pg/g)} \cdot tracer\ count\ for\ sample \cdot g_{sample}. \tag{4.5}$$

The concentrations of U, Th for samples of alloyed EFCu-Cr and Cr plated onto rolled Cu as described in § 3.7.2 are listed in Table 4.29. Sample EFCu-Cr 2 is shown as < LOD, which indicates the value is below the limit of detection and reported pg/g value is an upper bound. U, Th concentrations for Cr plated onto EFCu foil are given in Table 4.30. U, Th concentrations from their corresponding electrolytes and source Cr samples described in § 3.7.4 are given in Table 4.31. The rejection rates of U and Th from electrolyte in Cr electroplated on EFCu foil (Cr_1, Cr_3, Cr_5) are given in Table 4.32.
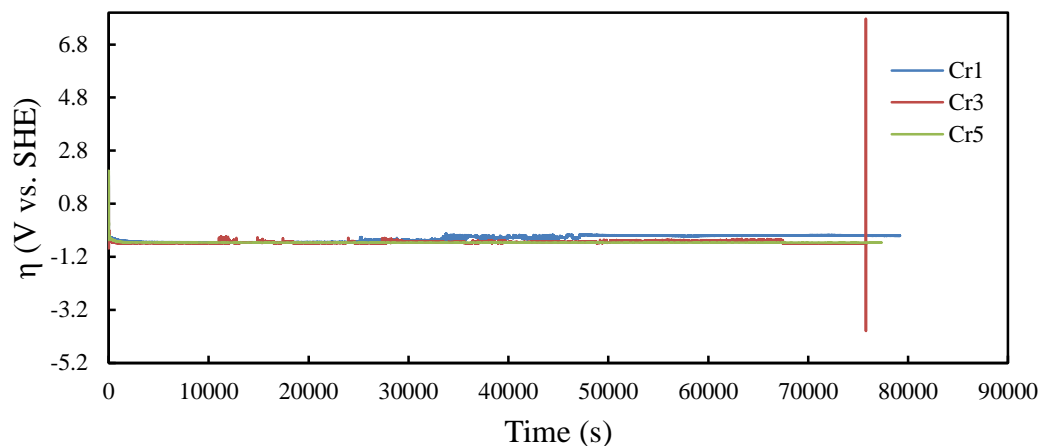
Figure 4.66: Deposition overpotential of assayed Cr samples plated on EFCu foil

Table 4.29: Cr plated onto rolled Cu and plated Cu-Cr samples assay results

Sample	C_{Th} (pg$_{Th}$/g$_{Sample}$)	Std Dev	C_U(pg$_U$/g$_{Sample}$)	Std Dev	% Recovery	
					229	233
Rolled Cr-1	148.82	3.75	4.74	0.67	69.0	37.2
Rolled Cr-2	140.64	10.46	2.45	0.56	44.9	21.3
Rolled Cr-3	47.60	4.09	3.77	0.35	50.1	33.5
Rolled Cr-4	90.078	4.39	4.80	0.72	45.9	25.8
EFCu-Cr 1	0.48	0.096	0.29	0.23	51.0	26.1
EFCu-Cr 2	0.26	<LOD	0.077	<LOD	48.0	26.7

Table 4.30: Cr-on-EFCu foil assay results

Sample	C_{Th} (pg$_{Th}$/g$_{Sample}$)	Std Dev	C_U(pg$_U$/g$_{Sample}$)	Std Dev	% Recovery	
					229	233
Cr$_1$ on EFCu foil	10.45	1.30	5.14	1.65	69.0	37.2
Cr$_3$ on EFCu foil	702.53	19.36	176.81	31.83	44.9	21.3
Cr$_5$ on EFCu foil	8.72	0.32	2.37	0.61	50.1	33.5

Table 4.31: Cr source samples and Cr-on-EFCu foil electrolyte assay results

Sample	C_{Th} (pg_{Th}/g_{Sample})	Std Dev	C_U (pg_U/g_{Sample})	Std Dev	% Recovery	
					229	233
VIM Cr	521.88	<LOD	3134.42	<LOD	69.0	37.2
CrO_3	319.35	<LOD	1918.063	<LOD	44.9	21.3
Cr_1 Electrolyte	153.16	9.91	211.20	29.48	50.1	33.5
Cr_3 Electrolyte	144.03	32.11	202.60	29.54	45.9	25.8
Cr_5 Electrolyte	181.56	43.79	224.31	37.63	51.0	26.1
Aluminothermic Cr	6733.37	142.53	1084.62	62.64	48.0	26.7

Table 4.32: Rejection rate

Sample	Rejection rate	
	Th	U
Cr_1	14.59	41.12
Cr_3	0.21	1.15
Cr_5	20.82	94.76

5. DISCUSSION

5.1 Cu-Cr Alloy Development

5.1.1 Alloying Alternative

The purpose of this work was to develop a mechanically superior radiopure alternative to EFCu, with the proposed solution being a low wt% Cu-Cr alloy. In conjunction with a Cu-Cr alloy solution, other less involved strengthening methods were investigated for value. Commercially Cr is hard-plated onto softer metals to improve wear performance by limiting ductility. This was investigated as an alternative to alloying in radiopure applications. This would be specifically applicable to EFCu threaded parts which must, for use in MJD, currently be taken to the surface and coated with Paralyene. Without such coating both galling and plastic deformation of threads occurs, rendering the part single-use only. The Paralyene dimer itself, without the added contamination from coating steps, has been assayed to contain as much as 390 pg_{Th}/g and 6230 pg_U/g[1].

Samples plated with Cr finishes frosty, bright, dark/milky and barely (§ 4.2) were hardness indented. The resulting hardness's (Table 4.13) show only slight increase for all cases. The indent effect on the Cr is shown in Fig. 4.15. Bright, which displayed the largest hardness increase, and frosty finishes both exhibit extensive cracking from hydrogen adsorption and high stress on brittle deposits high plating current density (Fig. 4.14). The measured hardness's of these samples cannot be considered quantitative because of the cracking. Surface cracking is detrimental for radiopure applications. Pure electroplated Cr, which has orders of magnitude higher levels of U and Th than that of

EFCu (§ 4.7), would not be suitable for use in radioassay detectors if pieces were chipping off near detectors during use. Therefore, bright and frosty finish Cr surface plates would be an unacceptable method of improving mechanical properties. Dark finish however demonstrates a 10.5% hardness increase without cracking (Table 4.13). It is plated at lower j and η, decreasing internal stress by increasing adsorbed ion mobility (allowing lower-energy bond formation). Decreasing j and η also drives fewer contaminants, such as U and Th, to co-deposit as will be discussed in § 5.2.

Annealing Cr surface plated samples as means of increasing adhesion and of mitigating contamination from Cr surface removal was investigated. Annealed Cu, Cr studies show no Cr drift at temperatures up to 600 $^{\circ}$C (Fig. 4.39). The hardness starts to radically decrease after 400 $^{\circ}$C (Table 4.20), negating the value of annealing.

As seen by the small increase in hardness on dark finished samples, Cr coating EFCu threaded components would not significantly prohibit their plastic deformation. Galling, however, is a result of bond-matching adhesion between coupled parts. As discussed in § 2.2, Cr possess a different crystal structure than Cu as well as large lattice misfit. Cr coating parts that screw into Cu would prevent galling, independent of Cr thickness plated so long as surface coverage is maintained. Table 4.30 shows that the aforementioned high concentrations of U, Th in the current solution of Paralyene coating are many times higher than concentrations in the developed electrorefined Cr.

5.1.2 Cu-Cr Single Electrolyte

Cu-Cr single electrolyte studies were conducted with aim of constructing a Cu-Cr alloy through potential waveform modulation. This would allow selective ion deposition as predicted by the Nernst Equation (§ 3.3.1) and alloy composition control. Literature

provides no data on Cr(VI)-Cu co-plating. While the reduction chemistry of Cr(VI) is debated and investigated in detail and still not very well understood, all that is said about co-deposition is that it is not done[32]. A look at the coordination chemistry involved shows that Cr continuously polymerizes with other ions in solution (§ 2.3.6), which can include Cu when present.

Deposits resulting from both mixed Cu-Cr electrolytes (Figure 4.33, Figure 4.34) and Cu anode Cr baths (Figure 4.25) are black, amorphous, lack cohesion, and generally of poor quality. Cu anode Cr baths maintained the specified $Cr:SO_4^{2-}$ ratio which protects the Cr complex, while adding only Cu ions. Voltage response shown in Figure 4.25 shows an increase in voltage and noise with increasing Cu dissolution into the Cr electrolyte. The voltage increase indicates an increase in solution resistance with Cu, moving the driven voltage nearer to reducing U and Th. Signal noise is a result of current interruptions prompting rise in V to recover the set current. Current interruptions, when not the result of faulty connections, indicate lack of charge transfer to reducing Cr ions. This occurs in H_2CrO_4 coordination chemistry when the Cr^{6+} complex is blocked by an excess of sulfate ions; however, for this system the ratio is set and the complex must be blocked by Cu ions. The co-deposition of a Cu-Cr complex is seen in black deposits. Mixed Cu-Cr electrolyte bath deposits, including those set at low overpotentials (Figure 4.33) in which only Cu is driven to reduce, offer the same poor quality. Overall the Cu and Cr are complexing and co-depositing, the chemistry of which is beyond the scope of this study other than to state that a Cr(VI)-Cu single electrolyte configuration is not suitable in constructing a Cu-Cr alloy.

5.1.3 Cr Cell Construction

Investigations in Cr cell anode materials (§ 4.2.4) showed PbO_2 to be the most suitable material because of Cr^{3+} to Cr^{6+} catalyst properties described by electrochemical Eq. 2.38. Fig. 4.23b shows a decreasing oxidation run voltage for all oxidation methods described using an inert anode. Therefore, the concentration of reducing species, which would lower the solution resistance and thus the voltage response, did not significantly increase during the runs. Fig. 4.23a shows CVs pre-oxidation, and Fig. 4.23c shows forward polarization curves post-oxidation. Notice that the only run with a significant increase in plating peak current is bath L1, post-oxidation Run 6; this is the only run shown which uses a PbO_2 anode instead of an inert anode.

Cu anodes are not chosen for use, for reason previously described in § 5.1.2. Fig. 4.24 shows current and voltage of a current controlled Cr plating run in which Cr-anode material is connected by Ti-strips. This is the same method used in this work for Cu anodes in both Cu and Cr baths (§ 3.1, 3.2). As shown by voltage response, where a potential of -12 V indicates infinite resistance, there is poor connection between Cr and Ti. The voltage response shows that potential starts increasing as much as 4 V while current is flowing before jumping to -12 V. This shows gradually increasing resistance before connection loss, indicating that the connection is not a result of Cr nuggets moving off the inactive Ti-connection strips, which would result in sudden current loss. Rather, this behavior indicates a dissolution or passivation layer building up around the anode before separating it from the Ti. This layer is also being perturbed by solution flow (dissolution layer) or dissolved into solution (passive layer) allowing regained periodic connection. The high affinity for Cr passivation at increased potential coupled with the

solubility of Cr oxides in H_2SO_4 based solutions, such as the electrolyte, point to a passivation mechanism. Also this behavior was not noticed with Cu anodes, for which the Cu Pourbaix Diagram shows possesses no passivating oxide at high potentials and low pH.

The increased voltage used to account for lost Cr anode connectivity results in Nernstian deposition of elements with higher electronegative potentials, such as U and Th. At the current-carrying potentials shown during the run in Fig. 4.24, all elements in solution thermodynamically may reduce. Therefore, Cr was not selected as anode material.

Contamination from PbO_2 anodes encapsulated in deposits is a concern as lead is not radiopure (§ 2.1.3)[1]. The oxide layer degrades over time, dependent upon passivation technique (Fig. 4.22). Pb^{2+} has a half cell potential of -0.13V vs. SHE with stability in the plating cell's operating Eh/Ph region. Pb forms an insoluble sulfate compound in sulfuric acid solutions but is protected by the lead oxide passivation layer.

Electroplated Cr samples assayed for radiopurity were deposited using PbO_2 anodes passivated according to the most stable procedure (Table 3.6, Table 4.14). This was qualified by corrosion potential slopes for passivated anodes:

1. slopes with large magnitude or low R^2 values over time are unstable (anode L6 and B1)
2. positive slopes indicate increasing resistivity of anode which results from degrading or inactive passivation layer (anode L4, A7, and B2)

3. low magnitude slopes with high R^2 values are maintaining their protective and active passive oxide layer over time, and least likely to contaminate electrolyte (anode A5)

Assay of the electrolyte for these baths, composed of CrO_3, H_2SO_4, and DI H_2O have consistent radiopurity (Table 4.31). CrO_3 U, Th concentrations reported, while much greater than that of the electrolytes made from CrO_3, were under detection limits because of the gross dilution necessitated. The actual concentrations could be much lower than this upper limit, and lower than the concentrations in the electrolyte. A significant increase in levels between starting CrO_3 and end electrolyte would indicate PbO_2 anode contamination; however, any information on such contamination cannot be gleaned with data resulting from currently developed Cr assay methods.

The one element that was found in deposits and is a source of possible contamination was Fe in initial precipitation alloying studies (§ 4.4.1). The 316 SS cathode, which had not been removed during HT was suspected, however further investigations into deposits revealed none of the Ni which would have preferably diffused from the SS. Non-HT deposits from other mandrels in the same run were further examined with EDX, and Fe was identified on the Cu, Cr interface in a sample (Fig. 4.41). An examination of 304 SS alligator clips used to connect cells to potentiostats showed that they had been dissolving into the specific baths in question. They were replaced with higher grade connections and the problem was not again observed.

Cr electrode ratio was investigated as it affects (1) required bias potential for Cr deposition and (2) concentration of Cr^{3+} oxidized to Cr^{6+} and, therefore, current

efficiency. Increasing anode : cathode ratio decreases required driving potential for Cr as seen in Fig. 4.26, seemingly beneficial to radiopurity. However, the bias is not changing the Nernstian reduction potential since there is no change in ionic activity or temperature. Fig. 5.1 shows that overpotential is not linearly changing either cathode or anode size. This indicates a charge transfer limiting rate step is not causing the voltage change.
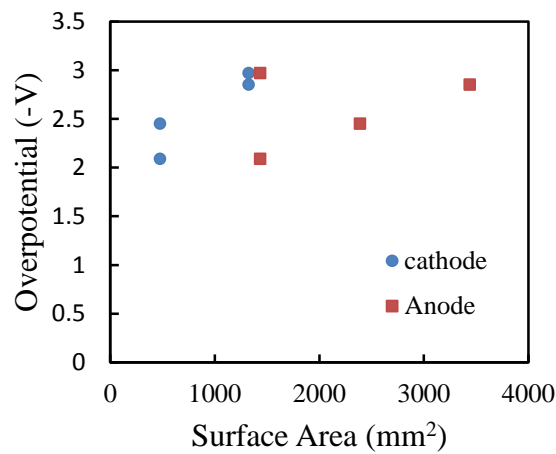
Figure 5.1: Change in overpotential with electrode area

Gauss's Law for a charging concentric cylindrical capacitor[79] is

$$V = \frac{Q}{\varepsilon 2\pi L} \ln\left(\frac{b_c}{a_c}\right)$$

(5.1)

where ε is the dielectric permittivity, L is the length, and a_c and b_c are smaller and larger electrode radii. Ratio studies were current-controlled, allowing the $Q/2\pi\varepsilon$ coefficient term to remain constant. Fig. 5.2 shows linearity of electrode voltage relative to $\ln(b_c/a_c)/L$. Eq. 5.1 assumes an infinite parallel capacitor, such that the closest distance between electrodes is the same for any given point, which is not the case in the finite Cr electrode cell configuration.
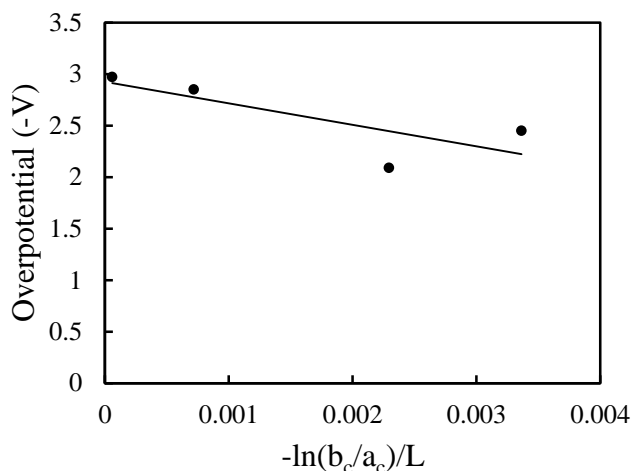
Figure 5.2: Electrode ratio Gaussian potential difference and measured potential

A high electrode ratio also increases the rate of Cr^{3+} oxidation by providing a higher quantity of oxidation catalysis active sites while maintaining the rate of partial reduction occurring at cathode. This is shown through increase in current efficiency with anode : cathode ratio (Table 4.15). Such oxidation side reactions also contribute to a more electropositive overpotential according to

$$E_{cell} = \Sigma\ E_{reduction} - \Sigma\ E_{oxidation}.$$

Radiocontaminants would be similarly affected by oxidation side reactions, so the decreased overpotential does not increase radiopurity. The increase in solution resistance with increase in Cr^{3+} concentration does lead to a higher voltage response, approaching that of radiocontaminants and increasing likelihood of their deposition. Therefore, a high anode : cathode ratio was chosen for Cr cells.

5.1.4 Cell Operation Parameters

Coordination chemistry between Cr and the sulfate ligand dictates a very specific concentration ratio of CrO_3 to SO_4 in Cr plating baths (§ 2.3.7.2). Acceptable concentration ratios of Cr to H_2O cover a much broader range, with increased

conductivity coming from greater H_2CrO_4 concentrations, instead of H_2SO_4 as with Cu electrolytes. Cr-electrolyte concentration studies show both covering power and deposit quality to be highest for 65.96 g_{Cr}/L (Fig. 4.17). CVs show increasing charge transfer with increasing concentration (Fig. 4.29); however, the deposition overpotential of this same 65.96 g_{Cr}/L bath is lower than for the other concentrations (Fig. 4.16). This behavior is also reflected for Cu reduction (Fig. 4.9), where the current peak continues to linearly increase with Cu concentration but the deposition potential decreases at an intermediate concentration before increasing again. This behavior is counter to the Nernst Equation (Eq. 2.24), where an increase in ion activity results in a decrease in reduction potential. The conductivity of Cu electrolytes used in the study were comparable; therefore, increasing solution resistance is not source of increasing potential. Linear behavior of Randles-Sevcik equation plots for Cu (Fig. 4.8), and at low scan rates for Cr (Fig. 4.28), indicate an ion-diffusion control mechanism. Plots of peak position for Cu (Fig. 4.9) and Cr (Fig. 4.29) at varying ion concentrations show that ion diffusion continues to linearly increase with concentration, as expected for a mass-transport limited system.

The Levich plot for Cu (Fig. 4.7a) confirms diffusion control. A liner plot of the associated limiting current dependence on concentration (Fig. 4.7b) shows a decrease in boundary layer thickness with increase Cu concentration, according to Eq. 2.23. Similar results could not be determined for Cr, for which study state was not achieved in RDE studies (Fig. 4.27) using extreme electrode rotation and scan rate values.

With the overall goal of minimizing radiocontamination co-deposition, cell parameters are investigated with the aim to lower the metal ion of interest (Cu and Cr)

overpotential without reducing the reduction potentials for the entire system. Most aspects discussed thus far addressed increases in the overpotential above the reduction potential, because of cell conditions. The Nernst Equation (Eq. 2.24) shows variables affecting reduction potential are metal ion activities and temperature. Analytical investigations into effect of Cr electrolyte temperature (Fig. 4.31) show a decrease in peak current and exponential increase in peak potential with increase in temperature. Hull cell cathodes at various temperatures (Fig. 4.18) show a decrease in minimum current density (Fig. 4.19) required to deposit Cr with a decrease in T. Thermodynamically a decrease in T will increase the reduction potential. The standard half-cell potentials of ions are also changed with T[80]: 0.557 mV/K for Th and 0.16 mV/K for U. At the very low relative concentrations of U, Th in the electrolyte solution (Table 4.31), the Nernstian increase in reduction potential is much lower than the increase for Cu and Cr with the same change in T. A higher deposit radiopurity is, therefore, still a result of lowered T from lowered overpotential and minimized required current density.

Fig. 5.3 shows Cu and Cr reduction potentials for all activities possible in the developed plating cells. Cr will not reduce under a certain activity and Cu will reduce well below concentrations considered here; those concentrations are plotted as low Cu. As seen from this plot, the potentials of U and Th (Table 2.2) are far greater than Cu or Cr for any concentrations considered, and thermodynamically there is not a basis for their reduction under plating conditions herein. Assay results of Cr shown in Table 4.30, however, show quantities of U and Th in electrorefined deposits. Hoppe hypothesized[9] (§ 2.3) that excess (over Nernstian theory) U, Th measured in EFCu deposits were a

result of mass transfer effects. It was of interest in this study, therefore, to minimize

both potential and current density. Potential and current relations for all investigated cell

parameters are shown in CV and RDE analytical study plots (§ 4.1, 4.2.5).
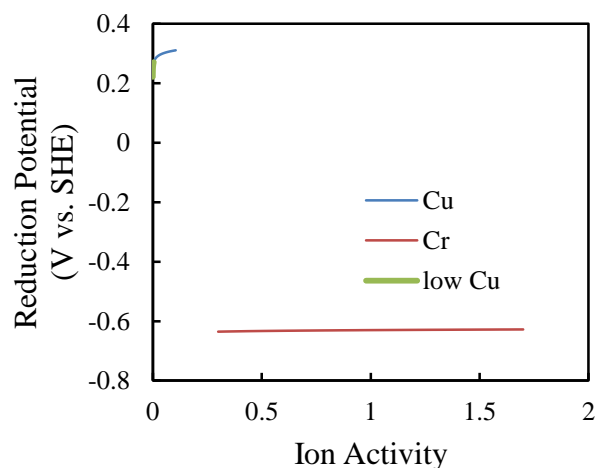
Figure 5.3: Nernst Eq. Cu and Cr reduction potentials

Examination of additive-free Cu deposits at varied temperature leaves no doubt in

temperature range which may be employed (Fig. 4.1). The presences of dendrites

resulting from temperature gradients were overwhelming at high T. At low T fine

dendrites of an entirely different structure were present. These are resultant of decreased

aquated ion mobility, shown by extreme reduction of current (Table 4.5). The reduced

current density provides lower initial nucleation coverage as shown in Eq. 2.44 where

the relationship between η and i is given by the Tafel equation (Eq. 2.18) and measured

constants in Table 4.10. Island growth results from low coverage, giving rise to thin

dendrites. There is little correlation between Cu deposition peak potential and

temperature (Fig. 4.11), providing no purity motivation for perturbing electrolyte

temperature.

Stir rate was the most important variable in reducing Cr on deposited Cu. Cr studies involving rolled Cu, which has negligible surface roughness, exhibited no difficulties plating without solution perturbation (Fig. 4.20). Ability to reduce Cr was examined at different stir rates on Cu cathodes plated in Runs 7 and 10, with roughness's listed in Table 4.7. The voltage response during current-controlled Cr plating on these cathodes is shown in Fig. 4.38. Cu Run 10, which possessed roughness significantly less than that of Run 7, has a periodically oscillating waveform at 0 RPM . Examination of Cr deposits on Cu Run 10 show very poor covering power and large field effects (ie. differences in current density between high and low surface features). No deposition occurred on rougher Run 7 cathodes at stir rates much greater or less than intermediate rate 525 RPM. The voltage response at lower stir rates oscillated at high frequency, and at higher rates leveled off to the hydrogen reduction potential. Cr analytical examinations show suppressed current for all stir rates outside of an intermediate (Fig. 4.30). In the analytical case the stir rate is 350 RPM; however, that employed a 1 cm^2 flat SS disk cathode. The increased peak current indicates a diversion from pure diffusion control and an increase in diffusion coefficient derived for the system (Fig. 4.28) for CV scan rate studies.

At low stir rates, Cu CV studies show little correlation between deposition potential or peak current with stir rate (Fig. 4.10). RDE studies show an increase in limiting current with rotation rate (Fig. 4.7). This indicates that the Cu system at low stir rates is not at study state and that pure diffusion control behavior is not exhibited in CV studies. The limiting current increases with perturbation (Fig. 4.7), raising current and lowering deposition potential as shown in Fig. 4.10. Table 4.3 shows improvement in

deposit quality with stir rate up to a point. The structure is a result of increasing

difference between applied current and limiting current with flow rate (Fig. 4.7).

5.2 Physical Metallurgy Discussion

5.2.1 Cu-Cr Hardness

The Cu-Cr alloy hardness increase over pure EFCu is shown in Fig. 5.4. The alloy is vastly harder than PNNL EFCu produced for radioassay detectors; however, similar in hardness to parent EFCu samples used in this study. Fig. 4.61a shows that the hardness of non-HT parent samples are (1) much greater than that of PNNL EFCu listed in Table 4.26 and (2) spread over a very wide hardness range of 80 to 180 HV. The PNNL EFCu hardness standard deviation is shown as only 7.5 HV. Fig. 4.61b shows that EFCu hardness post-solution treatment levels off to a constant value, independent of electrolytic Cu starting hardness. The EFCu-Cr hardness increase achieved during precipitation alloying is, therefore, from this baseline and not the starting Cu hardness.
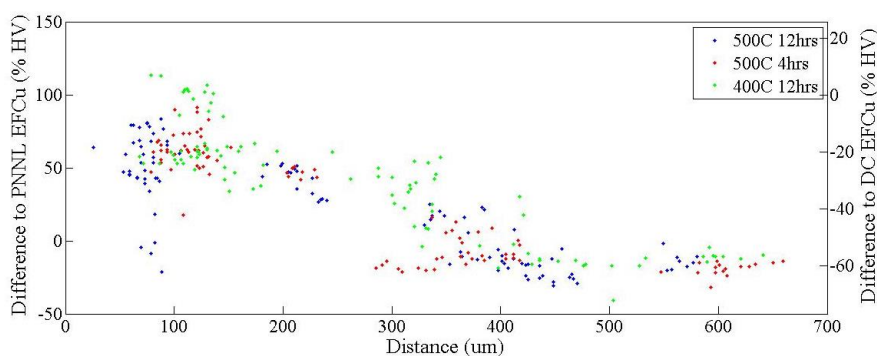
Figure 5.4: Hardness differences relative to Majorana EFCu average hardness and used parent sample hardness

The process with which Cu samples for this study (DC EFCu) were produced is with direct current, whereas PNNL EFCu uses a reverse-pulse waveform. The current density depositing DC EFCu is > 0.006 A/cm^2, and the current producing PNNL EFCu is ~ 0.001 A/cm^2. Fig. 4.6 shows the dramatic decrease in Cu hardness at lower current densities.

Pulse-plating (PP), employed at low frequencies in PNNL EFCu to increase radiopurity, was studied up to 1000 Hz (§ 3.1.2). As shown in Table 4.7, the roughness of resulting deposits is greatly reduced from that of DC Cu plated at the same current density. The hardness of high frequency deposits is lower than that of similar current density samples even when the grain size is larger (Table 4.8). Fig. 4.6 shows change in hardness with j for both DC and PP samples. As aforementioned the hardness in DC Cu increases with j, but that of PP Cu increases and then decreases again with j (Fig. 4.6a). Current response during PP runs (Fig. 4.2) shows that at frequencies over 10 Hz the waveform no longer relaxes to 0 A during duty-cycle off-time. This is the same point at which hardness goes from decreasing to again increasing (Fig. 4.6b). It is reasonable to assume the hardness would have continued to decrease with increasing frequency had the current dropped to 0 A during duty cycle off-time, allowing the matrix to relax and reducing residual deposit stress. The PP Cu hardness increase is not a strong function of grain size, which is being refined by increasing frequency. This can be seen in plot of grain size increasing during which hardness both decreases and increases (Fig. 4.6a).

Table 4.7 shows the increase in surface roughness with increased current density. Surface roughness is a function of grain size (Table 4.8). Increased current density decreases critical nucleus size (Eq. 2.44) increasing the surface coverage and producing larger grains. The DC EFCu samples were plated for less than a week apiece, while EFCu for detector projects plate for ~11 months to achieve desired thickness. The resulting surface morphology at the high current densities would be uncontrollable. More importantly, the mass transport increase with current density would also result in unacceptable purity levels (discussed further in § 5.3).

Current and potential waveforms were investigated as means of lowering Cu surface roughness (§ 3.1.3). Cu nucleated at high initial j followed by bulk deposition at low j possessed the low surface roughness of the bulk deposition j. In addition, deposits spiked for 5 min (Table 3.4) produced fewer dendrites than DC EFCu deposited at the same lower j (Table 4.1), and deposits spiked for 10 min produced no dendrites. This is a result of increased initial surface coverage preventing island growth. The increase in probability of radioimpurity inclusion during the initial η (at which E is still far lower than $E_{U, Th}$) and j spike is counteracted by the allowed decrease in the same during the much longer bulk plating period.

5.2.2 Intermediate Strain Hardening

Strain hardening Cu-Cr alloys between solution treatment and age hardening is used to increase strain and defect concentration, lowering precipitate nucleation energy barrier (Eq. 2.53) and increasing concentration of energetically feasible nucleation sites. This results in a higher concentration of precipitates forming at lower energy, which grow and coarsen more rapidly (Eq. 2.58). Alloy aging curves for CW samples show the maximum hardness for all conditions to be greater than that of non-CW samples (Fig. 4.63), as is expected. Table 5.1 shows the percent increase in hardness with cold rolling for the three hardest aging conditions. Compared to the percent CW of these samples listed in Table 5.2, this increase is insufficient to make up for the cross-sectional reduction. Fig. 5.5 shows hardness curves for prime aged CW samples before and after aging. There is very slight hardness increase in areas of maximum Cr content.

Table 5.1: Percent increase in hardness with intermittent cold rolling

T (^{o}C)	T (hrs)	CW (% HV)
500	12	8.91
500	4	11.97
400	12	28.40

Table 5.2: Percent cold work for Cu-Cr alloy samples

Sample	HT		% CW
	T (^{o}C)	t (hrs)	
5.14Mar	400	4	13.45
	400	12	
	500	12	
4.2Mar	500	4	40.49
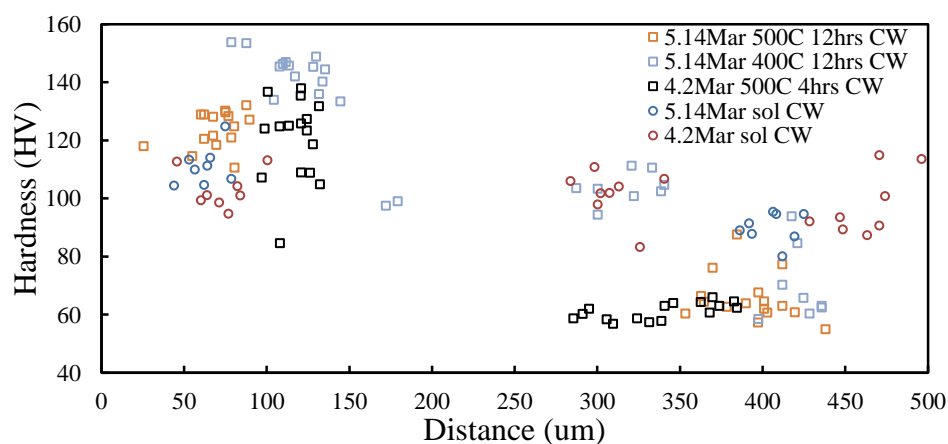
Figure 5.5: Vickers hardness of CW Cu-Cr samples before and after aging

A TEM examination of CW sample 600 ^{o}C 4 hrs shows precipitate growth mainly on grain boundaries (Fig. 4.54b). These precipitates range from 10 to 200 nm in diameter, whereas the same HT non-CW sample only exhibited precipitates up to 45.6 nm (Table 4.24). Because of the situation of precipitates on GB, the average spacing is much less than the average precipitate diameter. An examination of CW sample TEM images of the in Fig. 5.6a shows a high dislocation strain concentration. There is little

coherency strain however seen around the spherical precipitates shown in Fig. 5.6b. Non-CW aged samples show such high precipitate coherency strain that the precipitates cannot be imaged under diffraction contrast (Fig. 5.6b). Non-CW alloy precipitates also exhibit an increasingly needle-like shape with increasing aging extent (Fig. 4.54a, c, d), which is expected for KS-oriented overaged precipitates in Cu (§ 2.4.3). CW sample precipitates are spherical despite their large size (Fig. 4.54) and are off-axis from the matrix (Fig. 4.58) indicating entire incoherency. The sample, therefore, lacks deformable precipitate coherency strengthening and is only strengthened through dislocation looping mechanisms (§ 2.2.2). This is seen in a high resolution SEM image of the CW TEM sample (Fig. 4.52), where Cr is selectively clustered in large loops. These are not grains as can be seen from the etched sample, indicating they are dislocation loops. Non-CW Cu-Cr samples utilize a combination of misfit and Orowan looping strengthening mechanisms. SAD diffraction patterns identified Cr precipitates as BCC (Fig. 4.59), so neither CW nor non-CW Cu-Cr benefit from chemical strengthening. There is, therefore, a lower increase in strain rate over unalloyed EFCu-Cr resulting from an intermediately CW EFCu-Cr alloy than resulting from alloying without strain hardening.

(a) (b)
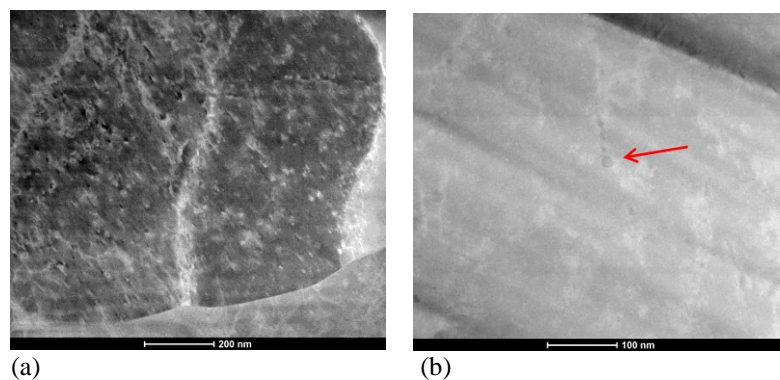
Figure 5.6: TEM image of CW sample aged at 600 $^{\circ}$C 4 hrs (a) high dislocation strain concentration (b) low precipitate strain

Produced alloy purity is the main concern when adding materials process steps, such as cold rolling. The CW material would have to be skim cut on each surface post-processing, further reducing cross-sectional area and negating the small increase in hardness over non-CW Cu-Cr alloys.

5.2.3 Peak Aging

Fig. 4.63 shows aging curves of CW and non-CW Cu-Cr samples for all investigated T and t. Peak hardness of non-CW Cu-Cr occurs at 500 $^{\circ}$C 4 hrs and for CW is 400 $^{\circ}$C 12 hrs. The hardness difference between 500 $^{\circ}$C 4 hrs and 12 hrs was within error limits for non-CW samples, with 500 $^{\circ}$C 4 hrs being slightly higher than 500 $^{\circ}$C 12 hrs for CW samples. Table 5.1 shows CW percent reduction for samples used in each of these tests. The Cu-Cr CW sample used in 400 $^{\circ}$C 12 hrs has lower reduction than that used for 500 $^{\circ}$C 4 hrs. The grain size for these samples is shown in Table 4.28 as being G = 0.5 for 500 $^{\circ}$C 4 hrs CW and G = 8.6 for 400 $^{\circ}$C 12 hrs CW. These factors indicate that the greater hardness in the 500 $^{\circ}$C sample over the 400 $^{\circ}$C sample is not a result of CW residual strain or GB strengthening from CW grain refining. As discussed in § 5.2.2, precipitates will mature sooner in strain hardened samples. This indicates peak aging conditions for strain hardened electrolytic Cu-Cr is 400 $^{\circ}$C 12 hrs and peak aging without intermediate processing occurs at 500 $^{\circ}$C 12 hrs.

Fig. 4.62 shows hardness curves for the hardest non-CW aging conditions. Fig. 5.7 shows partial delamination at Cu-Cr interface prior to solution treating resulting in the low harnesses plotted near the interface in Fig. 4.62. The stress required for a dislocation to pass precipitates is inversely related to the distance between particles (Eq. 2.8). Peak

aging occurs at the point of maximum dislocation flow stress, which is discussed further in § 5.2.4. The measured precipitate sizes and spacing are listed in Table 4.24. The precipitate spacing for 500 ^{o}C 12 hrs is less than the other examined HTs with lower hardness, indicating that the other HTs are over-aged. Hardness results for 400 ^{o}C 12 hrs are similar to 500 ^{o}C 12 hrs, although no precipitates could be verified in prepared TEM sample (Fig. 4.55b).
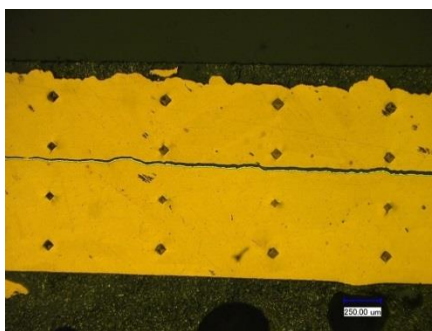
Figure 5.7: Indents near delaminated section of interface

5.2.4 TEM Characterization

The stress concentrations in TEM examined samples were very high, effectively hiding precipitates that would otherwise be identified by their strain fields under diffraction contrast. In each sample there were numerous features that appeared to possess coffee-bean contrast, which generally identifies them as coherent precipitates (Fig. 4.56a, c). The EDX scans of these areas showed no distinction between Cu matrix level Cr concentrations and features, which could be explained by the signal from relatively small features attenuated by the Cu matrix. Upon veering off-axis to pure atomic number (Z)-contrast, these features are suppressed and actual Cr precipitates emerge. The spectra of precipitates of the same diameter as the features exhibit large, distinct Cr peaks (Fig. 4.56b, d).

The manner by which the Cr precipitates must be imaged in TEM prevents typical strain field, coherency, and SAD analysis. SAD patterns were taken on larger precipitates found on CW and 500 °C 12 hrs samples (Fig. 4.58-4.60), as well as the adjacent Cu matrix. Calculated misfit from measured lattice spacing show an 11% higher misfit than literature.

Large peak aged Cr precipitates, as shown in Fig. 4.58 and Fig. 4.59, are oriented on different zone axis than the Cu matrix and are BCC. These are, therefore, non-shearable precipitates as discussed in § 2.2.2. Flow stress for non-shearable particles is given by Eq. 2.8. The Burger's vector is calculated from the Cu lattice constant of sample 500 °C 12 hrs (Table 4.25) shown on [110] zone axis SAD image (Fig. 4.60). According to Eq. 2.2,

$$b = \frac{a\sqrt{2}}{2} = 262.87 \ pm.$$

For shear modulus µ=48 Gpa[81], and average precipitate spacing r and precipitate diameter d listed in Table 4.24, the flow stress τ is

$$\tau = \frac{0.034}{r}\ln\left(\frac{d}{1.05}\right).$$

Values for each non-CW TEM sample in which precipitates were verified are calculated and listed in Table 5.3, as they compare to measured hardness.

Table 5.3: Calculated flow stress and measured hardness for alloyed Cu-Cr samples

Sample (°C/hrs)	Spacing (nm)	Diameter (nm)	Stress (Gpa)	Max Hardness (HV)
500/12	12.15	13.03	0.337	121.22
600/12	148.29	84.86	0.048	89.74
600/4	19.12	23.08	0.263	96.78

Lattice constants for smaller precipitates with high coherency stain could not be measured, since the off-axis means of imaging them prevents SAD pattern imaging. Their coherency could also not be determined, but should they be coherent their lattice constant would be different than that of the large incoherent particle measured. Therefore, the deformable particle stress contribution cannot be accurately calculated using Eq. 2.7.

5.2.5 Maximum Alloy Hardness

The maximum hardness achieved in non-CW EFCu-Cr alloy samples solution treated at 1000 ^{o}C is 121.39 HV. This is comparable to the maximum hardness reported for Cu-Cr alloys investigated by Proca (Table 2.4) using similar wt% Cr. Other methods listed in Table 2.4 use strain hardening, grain refining, or excessive Cr concentrations (up to 15 wt%) to increase hardness.

This peak hardness does not represent the upper limit for potential EFCu-Cr alloy hardness. Solution treating with a 0.78 % increase in temperature resulted in a 14.16 % increase in hardness under identical peak aging conditions (§3.4.3). The increase is a result of increase in Cr solubility at higher T as shown by the phase diagram (Fig. 2.5).

Solution treatment studies to cover a wider range of T and t were initially employed in an Ar purged atmosphere on electroplated Cu-Cr samples removed from their SS cathodes (§ 3.4.2). Resulting micrographs and SEM images with EDX overlay (Fig. 4.42, 4.43) showed a Cr-oxide band on either side of the Cr layer. This indicated that (1) the Cr had diffused at least that far (Fig. 4.44) during the solution treatment and (2) there was O_2 resulting from either sample fabrication or furnace atmosphere. A

further sample was solution treated under the same conditions, but with the deposit remaining around the SS cathode. This sample exhibited the circumferential oxide band only on the outer side of the Cr band as shown in Fig. 5.8, indicating O_2 in the furnace atmosphere (§ 2.4.4). H_2 was added to the furnace atmosphere to reduce any residual O_2 and the problem was not again observed.
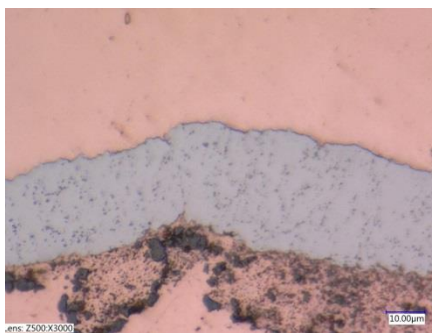
Figure 5.8: Cr band in solution treated Cu-Cr sample with oxidation on atmosphere-exposed side

5.2.6 Determination of Alloy Composition

Vickers hardness of alloyed EFCu-Cr plotted against distance from Cu-Cr interface shows distinct curves which slope down to level out at the solution treating hardness (Fig. 4.62). The hardness increase is not from Hall-Petch GB strengthening, as is shown by independence of grain size on hardness of alloyed samples (Fig. 4.64). The hardness curves show dependence on concentration of Cr alloying element present, and the amplitude of the curve shows aging stage.

Determination of Cr concentration alloyed in this study is significant. TEM samples were much too thick (necessitated from FIB curtaining) to determine either thickness using typical approaches or actual concentration of precipitates per volume. Using TEM EDX area scans showed 0 wt% Cr, because of attenuation from Cu matrix

with Z-value higher than that of Cr. Unlike other alloying studies, the concentration of alloying element is not dispersed evenly throughout the matrix and simple weight ratios are not definitive. SEM/EDX Cr concentration results (Fig. 4.53) are inconsistent as shown in Fig. 5.9. Inconsistencies are most likely a result of interaction volume, small alloyed volume, and low Cr signal relative to that of the surrounding Cu matrix.

(a)   (b)
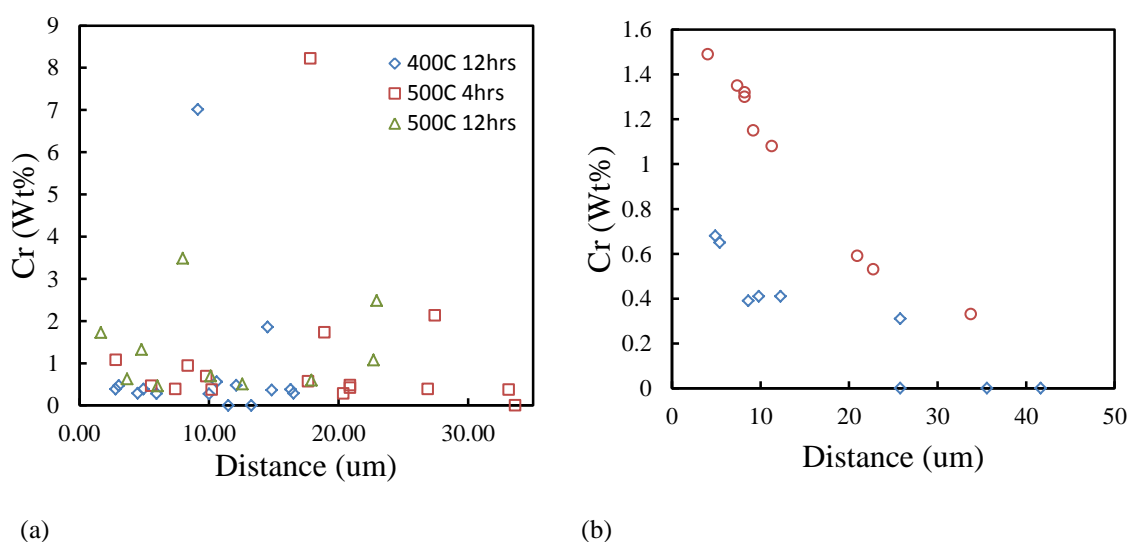
Figure 5.9: (a) Point and analyze EDX spectra on high-contrast features in Cu matrix, shown in distance from Cu-Cr interface (b) Point and analyze EDX spectra in two lines on same sample

Cu-Cr alloy hardness curves are used to determine Cr concentration at any given point in the alloy. A linear relationship between peak aging hardness and Cr wt% in Cu-Cr alloy is assumed. This assumption takes into account negligible grain boundary stress contribution as previously discussed, negligible residual stress from plating after solution treatment recrystallization, and over-saturated Cr concentration fully precipitated from Cu matrix. This last assumption indicates that underaged samples' hardness curves cannot be used to calculate Cr wt%, but that the developed relationship between hardness and Cr concentration applies to them.

In § 4.4.2 it was discussed that reduction of plated Cr band thickness throughout HT represents a means of determining Cr quantity introduced into Cu matrix (Fig. 4.49). The validity of this approach is verified by plot of band thickness at periodic solution treatment soak time increments (Fig. 4.50). The measured Cr band width reduction represents the percentage of known plated Cr grams which has dissolved into the Cu. The dissolved Cr quantity was calculated for each individual HT sample.

The diffusion of Cr into Cu is assumed to be negligible during aging, since Cu matrices are supersaturated with Cr from solution treating and aging T is kept below the solubility limit. Any diffusion occurring during aging is from Cr already in solution, to growing precipitates. This assumption does not apply to sample aged at 800 ^{o}C as seen in TEM analysis of sample 800 ^{o}C 4 hrs (Fig. 4.55a). Cr concentration in the Cu matrix was orders of magnitude higher than concentrations in all other samples (observed in SEM/EDX for this sample as well). Nanometer size loosely grouped Cr clusters were seen, indicating this sample was aged on the boundary of Cr solubility.

The sixth-order polynomial curve *f(x)* shown in Fig. 5.10 is modeled to the aging hardness curve for sample 4.22Feb aged at 400 ^{o}C for 12 hrs. This curve is normalized to solution treatment hardness, the point of 0 wt% Cr where hardness has not increased though aging. The area under the curve is found taking the integral from the interface to the point at which there is no hardness increase over solution treatment values,

$$Area = \int_{0um}^{450um} f(x)\ dx. \tag{5.2}$$
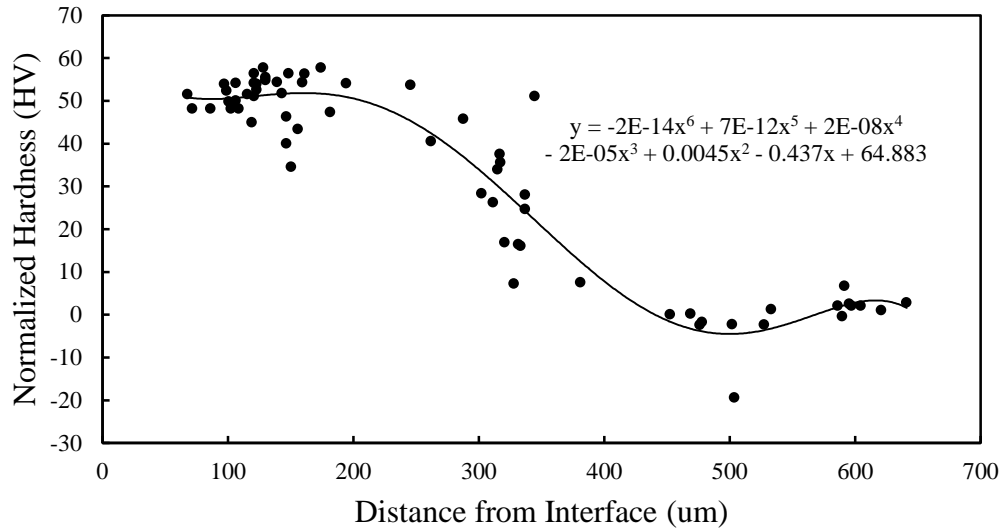
Figure 5.10: Polynomial fit on hardness curve for aging HT 400 °C 12 hrs

The curve represents relative concentrations of Cr present in the Cu. The actual concentration of Cr dissolved in the matrix is calculated over that cross-sectional surface area S_A,

$$C_{Cr} = \frac{Wt_{Cr,dissolved}}{2 \cdot S_{A,Cu}}$$
(5.3)

$$C_{Cu} = \frac{\rho_{Cu} * V_{Cu,450um}}{S_{A,Cu}}$$
(5.4)

where wt_{Cr} is the grams of Cr dissolved, $V_{Cu,450um}$ is the volume of plated Cu for a 450 um thickness, ρ_{Cu} is the density of Cu and C_{Cu} and C_{Cr} are concentrations of Cu and Cr in $\left(\frac{g}{um^2}\right)$. A factor of two in the Cr concentration term accounts for Cr migration bilaterally across the interface; both sides are tested for hardness and included in aging curves but the function only accounts for one side. The Cu concentration is calculated out to 450 um, which is the upper bound for the area integral and the distance at which the hardness

curve slopes to 0 HV. The numerical area solution was related to concentration by coefficient m,

$$Area \cdot m = \frac{C_{Cr}}{(C_{Cu}+C_{Cr})} \qquad (5.5)$$

The polynomial was solved for maximum Cr concentration next to the Cu-Cr interface, where distance x = 0 um,

$$HV(x = 0) \cdot m \cdot 100 = wt_{Cr,max}\%. \qquad (5.6)$$

Concentrations are thus further correlated linearly to hardness data (Fig. 5.11). Each additional sample uses the same integrated curve with their unique C_{Cr} and C_{Cu} values.
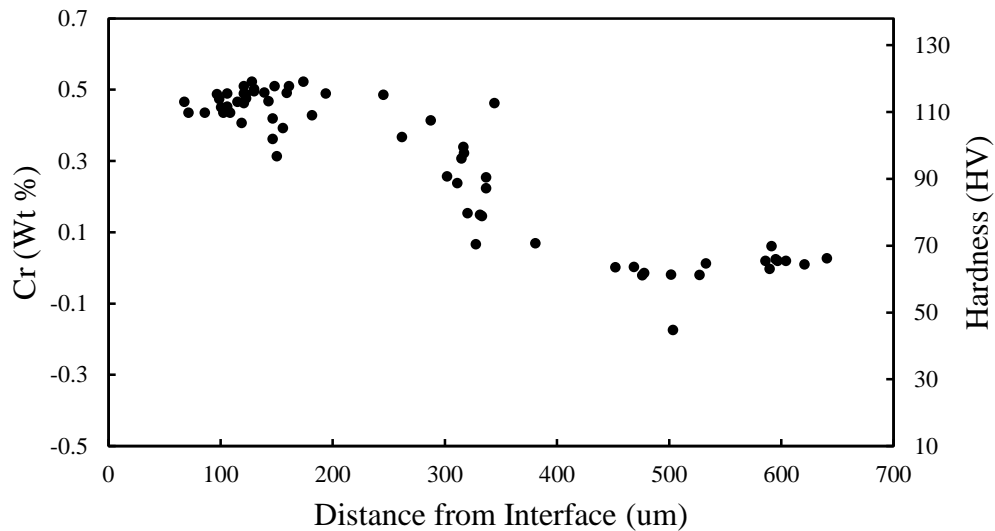
Figure 5.11: Alloyed Cu-Cr Cr concentration determination, relative to hardness

The resulting alloy is a maximum of 0.585 wt% Cr, a value consistent over all alloyed samples and in close agreeance with literature (§ 2.4). This is further modeled for Cr diffusion using Fick's Second Law as shown in in Fig. 5.12. The resulting diffusion coefficient is 8.9 x 10^{-9} cm^2/s. Comparing this value with those calculated in §

4.4.2 from EDX measurements on the same alloy (Fig. 4.46, 4.47) and literature values (Fig. 4.48) shows a much higher rate of diffusion. The previously calculated Cr diffusion coefficients using EDX Cr concentrations in EFCu-Cr only show diffusion in Cu to ~ 50 um, however strengthening effects are seen beyond 300 um. Literature values show insignificant concentrations at 150 um.
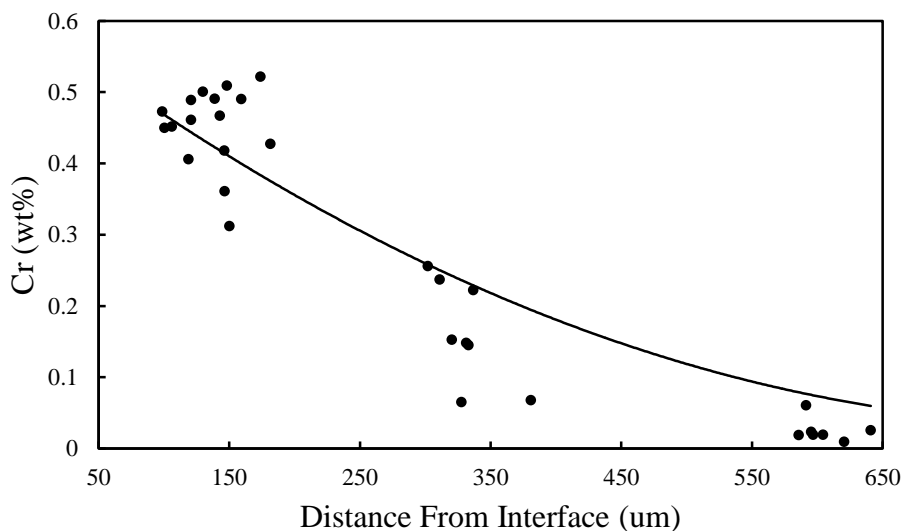
Figure 5.12: Cr diffusion coefficient calculation using hardness curve

The higher diffusion rate can be explained by two factors unique to electrolytic growth. First, Cr diffuses in the direction of Cu growth within aligned grains, as seen by etched Cu micrographs (Fig. 4.4). Cr diffusion is not impeded by grain boundaries as it would in other systems, such as in a cast Cu-Cr solution. Second, high Cu lattice strain from electrolytic growth and shown in TEM images (Fig. 4.56) results in a larger Cu lattice constant (Table 4.25) than found in literature. This lowers the energy Cr must overcome to diffuse along a plane.

5.3 Radiopurity

The preparation of Cr-baring samples for ICP-MS assay was entirely research and development. The levels of U and Th at which physics radioassay detectors are interested have only recently been successfully assayed. Only PNNL has hitherto developed processes to assay to these levels, and Cr was not a material they investigated or for which they developed methods.

5.3.1 Sample Screening

The first set of samples was greatly diluted for screening to determine general guidelines for the entirely unknown purity concentrations. Even at metal ion concentrations around 100 ppb the ICP-MS plasma cone was coated with Cr, destroying sensitivity and producing no useable results. All further samples could, therefore, not have similar concentrations of Cr ions present, indicating necessity of ion-exchange columns.

Dilution methods were again necessitated in § 3.7.4 because of the inability of columns to process several key samples. A dilution to ~1 ppb was used to prevent a repeat coating of the ICP-MS cone. This excessive dilution resulted in obtaining only upper limits on several source Cr samples and alloyed sample EFCu-Cr 2. As mentioned in § 5.1.3, important information is lost through the upper limits; however, what is seen is a much lower Th limit on the VIM Cr nugget than the actual value measured for the Cr chips from which the nugget was formed (Table 4.31). This does not automatically indicate the VIM process purifies Cr. The U, Th concentrations in the aluminothermic Cr is higher than the majority of unrefined materials assayed by PNNL[1]. The chips were

cleaned before assaying by rinsing with passivating HNO_3 to prevent entire dissolution, whereas the nugget was surface etched with HCl. Therefore, surface embedded contaminants could have remained in the chips.

Although Cr anodes are not suitable for use in Cr electrorefining (§ 5.1.3), high purity solid Cr may still be used as an ion addition source, should it be obtainable in higher radiopurity than possible for CrO_3. This is important in the case of a mass transport rejection rate based U, Th deposition mechanism. Although both Cr sources purchased are 99 % purity, the solid Cr is listed at 99.5 % Cr, and the CrO_3 is 99.8 % CrO_3. Only an upper limit was determined for CrO_3 as well, in the same region as the limit on VIM Cr (Table 4.31). No comparison of their radiopurities can, therefore, be made.

5.3.2 Rolled Cu Cathode Samples

The currently developed PNNL separation method for Cu, used to assay MJD EFCu, utilizes anion exchange resins. The Cu passes through while the resin retains the U and Th. After all Cu metal ion residue is rinsed from the resin, the U and Th are eluted and assayed. The effectiveness of this method is verified by radioisotope tracers which mirror the response of the U and Th isotopes of interest. The resin retains or releases ions in response to specific acids introduced, such that according to methods developed by PNNL all separated samples must be introduced in a 2% HNO_3 matrix.

Cr passivates in HNO_3 and dissolves in HCl (Eq. 2.45) so the matrix of Cr samples must be switched after dissolution. Since HCl has a lower boiling point than

HNO_3 this is done through successive boil-offs. Every sample preparation step only adds to the probability of contamination.

Initial Cr plated for ICP-MS analysis were plated onto rolled Cu cathodes. Although these were commercial and of unknown radiopurity, they were very flat with negligible roughness. Cr plated on rolled sheets retained their shape after dissolving the Cu, allowing Cr to be further cleaned and processed for assay. Cr plated on electroformed Cu followed the relatively rough surface morphology, and fell apart after dissolution of cathode. The remaining flakes could not be rinsed and retained; therefore, rolled Cu cathodes were used.

As seen from Table 4.29, the Cr radiopurity resulting from plated on rolled Cu was both high and covered a large range. This indicates contamination and inconsistency in methods.

5.3.3 EFCu-Cr Samples

It was of interest to both determine the EFCu-Cr alloy contamination derived from the Cr alone, and any added during deposition layering and heat treating. Three alloyed Cu-Cr samples were prepared for assay. Boil-off Ar and purified H_2 were used for aging heat treatment atmosphere, so there should be no added contamination after surface etching produced samples. The process of moving deposited samples in a dual Cu-Cr bath process between baths and possible electrolyte entrapment between layers are several areas of potential contamination.

TEM analyzed EFCu-Cr alloyed at 800 ^{o}C for 4 hrs showed sulfur deposits (Fig. 4.57). These clusters were concentrated on one side of the Cu-Cr interface and absent on

the other. The only significant source of S is the plating electrolyte. The Cu and Cr

electrolyte concentrations of sulfate are 1.45 M and 0.0109 M respectively. The

concentration of S identified by the TEM EDX detector is 1.93 wt%, indicating the

source is the Cu electrolyte. Cu has very poor adhesion (§ 2.3.8), allowing a gap between

plated Cr and subsequent Cu layer in which electrolyte can be inclused. There is no gap

allowing electrolyte enclosure between the Cu and Cr layer, which possess excellent

adhesion. The electrolyte contains all rejected U and Th so inclusions lower radiopurity.

Extent of Cu adhesion to Cr (§ 3.3.2) was investigated to reduce the

aforementioned potential contamination introduced between deposited alloy layers.

1. Each Cr surface finish (bright, frosty, and dark) was tested both with and without
   HNO_3 passivation. The surface finishes possess different sub-micron scale
   roughness features created by cracking and pitting from hydrogen adsorption (Fig.
   4.15) changing the surface energy, allowing different quantities of preferable
   nucleation sites and changing the critical nucleation size according to Eq. 2.44 (§
   2.3.8.2). Passivation prevents galvanic corrosion of Cr (§ 2.3.8.1) which pushes
   the plane of closest approach further from Cr surface.

2. Chemical etchants H_2SO_4 and HCl were also used change surface energy of the
   Cr layer (§ 2.3.8.4). HCl is a harsher Cr etchant and opens the surface bonds.
   H_2SO_4 removes the passivation layer which easily forms. This was evidenced by
   observed banding of subsequent Cu deposits from uneven cathodic impedance.

3. Increased current density was tested with and without Cr passivation. Increasing
   the overpotential reduces the critical nucleation size by $1/\eta^3$ (Eq. 2.44), increasing
   the surface coverage.

The presence of an interfacial gap was noticed in all surface and cell conditions (Table 4.19) with the exception of the 50% HCl etch on bright Cr.

Assayed alloyed samples EFCu-Cr 1 and 2 (Table 4.29), which represent pre- and post-HT Cu-Cr, were plated with DC current and ACS grade starting materials. The resulting sample levels of U, Th are very low compared to Cr plated on rolled Cu. Sample EFCu-Cr 1 represents the pre-HT sample and EFCu-Cr 2 the post-HT sample. Since there are lower levels of U, Th in the post-HT sample, it is safe to assume that significant extra contamination is not added in this step. The same parent sample was used for both alloyed samples, it contained 0.877 wt% Cr. Cu electroformed from Optima grade starting materials has been extensively characterized for radiopurity (§ 2.3.4), and it is reasonable to assume that there is a factor of at least 10 times the concentration of radioimpurities in ACS grade starting components. Using published U, Th concentrations in PNNL EFCu[1] as estimated Cu contribution in alloyed samples, Cr contribution is calculated. For 0.11 pg_{Th}/g_{Cu} and 0.17 pg_u/g_{Cu}, the concentration of electroplated Cr is 36.97 pg_{Th}/g_{Cr} and 3.45 pg_U/g_{Cr} for EFCu-Cr$_1$, and 14.67 pg_{Th}/g_{Cr} in EFCu-Cr$_2$.

Since both EFCu-Cr samples are from the parent sample, higher U, Th levels in the pre-HT sample indicate contamination in the pre-HT sample. This contamination is very small and can result from the extensive sample preparation process.

5.3.4 EFCu Foil Cathode Samples

The Cr assay results for samples plated on rolled Cu were much higher than that of EFCu-Cr. Although the Cu was dissolved and disregarded from Cr samples before

assaying, it could easily have contributed to heightened electrolyte U, Th concentrations. The EFCu-Cr samples as well were assayed with large relative quantities of EFCu, the U and Th contribution for which had to be estimated. The best way to cleanly assay the Cr without cathode contribution was determined to be use of EFCu foil, which had been previously assayed and was smooth and flat, allowing for removal of plated Cr.

Cr-on-EFCu foil samples Cr_1 and Cr_5 showed satisfactory low U, Th concentrations, however sample Cr_3 resulted in 702.53 pg_{Th}/g_{Cr} and 176.81 pg_U/g_{Cr}. The electrolyte contaminant concentrations for the three Cr baths (Table 4.31) are all similar at an average of 213 pg_{Th}/g_{Cr} and 160 pg_U/g_{Cr}. The electrolyte U, Th concentrations are considerably lower than those in the Cr_3 sample, showing that Cr_3 has not been refined.

Table 5.4 shows the half-cell potentials of U and Th. The Nernst Equation (Eq.2.22) at room temperature is calculated using average electrolyte U, Th concentrations (Table 4.31) with an activity coefficient of one for the very low concentrations of metal ion of interest. The reduction potentials become E_U = -1.82 V and E_{Th} = -1.96 V vs. SHE.

A look at the plotted potentials during Cr deposition for each sample (Fig. 4.66) shows a potential spike on bath Cr_3 while both Cr_1 and Cr_5 remain around –0.7 V vs. SHE. Fig. 5.13 shows this spike to dip down below -4 V, thermodynamically reducing any ion in solution for that period of time. Faraday's Law (Eq. 2.36) is used to calculate possible quantity of ions reduced at 0.051 A during the 1 sec in which E < -1.96 V. Table 5.4 shows calculated quantity expected, and quantity measured. The amount potentially plated during the short spike is so much greater than the actual amount

deposited, that the current efficiency of these radiocontaminants is $< 2 \times 10^{-5}$ %.

Kinetically a low CE is expected; U is a molten salt process, not typically plated from a

sulfate-based electrolyte.
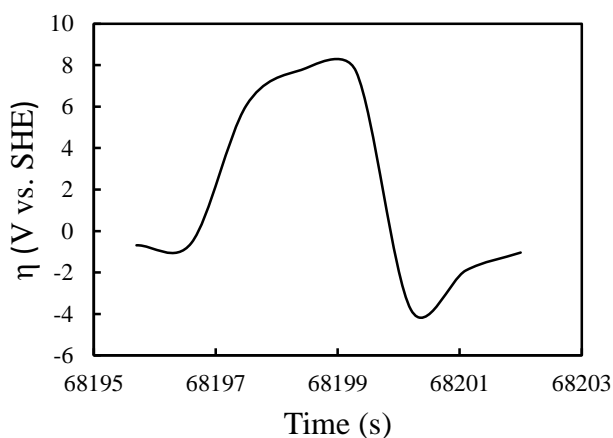
Figure 5.13: Voltage spike during Cr_3 ICP-MS run

Table 5.4: Cr_3 theoretical and measured U, Th

Radioisotope	E_o (V vs. SHE)	$Wt_{Faraday}$ (pg/Sample)	Wt_{meas} (pg/Sample)	CE (% $x10^{-05}$)
^{238}U	-1.642	62907593.77	2.9797	0.47
^{232}Th	-1.826	61324530.77	11.8396	1.93

5.3.5 Rejection Rate

The PNNL published rate of U, Th rejection in EFCu is 885[9]. That rate

considers a reverse pulse waveform, a current density of ~0.001 A/cm^2, and a bias

voltage of 0.32 V. All of these factors are designed for minimizing contamination. The

EFCu rejection rate is independent of radioimpurity concentration within the range tested

and comparable for both U and Th. As previously mentioned, at the low overpotentials

utilized in Cu and Cr electroforming there should thermodynamically be no U, Th co-

deposition. Their proposed solution is mass transport effects resulting in desired metal ions dragging the contaminants along with them as they travel to the interface.

Higher deposited U, Th quantities than thermodynamically predicted could also be a result of the extremely low activities at which U, Th are present in solution. The Nernst Equation was empirically modeled for 1 M quantities of each ion, and has never been examined at the quantities in which this study has interest. The Nernst model likely breaks down at extreme limits, although analytical investigations are needed to confirm this.

The highest Cr rejection rate (RR) of U, Th achieved in this study (Table 4.32) is 20.82 Th and 98.76 U. These Cr samples are deposited at a potential bias 0.4 V closer to U, Th and a current density 20 times that of EFCu. The rejection rates are Cr_1 $RR_U = 2.8 * RR_{Th}$ and Cr_5 $RR_U = 4.6 * RR_{Th}$. This shows a greater RR for U in both cases indicating a non-Nernstian mechanism, since the reduction potential of U for both bath concentrations is 0.14 V more electropositive than that of Th. However, the ratio for the same current density is different. The concentration of U in the electrolyte is higher for each bath (Th:U ratios 1: 1.38 and 1:1.24), also indicating encapsulation and not co-deposition since higher activities thermodynamically reduce at lower potential. It's not likely the samples or the electrolytes were significantly contaminated to throw the ratios off, since the values are otherwise consistent.

6. CONCLUSIONS

A Cu-Cr electrolytic precipitation hardened alloy with 0.585 wt% Cr was developed using an additive-free dual $CuSO_4$, H_2CrO_4 electrolyte method. The extent of diffusion of Cr in EFCu with a 1000 ^{o}C 24 hr solution treatment is 300 um. The diffusion coefficient of Cr in EFCu alloys is modeled using measured hardness variation with distance from the Cu-Cr interface. The calculated Cr diffusion coefficient at 1000 ^{o}C is $D = 8.9 \times 10^{-9}$ cm^2/s, which is much higher than the literature value of 5.086×10^{-10} cm^2/s[59]. A maximum hardness of 121 HV was achieved with a 1000 ^{o}C 24 hr solution treatment followed by peak age hardening at 500 ^{o}C for 12 hrs. Intermediate strain hardening of the EFCu-Cr alloy does not produce significant strain rate increases in the alloy after precipitation hardening.

The achieved Cr radiopurity is 8.72 pg$_{Th}$/g$_{Cr}$ and 2.37 pg$_U$/g$_{Cr}$. For the developed 0.585 wt% Cr alloy, the Cr contributions are 0.051 pg$_{Th}$/g$_{Cr}$ and 0.014 pg$_U$/g$_{Cr}$. This combined with published EFCu[1] purity produces a Cu-Cr alloy with 0.062 pg$_{Th}$/g$_{Cr}$ and 0.031 pg$_U$/g$_{Cr}$. MJD experimental radiopurity limits for currently required mass of electroformed parts is 0.075 pg$_{Th}$/g$_{Cr}$ and 0.024 pg$_U$/g$_{Cr}$. The rejection rates for electrolytic Cr are 21 for Th and 95 for U; therefore, slightly increasing the source Cr radiopurity greatly increases the produced alloy radiopurity.

The developed radiopure Cu-Cr alloy electrodeposition method is practical on an experimental scale, and future research will need to be done on increasing to production scale. The use of high grade starting material will result in lower concentrations of U and Th in Cr deposits, for both Nernstian and mass transport radiocontaminant deposition

mechanisms; therefore, a radiopure EFCu-Cr alloy which satisfies MJD experiment requirements is feasible. The produced alloy's increased strength will allow experiments to design lower mass parts use for specialty applications, reducing the overall mass U and Th contributions.

Bibliography

1.   N. Abgrall, I.J.Arnquist, F.T. Avignone III, H.O. Back, A.S. Barabash, F.E. Bertrand, M. Boswell, A.W.Bradley, V. Brudanin, M. Busch, M. Buuck, D. Byram, A.S. Caldwell, Y.-D. Chan, C.D. Christofferson, P.-H. Chu, C. Cuesta, J.A. Detwiler, J.A. Dunmore, Y. Efremenko, H. Ejiri, S.R. Ellior, P.Finnerty, A. Galindo-Uribarri, V.M. Gehman, T. Gilliss, G.K. Gioanetti, J. Goett, M.P. Green, J. Gruszko, I.S. Guinn, V.E. Guiseppe, R. Henning, E.W. Hoppe, S. Howard, M.A. Howe, B.R. Jasinski, R.A. Johnson, K.J. Keeter, M.F. Kidd, O. Kochetov, S.I. Konovalov, R.T. Kouzes, B.D. LaFerriere, J. Leon, J.C. Loach, J. MacMullin, S. MacMullin, R.D. Marin, R. Massarczyk, S. Meijer, S. Mertens, M.L. Miller, J.L. Orrell, C. O'Shaughnessy, N.R. Overman, A.W.P. Poon, K. Pushkin, D.C. Radford, J. Rager, K. Rielage, R.G.H. Roberson, E. Romero-Romero, M.C. Ronquest, A.G. Schubert, B. Shanks, M. Shirchenko, K.J. Snavely, N. Snyder, D. Steele, A.M. Suriano, D. Tedeschi, J.E. Trimble, R.L. Varner, S. Vasilyev, K. Vetter, K. Vorren, B.R. White, J.F. Wilkerson, C. Wiseman, W. Xu, E. Yakushev, C.-H. Yu, V. Yumatov, I. Zhitnikov and *Nuclear Instruments and Methods in Physics Research A* 2016, vol. 828, p. 14.

2.   K. L. Lee, C. K. Hu and K. N. Tu, *Journal of Applied Physics* 1995, vol. 78.

3.   T. Horita, Y. Xiong, K. Yamaji, N. Sakai and H. Yokokawa, *Journal of The Electrochemical Society* 2013, vol. 150, p. 5.

4.   N. Abgrall, E. Aguayo, F.T. Avignone III, A.S. Barabash, F.E. Bertrand, M. Boswell, V. Brudanin, M. Busch, A.S. Caldwell, Y.-D. Chan, C.D. Christofferson, S.R. Elliott, J. Esterline, J.E. Fast, P. Finnerty, F.M. Fraenkle,

V.E. Guiseppe, K. Gusev, A.L. Hallin, R. Hazama, A. Hegai, R. Henning, E.W. Hoppe, S. Howard, M.A. Howe, K.J. Keeter, M.F. Kidd, A. Knecht, O. Kochetov, S.I. Konovalov, R.T. Kouzes, B.D. LaFerriere, J. Leon, L.E. Leviner, J.C. Loach, P.N. Luke, S. MacMullin, R.D. Marin, S. Mertens, L. Mizouni, M. Nomachi, J.L. Orrell, C. O'Shaughnessy, N.R. Overman, D. Phillips, A.W.P. Poon, K. Pushkin, D.C. Radford, K. Rielage, R.G.H. Robertson, M.C. Ronquest, A.G. Schubert, B. Shanks, T. Shima, M. Shirchenko, K.J. Snavely, N. Snyder, D. Steele, J. Strain, A.M. Suriano, J. Thompson, V. Timkin, W. Tornow, R.L. Varner, S. Vasilyev, K. Vetter, K. Vorren, B.R. White, J.F. Wilkerson, T. Williams, W. Xu, E.Yakushev, A.R. Young, C.-H. Yu and V. Yumatov, *Advances in High Energy Physics* 2014, vol. 2014, p. 18.

5.   Felix Boehm and Petr Vogel: *Physics of Massive Neutrinos*. (Cambridge University Press, 1992).

6.   E. W. Hoppe, A. Seifert, C.E. Aalseth, P.P. Bachelor, A.R. Day, D.J. Edwards, T.W. Hossbach, K.E. Litke, J.I. McIntyre, H.S. Miley, S.M. Schulte, J.E. Smart and G.A. Warren, *Nuclear instruments & methods in Physic Research* 2007, vol. 579, p. 21.

7.   D.G.Phillips II, E. Aguayo, F.T. Avignone III, H.O. Back, A.S. Farabash, M. Bergevin, F.E. Bertrand, M. Boswell, V. Brudanin, M. Busch, Y.-D. Chan, C.D. Christofferson, J.I. Collar, D.C. Combs, R.J. Cooper, J.A. Detwiler, P.J. Doe, Y. Efermenko, V. Egorov, H. Ejiri, S.R. Elliott, J. Esterline, J.E. Fast, N. Fields, P. Finnerty, F.M. Fraenkle, V.M. Gehman, G.K. Giovnetti, M.P. Green, V.E. Guiseppe, K. Gusey, A.L. Hallin, R. Hazama, R. Henning, A. Hime, E.W.

Hoppe, M. Horton, S. Howard, M.A. Howe, R.A. Johnson, K.J. Keeter, C. Keller, M.F. Kidd, A. Knecht, O. Kochetov, S.I. Konovalov, R.T. Kouzes, B. LaFerriere, B.H. LaRoque, J. Leon, L.E. Leviner, J.C. Loach, S. MacMullin, M. G. Marino, R. D. Martin, D.-M. Mei, J. Merriman, M.L. Miller, L. Mizouni, M. Nomachi, J.L. Orrell, V. Yumatov and C. Zhang, *Journal of Physics: Conference Series*, vol. 381.

8. C.E. Aalseth, R.L Brodzinski, O.T. Farmer, E.W.Hoppe, T.W. Hossbach and H.S. Miley, *PNNL-SA-45365*.

9. E.W.Hoppe, C.E.Aalseth, R. Brodzinski, A.R. Day, O.T. Farmer, T.W. Hossbach, J.I. McIntyre, H.S. Miley, E.E. Mintzer, A. Seifert, J.E. Smart and G.A. Warren, *J Radioanal Nucl Chem* 2008, vol. 277, p. 7.

10. H.S. Miley, C.E. Aalseth, A.R. Day, O.T. Farmer, J.E. Fast, E.W. Hoppe, T.W. Hossbach, K.E. Litke, J.I. McIntyre, E.A. Miller, A. Seifert and G.A. Warren, *Environmental Radiochemical Analysis III* 2007.

11. K. Graham, In *APS Division Nuclear Physics*, (Hawaii, 2014).

12. Laura Segui and SNO+ Collaboration, *Nuclear and Particle Physics Proceedings* 2016, vol. 273–275, p. 2.

13. E. Previtali, *Nuclear Instruments and Methods in Physics Research Section A* 2013, vol. 718, p. 2.

14. E.W. Hoppe, C.E. Aalseth, O.T. Farmer, T.W. Hossbach, M. Liezers, H.S. Miley, N.R. Overman and J.H. Reeves, *Nuclear Instruments and Methods in Physics Research A* 2014, vol. 764, p. 5.

15.   R. Abbaschian, L. Abbaschian and R.E. Reed-Hill: *Physical Metallurgy Principles*. Fourth Edition ed. (Cengage Learning 2009).

16.   W.D. Callister Jr and D.G. Rethwisch: *Materials Science and Engineering an Introduction*. Eighth Edition ed. (John Wiley & Sons, Inc, 2010).

17.   NR Overman, C.T. Overman, T.A. Kafentzis, D.J. Edwards and E.W. Hoppe, *PNNL-21315* 2012.

18.   N. R. Overman, D. L. Neal, A.M. Jensen, C.T. Overman and E.W. Hoppe, *PNNL-24319* 2015.

19.   H. Deutchman, *The Ohio State University* 2013.

20.   W. Gan, *The Ohio State University* 2015.

21.   R. E. Smallman and A. H. Ngan: *Physical Metallurgy and Advanced Materials* Seventh Edition ed. (Elsevier, 2007).

22.   B. Kokuoz: *The Role of Crystallographic Relationships Between Alpha and Beta Phases on the Elevated Temperature Isothermal Phase Transformation Kinetics in TIMETAL LCB (titanium-6.5molybdenum-4.5iron-1.5aluminum)*. (Proquest, UMI Dissertation Publishing 2012).

23.   A. Chbihi, X. Sauvage and D. Blavette, *Acta Mater* 2012, vol. 60, p. 10.

24.   *Elements of Metallurgy and Engineering Alloys*. (ASM International, 2008).

25.   C. Brice, *The Ohio State University* 2000.

26.   A.C. Reardon: *Metallurgy for the Non-Metallurgist*. Second Edition ed. (ASM International 2011).

27.   S. Krishna, N. K. Gangwar, A. K. Jha and Bhanu Pant, *Journal of Materials* 2013, p. 6.

28.   J.A. McGeough, M.C. Leu, K.P. Rajurkar, A.K.M. De Silva and Q. Liu, *CIRP Annals-Manfacturing Technology* 2001, vol. 50, p. 15.

29.   A.M. Suriano, S. Howard and S. Safarzadeh, *EPD Congress 2015* 2015, p. 6.

30.   A. Bard and L. Faulkner: *Electrochemical Methods Fundamentals and Applications*. (John Wiley and Sons, 2001).

31.   F. C. Anson: *Elecroanalytical Chemistry*. (American Chemical Society, Washington DC, 1976).

32.   M. Schlesinger and M. Paunovic: *Modern Electroplating*. fifth edition ed. (John Wiley & Sons, Inc).

33.   J. Town, F. MacLaren and H. Dewald, *Journal of Chemical Education* 1991, vol. 68, p. 2.

34.   D. R. Gaskell: *Introduction to the Thermodynamics of Materials*. Fifth Edition ed. (Taylor & Francis Group, LLC, 2008).

35.   H.S. Harned and B.B. Owen: *The Physical Chemistry of Electrolyte Solutions*. (Reinhold Book Corp., New York, 1958).

36.   R. Sarmaitis, V. Dikinis and V. Rezaite, *Plating & Surface Finishing* 1996, p. 4.

37.   *Properties and Selection: Nonferrous Alloys and Special-Purpose Materials*. (1991).

38.   R. Giovanardi and G. Orlando, *Surface & Coatings Technology* 2011, vol. 205.

39.   C. Housecroft and A. Sharpe: *Inorganic Chemistry*. Fourth Edition ed. (Pearson Education Limited 2012).

40.   *Alloy Digest - Data on World Wide Metals and Alloys*. (ASM International, 2011).

41.   M. Laubenstein and G. Heusser, *Applied Radiation and Isotopes* 2009, vol. 67.

42.   *Mini Table de radionucléides 2015*. (EDP Sciences, 2005).

43.   D. Chakrabrti and D. Laughlin, *Bulletin of Alloy Phase Diagrams* 1984, vol. D.

44.   Y. Jin, K. Adachi, T. Takeuchi and H.G. Suzuki, *Journal of Materials Science* 1998, vol. 33, p. 8.

45.   M. Bizjak, B. Karpe, G. Jakša and J. Kovač, *Applied Surface Science* 2013, vol. 277, p. 4.

46.   R. Islamgaliev, K. Nesterov and et al, *Journal of Applied Physics* 2014, vol. 115.

47.   V.S. Protsenko, V. O. Gordiienko and F. I. Danilov, *Electrochemistry Communications* 2012, vol. 17, p. 2.

48.   D. C. Harrie: *Quantitative Chemical Analysis*. Sixth Edition ed. (W.H. Freeman and Company, 2003).

49.   N.V. Mandich, *AESF 82nd Technical Conference* 1995.

50.   *International directory of radioisotopes*. (International Atomic Energy Agency, 1959).

51.   D. Snyder, *Metal Finishing* 2012.

52.   V.S. Protsenko and F.I.Danilov, *Clean Technology Environ Policy* 2014, vol. 16.

53.   *2000 PF Directory* 2000.

54.   K Mondal, NV Mandich and SB Lalvani, *Journal of applied electrochemistry* 2001.

55.   C. Liao, *Case Western Reserve University* 2012.

56.   M. Fontana: *Corrosion Engineering*. Third Edition ed. (McGraw Hill, 1986).

57.   I.M. Ritchie, *Adv. In Colloid and Interf. Sci* 1999, vol. 80.

58.	Z. Zhou, Z. Xiao, B.W. Wei, Y. Hu, L.W. Tang and C. Liu, *Procedia Engineering* 2012, vol. 29, p. 4.

59.	D. Butrymowicz, J. Manning and M. Read, *j Phys Chem* 1975, vol. 4.

60.	 *Copper and Copper Alloys*. (ASM International, 2001).

61.	A. Olofinjanaa and K. Tan, *Journal of Achievements in Materials and Manufacturing Engineering* 2009, vol. 35, p. 6.

62.	V. Proca and E. Proca, In *5th Int. Conference Structural Integrity of Welded Structures*, (Timisora, Romania, 2007).

63.	A. Vinogradov, Y. Suzuki, T. Ishida, K. Kitagawa and V. Kopylov, *Materials Transactions* 2014, vol. 45, p. 4.

64.	T. Todi, *Journal of Japan Inst. Metal* 1957, vol. 21, p. 5.

65.	N. Sathirachindaa, R. Petterssonb, S. Wessman and J. Pan, *Corrosion Science* 2010, vol. 52, p. 7.

66.	E. Lemmon and R. Jacobsen, *International Journal of Thermophysics* 2004, vol. 25.

67.	*Heat Treating*. (ASM International, 1991).

68.	*Casting*. (ASM Internaitonal, 1988).

69.	J. Robson: *Modelling the evolution of particle size distribution during nucleation, growth and coarsening*. (IoM Communications Ltd, 2004).

70.	*Encyclopedia of Materials: Science and Technology*. (Elsevier Ltd, 2001).

71.	*HKL Technology* 2005, vol. 8.

72.	G. Kurdjumov and G. Sachs, *Zeitschrift für Physik* 1930, vol. 64, p. 18.

73.	Z. Nishiyama, *Sci. Rep. Tohoku Imp. Univ. Tokyo* 1934, vol. 23, p. 27.

74. R. Nemenyi: *Controlled atmospheres for heat treatment*. (Pergamon Press, 1984).

75. I. S. Balegash: *Oxidation Protection For Metals And Alloys*. (Messer).

76. S. Roy and D. Landolt, *Journal of Applied Electrochemistry* 1997, vol. 27.

77. K. Hermann: *Crystallography and Surface Structure: An Introduction for Surface Scientists and Nanoscientists*. (Wiley-VCH Verlag GmbH & Co, 2011).

78. V. Voort: *Metallography Principles and Practice*. (McGraw Hill, Inc, 1984).

79. W. H. Hayt Jr.: *Engineering Electromagnetics*. Second ed. (McGraw-Hill, Inc, 1967).

80. D. C. Harris: *Quantiative Chemical Analysis*. Seventh Edition ed. (W.H. Freeman, 2007).

81. C. Yaws: *Yaws' Handbook of Properties of the Chemical Elements*. (Knovel, 2011).

Appendix A: Kinetics of Electrodeposition

RATE OF METAL DEPOSITION FROM AQUEOUS SOLUTIONS

Anne-Marie Suriano, Stanley Howard, Sadegh Safarzadeh

Abstract

The electrodeposition of metal ions from aqueous electrolyte solutions has been a well-known process for the last half century. With numerous industrial applications such as electroplating, electrowinning and electrorefining, the kinetics of electrochemical reactions involved in the process has been extensively researched. Arrhenius-type rate equations, the Butler-Volmer equation, and the empirical Tafel equation are among the most important models to explain the rate of electrochemical reactions. The study of the kinetics of metal deposition is critical to understanding the underlying mechanisms through which a certain morphology of metal deposit is formed on the cathode. The purpose of this paper is to elucidate the influence of experimental parameters such as pH and additives on the rate and the reaction mechanism determining the rate limiting step of the electrodeposition reactions.

Introduction

Electrodeposition as a method by which aquated metal is deposited onto a metal surface can be described by the charge transfer equation

$$M_{aq}^{+} + ze^{-} \rightarrow M_{s} \tag{1}$$

where M_{aq}^{+} is the metal ion in solution and M_{s} is the deposited solid metal. The electrodeposition of metal ions from an aqueous solution onto an electrode is a multi-step process consisting of

1) Mass transport of metal ions from aqueous electrolyte solution bulk to the metal-solution double layer, analogous to a boundary layer

2) Diffusion through the boundary layer

3) Integration onto the interface

4) Bulk metallic deposit growth

Commonly employed electrodeposition kinetics relations used to describe the driving forces behind metal deposition rate include the Butler-Volmer, generalized Frumkin-Butler-Volmer (gFBV), and Tafel equations. While the Tafel equation has been developed empirically, the former two equations rely upon ion concentration models of the reaction surface's diffusion layer. This layer is referred to as the Double Layer (DL) and shown to determine the rate for the many electrocrystallization cases which are controlled by a slow electron transfer step[1].

Electrodeposition Experimental Set-up

Fig. 1 shows a typical electrolytic cell with two anodes and a central cathode. The cathode is rotating such that convection currents in the electrolyte create steady state conditions. A rotation rate of approximately 1000 rpm is needed to achieve steady state[2,3,4,5]. Shown is a rotating cylindrical electrode (RCE). A rotating disk electrode (RDE) which uses a uniform flat electrode may also be used. So long as the same solution flow is induced, the method of inducing it does not factor into subsequent equations and calculations.
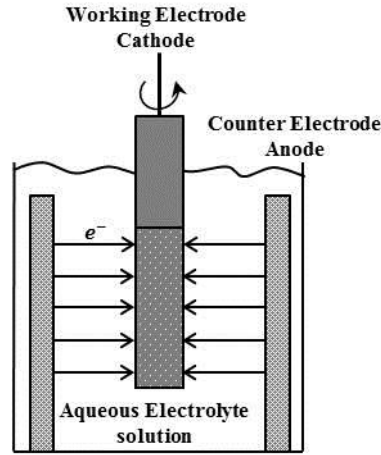
Figure 1: A Schematic of the rotating cylindrical electrolytic cell.

If the anode is assumed to have already dissolved sufficiently into the solution so as to reach a steady rate of deposition onto the working electrode, the cell is potentiostatically controlled and reversible potentials used for deposition may be calculated using the Nernst Equation,

$$E = E^0 + \left(\frac{RT}{nF}\right) \ln\{\frac{a_{ox}^p}{a_{red}^q}\} \tag{2}$$

where F is Faraday's constant, R is the gas constant, T is temperature, E is the electrode potential, E^o is the standard electrode potential, and a_{ox} and a_{red} are the activities of the oxidized and reduced species with stoichiometric coefficients p and q[1]. For a constant bulk concentration of ions in solution the plating potential is also constant, as shown in the Nernst Equation.

Determination of Rate Determining Step

There are many variables in an electrolytic bath and set up which would affect the kinetic rates and the subsequent slowest step. Convection, pH, concentration, current density, and additives have all been shown to effect rates[1-13].

Mass Transfer Rate Equations

The Nernst-Plank relation for ion transport in electrolyte,

$$-\nabla \cdot J_i = \nabla \cdot [D_i(c_i + c_i z_i f \nabla V)] \tag{3}$$

where J_i is the flux, D_i diffusivity, z_i ion valence, c_i ion concentration and V voltage potential, has been used to describe mass transport for a dilute electrolyte[6]. It however does not allow for advection or chemical reactions in solution. These effects may be addressed by the Poisson equation, which relates electrical potential with charge density[6],

$$\nabla \cdot (\varepsilon \nabla V) = -F \sum_i z_i c_i. \tag{4}$$

The large boundary layer potential as described in the next section must also be considered when considering the effect of the electrical potential in Eq. 4. For a steady state system the Poisson-Nernst-Plank equation describes mass transfer in the bulk solution by combining Eqs. (3) and (4) with boundary layer potential effects giving the ion concentration in solution at a position and time,

$$c(x,\tau) = 1 + 2i_{app}\{0.5 - x - \sum_{n=1}^{n=\infty} f_n \cos(\frac{2Nx}{L})\} \tag{5}$$

where f_n and τ are functions of time, I_{app} is the applied current, and L and x are spatial positions[6].

Since ion flux and thus solution convection currents determine mass transfer rate, the speed of the rotating electrode is important. The slowest rate step, whether diffusion or chemical reaction, may be determined by monitoring the effect of cathode rotation speed on the rate of metal deposition[7]. The mass transfer coefficient increases with flow

rate[5] while the current density decreases indicating a shift from electron-transfer control to diffusion control[3].

<u>Charge Transfer Rate Equations</u>

The Butler-Volmer description of the classic Double Layer (DL) model is shown in Fig. 2. Here the metal ions in solution are considered to have finite size and the reaction surface is coated in a layer of solvent molecules. Since the ions are restricted in their surface approach by their size both a charge free and a charge covered surface layer are created. These act as a capacitor where the ion layer is one plate and referred to as the outer Helmholtz plane and the surface of the metal-aqueous solution is the other plate called the reaction plane. Ions in solution undergo at least one electron transfer reaction at the DL, which is described by a Faradaic charge transfer relation. In order to balance the charge and maintain the operating potential, ions transfer charge and replace the solvent atoms shown in Fig. 2. This charge-transfer adsorption is called specific adsorption[1] and generally occurs before bulk metallic growth. Since the behavior of an electrochemical reaction is characterized by a polarization resistance at the interface, the capacitance of the DL determines the rate[8]. The potential drop between the working electrode and the bulk electrolyte solution, which is analogues to the overpotential, drives the reaction[6] and leads to the general Butler-Volmer equation,

$$i = -nFAk_{Red}C_{Red}exp(\alpha nfE) \tag{6}$$

for

$$f = F/RT \tag{7}$$

where A is the electrode surface area, k_{Red} the rate constant and α the transfer coefficient[1]. It should be noted that the Butler-Volmer equation shown is in terms of

current, through measurement of which rate is determined[5]. Commonly deposited are higher oxidized metal ions, such as Cu^{2+}, which must go through multiple consecutive electron reactions at the DL. In such cases the slower reaction is generally found to be the first electron reaction[4,8].
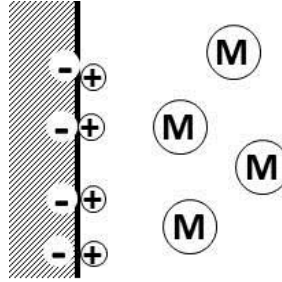

Figure 2: Classical Butler-Volmer double layer model for + solvent surface coverage and M ions in solution.

The generalized Frumkin-Butler-Volmer (gFBV) equation is extension of the Butler-Volmer model, which goes farther to take into effect upon the rate the DL composition[6]. In this model, which is shown in Fig. 3, a diffuse layer with non-zero charge is included between the reaction plane and the zero-charge zone causing a change in potential drop across the DL, which is assumed to be linear in the Butler-Volmer model. This contributes to the total cell potential although the ion concentration of the bulk remains the same as considered in the simpler model. Therefore this impacts the charge transfer rate and the electrical potential. The driving force is the ion concentration at the reaction plane and the electric field strength describing the potential drop across the charge-free layer,

$$J_F = K_R c_{O,bulk} \exp\{-(\alpha *)nf(V_m - V_{bulk})\} - K_O c_{R,bulk} \exp\{(1 - \alpha *)nf(V_m - V_{bulk})\} \ (8)$$

where K_i are rate constants, V_i are voltages, c_i are concentrations, and the effective transfer coefficient, $\alpha *$, is the transfer coefficient adjusted for dependence upon the

diffusion layer to zero-charge layer capacitance ratio[6]. From this it can be seen that for zero-charge layer thickness << diffusion layer thickness, the latter will dominate the charge transfer rate necessitating the use of the gFBV equation. For zero-charge layer thickness >> diffusion layer thickness, the former dominates and $\alpha *$ will approach the value of the classical transfer coefficient such that the Butler-Volmer equation may be used[6].
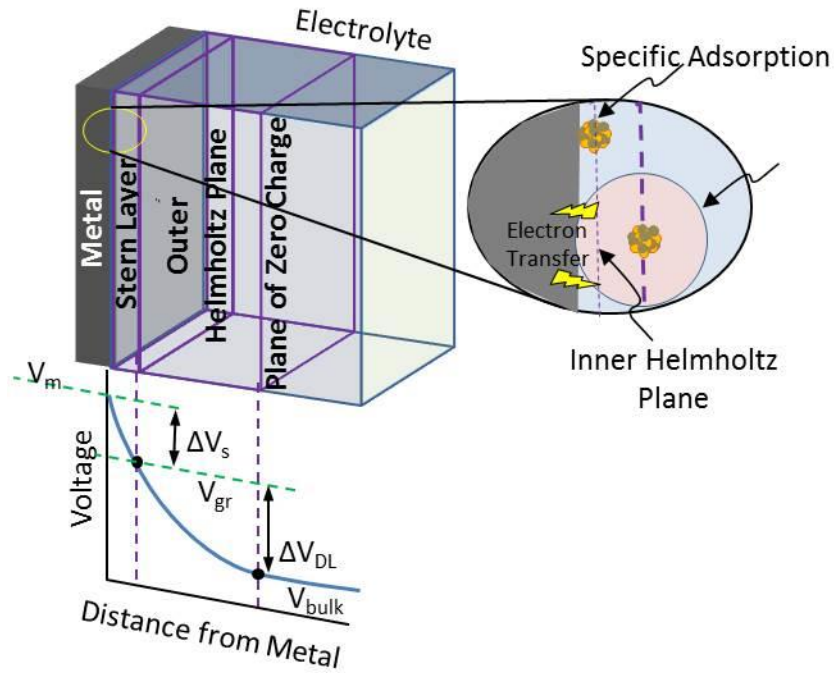

Figure 3: Frumkin-Butler-Volmer double layer model

Charge Transfer Adsorption

Before metal ions grow in the bulk metal solid phase, they are generally adsorbed on the electrode surface. This is described by the Frumkin isotherm for charge-transfer adsorption,

$$\left[\frac{\theta}{1-\theta}\right] expf\theta = kCexp(\frac{\gamma nFE}{RT}) \tag{9}$$

where $(1-\theta)$ is the fraction of active adsorption sites, n is number of electrons, k & f are constants, C is adsorbate concentration, and γ is the electrosorption valency which accounts for DL charge changes during adsorption[1]. The rate and manner of which the layers of metal ions are adsorbed and consequently deposited may vary for the first monolayer deposited upon the working electrode surface and the subsequent multilayers deposited onto the bulk metal, since the composition and crystal structure of the two substrates are generally different[1].

Adsorption is very important in the case of organic surfactants being added to the electrolyte for nucleation enhancement. Studies found that the addition of organics which do not affect the metal ion's deposition reaction pathway inhibit rate of the deposition due to adsorption[4]. This is shown by the decreasing limiting current density with increase in organic concentration. Organic molecules in the electrolyte solution follow the Langmuir isotherm,

$$\frac{\theta}{1-\theta} = KC \tag{10}$$

for equilibrium constant K[7]. Therefore, the metal ions and the organic molecules will vie for active adsorption sites and inhibit the adsorption and deposition rate[4,7].

Nucleation

Alternately, the interface conditions of the electrocrystallization process in an electrolytic cell may result from nucleation rather than adsorption. The rate of nucleation in such processes is generally found empirically by evaluating the current-time transients over potential steps[1].

Experimental Methods

The slowest mechanism is determined experimentally. Voltammetry analysis can be used to show if a deposition process with given parameters is diffusion controlled. A voltammetry sweep is conducted over a determined range, giving potential regions at different current densities. A kinetic peak indicates the mass transfer process and lack of any diffusion peak indicates charge-transfer rate control[9]. Chronoamperometric analysis is also used. Current transients I-$t^{1/2}$ are plotted and linear behavior indicate mass-transfer rate control. These experiments may be conducted with respect to varying parameters such that the effect of the parameter upon rate determining mechanism may be analyzed. As is modeled by the Butler-Volmer equation where the current density drives the equation, much investigation into the RDS is done through observing current density behavior relative to a given electrolytic system. The Tafel Equation,

$$E = a - blog|i| \qquad\qquad (11)$$

where a and b are the Tafel parameters determined experimentally[1], relates the current to the potential and are used to determine the effect of current efficiency[10,11].

Conclusions

The electrolytic cell controlling electrodeposition of metal ions from aqueous solutions to bulk metal solids is complex and has many variables that may affect the rate of deposition. Considerable experimental and theoretical work has been done to determine the effect of varying parameters on the rate determining mechanism. Current density and overpotential examinations give data sufficient to determine the slowest step for most electrodeposition systems.

References

1. I.M. Ritchie, "The metal-solution interface," *Adv. In Colloid and Interf. Sci.*, Amsterdam: Elsevier, 80 (1999), 183-231.

2. E.J. Podlaha, and D. Landolt, "An Experimental Investigation of Ni-Mo Alloys*," J. Electrochem. Soc.*, 143 (1996), 885-892.

3. E.J. Podlaha, and D. Landolt, "A Mathematical Model Describing the Electrodeposition of Ni-Mo Alloys," *J. Electrochem. Soc.*, 143 (1996), 893-899.

4. S. Varvara, "Kinetics of copper electrodeposition in the presence of triethyl-benzyl ammonium chloride*," J. of Appl. Electrochemistry*, Netherlands: Kluwer Academic Publishers, 33 (2003), 685-692.

5. T. Subbaiah, S.C. Das, and R.P.Das, "Mass transfer rates in an electrochemical cell," *Hydrometallurgy*, Amsterdam: Elsevier, 33 (1993), 153-163.

6. M.V. Soestbergen, "Frumkin-Butler-Volmer Theory and Mass Transfer in Electrochemical Cells*," Russian J. of Electrochem.*, Pleiades Publishing Inc., 48 (2012), 570-579.

7. A.M.M. Ahmed, "Effect of Organic Solvents on the Electrodeposition of Copper from Acidified CuSO4*," J. of Dispersion Sci. and Tech.*, Taylor & Francis, 33 (2012), 898-912.

8. V.S. Protsenko, "Applying a Theory of Generalized Variables to Electrochemical Kinetics," *Protection of Metals*, Pleiades Publishing Inc., 43 (2007), 398-406.

9. M. Torabi, "A Kinetic study on the electrodeposition of nickel nanostructure and its electrocatalytic activity for hydrogen evolution reaction," *J. Appl. Electrochem.*, Springer, 40 (2010), 1941-1947.

10. O.E. Kongstein, F.M. Haarberg, and J. Thonstad, "Current efficiency and kindetics of cobalt electrodeposition in acid chloride solutions," *J. Appl. Electrochem.*, Springer, 37 (2007), 669-674.

11. O.E. KongsteinF.M. Haarberg, and J. Thonstad, "Pt II. The influence of chloride and sulphate concentrations," *J. Appl. Electrochem.*, Springer, 37 (2007), 675-680.

12. I. Giannopoulou, D. Panias, I. Paspaliaris, "Electrochemical modeling and study of copper deposition from concentrated ammoniacal sulfate solutions," *Hydrometallurgy*, Amsterdam: Elsevier, 99 (2009), 58-66.

Appendix B: Metallographic Sample Preparation Polishing Procedure

1. 320 grit silicon carbide grinding paper with water

2. Buehler Trident polishing cloth with Metadi 9um diamond suspension

3. Buehler Trident polishing cloth with Metadi 3um diamond suspension

4. Bueler Microcloth Metadi with 1um diamond suspension

5. Bueler Microcloth Masterprep 0.05um Alumina
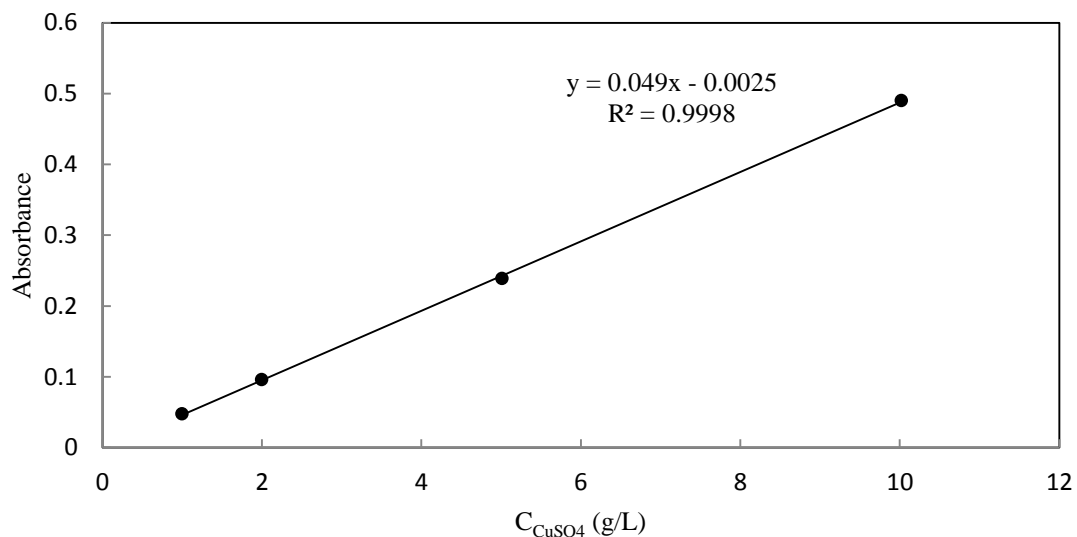
Appendix C: Spectrophotometer Calibration Curves

$$y = 0.049x - 0.0025$$
$$R^2 = 0.9998$$

Figure C.1: $CuSO_4$ spectrophotometer calibration curve

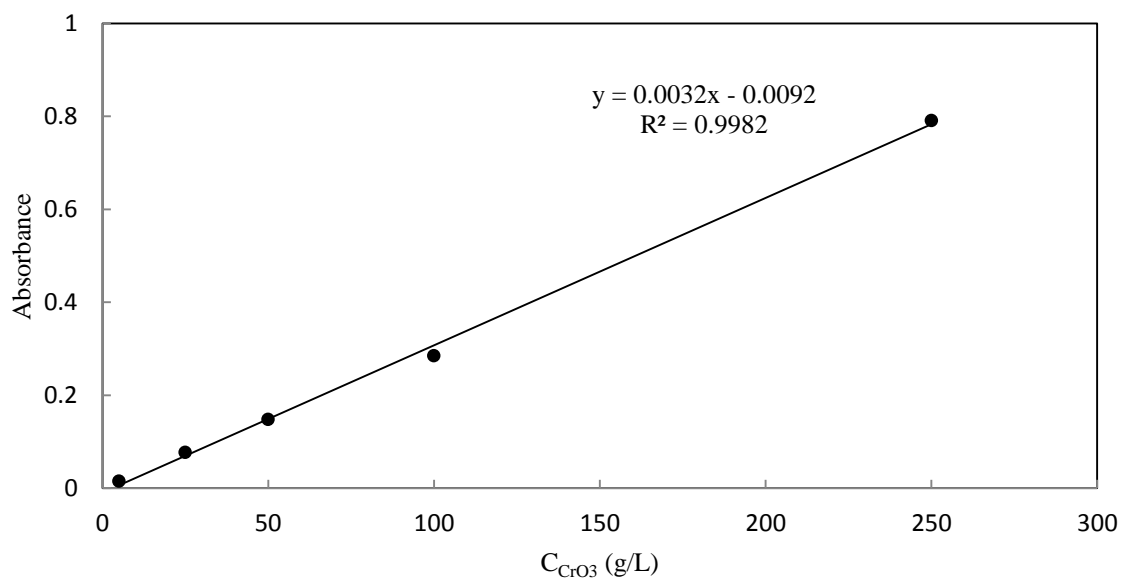$$y = 0.0032x - 0.0092$$
$$R^2 = 0.9982$$

Figure C.2: H_2CrO_4 spectrophotometer calibration curve

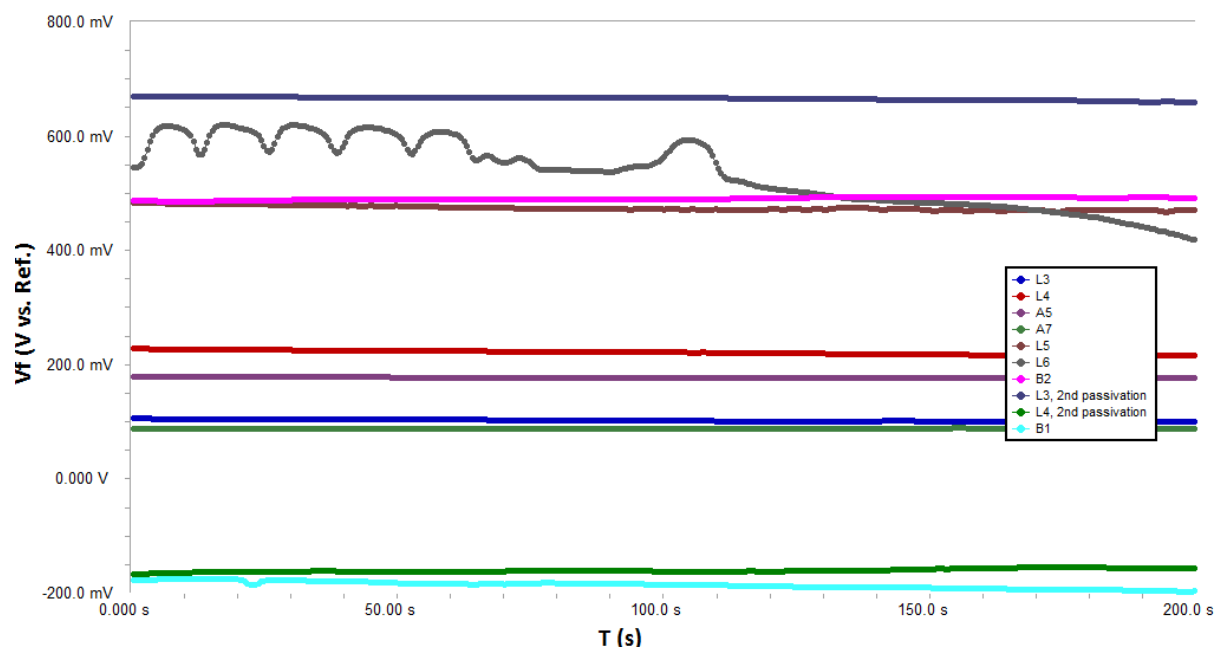**Appendix D: Cr Cell**

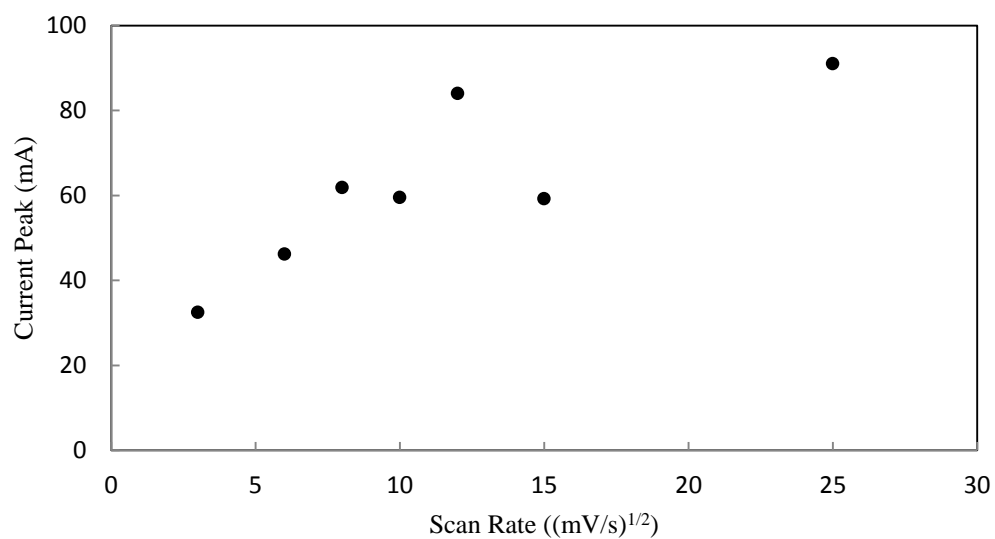Figure D.1: Corrosion potential curves for each of the passivated Pb anodes described in Table 3.6

Figure D.2: Peak positions for higher scan rates taken in quasi-reversible Cr system

Vita

Anne-Marie Suriano was born in Lafayette, Indiana. She completed high school at Avondale High School in Auburn Hills, Michigan. She earned Bachelor's degrees in Mathematics and Physics from the University of Wyoming in Laramie, Wyoming in May, 2007. After completing her undergraduate degrees she occupied a position as a Data Analysis Engineer for the Defense Engineering Corp. in Dayton, Ohio.

Ms. Suriano worked during the duration of her Ph.D. studies for the Majorana Collaboration in the Sanford Underground Research Facility in Lead, South Dakota. She is a member of the Electrochemical Society and Materials Advantage which includes The Minerals, Metals & Materials Society, Association for Iron & Steel Technology, American Society for Metals, and The American Ceramic Society.

Ms. Suriano is the recipient of the 2014 DOE Office of Science Graduate Student Research Fellowship. She conducted her fellowship research at Pacific Northwest National Laboratory (PNNL) in Richland, Washington in 2016. After the fellowship completion, she continued her research as a Ph.D. Intern at PNNL. She was awarded the "Outstanding Graduate Student in Materials Engineering and Science" from The South Dakota School of Mines and Technology in 2016.